Study of ionization dynamics of high-Z target irradiated by high-intensity laser and acceleration of multiply charged ions

Daiki Kawahito

Acknowledgement

First of all, I would like to express the deepest gratitude to my supervisor, Professor Yasuaki Kishimoto for his continuous encouragement and prospective guidance for my research for five years in Kyoto University. The present thesis would not have been achieved without his help. I am in debt to his generosity in having a wide viewpoint on nature, which has been a great help for me to keep faith in my research.

I would like to acknowledge to Assistant Professor Kenji Imadera for his continuous support over five years. He has provided me helpful advices and encouragements. I would like to thank all the members of our laboratory, especially, Dr. Natsumi Iwata, Dr. Feng Wu, Mr. Wang wei, Mr. Ryutaro Matsui, for their help and fruitful discussions on the theoretical study of laser-matter interaction. I would like to appreciate secretary Ms. Tomoko Takahashi. I couldn't have studied without her supports.

I would like to acknowledge to thesis committee Prof. Yuji Nakamura and Prof. Hitoshi Tanaka for their helpful remarks.

I would like to acknowledge to Prof. Yasuaki Sentoku, Assistant Professor. Takayoshi Sano in Osaka University, and Prof. Kunioki Mima in Graduate school for creation of New Photonics Industries for their encouragements and insightful comments to proceed my research. I would like to appreciate Prof. Shuji Sakabe, appreciate Professor Masaki Hashida, and Dr. Kazuaki Mori in Kyoto University for their valuable comments and discussions to proceed research of THz emission. I would like to appreciate Dr. Yuji Fukuda in National Institutes for Quantum and Radiological Science and Technology (QST) for his valuable comments on the study of laser-cluster interaction from the viewpoint of a experimentalist. I would like to appreciate Dr. Mamiko Nishiuchi and Dr. Hironao Sakaki in QST for their valuable comments on the study of heavy ion acceleration from the viewpoint of a experimentalist. I would like to appreciate Dr. Kengo Moribayashi in QST for his great help for calculation of the ionization potential. I would like to acknowledge to Dr. Tomohiro Masaki for his great help and support in developing the EPIC3D code.

I would like to acknowledge to Prof. Makoto Asakawa in Kansai University for his grateful guidance which is the basis for my study.

I am grateful to my family, Minoru Kawahito, Akemi Kawahito and Riku Kawahito for all their support and encouragement in my life.

Abstract

With development of laser technology in recent years, new research field named high energy density science was also developed. This is a new science exploring ultra-high temperature and ultra high-density plasma in the laboratory system by taking advantage of the high-intensity laser pulse which could input high energy density. This extreme plasma state includes various elementary processes such as ionization process, nuclear reaction, electron-positron pair creation accompanied with energy sources of high energy ions, electrons and emission of high luminance X-rays and γ -rays. Therefore, this study could lead to a wide range of scientific fields such as atomic physics, astrophysics, etc., and advanced technology such as laser fusion and particle acceleration. Internationally, large-scale laser facility covering high laser intensity of $I = 1.0 \times 10^{22-23}$ W/cm^2 with the aim of promoting this high energy density science is constructed. Furthermore, international magazine 「Journal of High Energy Density Physics」 starts to be published from 2005. Therefore, such new field of physics is being opened up.

Recently, the experimental result was reported that iron ions with the fully ionized state are observed in 1/5 of the light velocity through the high-intensity laser interaction. This is the result of generating relativistic heavy element plasmas based on iron or heavier atoms, and it indicates the possibility of their applications beyond the framework of conventional plasma generated by the laser field. Such laser particle acceleration can instantaneously extract unstable nuclei that can exist only for a short period from psec to nsec and is expected to be applied to the discovery of new nuclei that could not be observed so far.

On the other hand, the radiations, which the characteristic X-ray through the ionization process and the bremsstrahlung of hard X-ray and γ -ray through the collision with heavy ions, can be a new high-brightness emission source for industrial and medical applications. In addition to that, the radiation process in the laser produced plasma is also an important process responsible for energy transport in the heavy element medium.

However, since heavy elements have a lot of electrons bound by various energy levels, the ionization state sensitively changes in response to small electric fields and temperature changes. Especially in solid media such as iron and gold, the internal ionization structure is an important parameter as the initial value of plasma dynamics since the laser is reflected on the solid surface. In previous studies, a fully ionized state has been assumed by selecting relatively light elements, or an arbitrary state has been predicted by using the Thomas-Fermi model in thermal equilibrium. The heavy element plasma generated by the ultra short-pulse and high-intensity laser whose spatiotemporal structure rapidly changes is a non-equilibrium and non-stationary state, and arbitrary assumption does not hold.

Based on the above background and problems, not only a calculation model describing plasma dynamics but also an ionization process is indispensable. Therefore, we extended the particle in cell code (PIC) to the heavy element ionization model based on the field ionization process and the collisional ionization process accompanying the relaxation process. Furthermore, we introduced (1) bremsstrahlung process coupled with the collisional process, (2) radiative excitation through the inner-ionization, and (3) radiation damping effect in the high-intensity field. As a result, the laser-solid interaction coupled with the ionization dynamics and the radiation process according to the time transition of the charge state can be evaluated. Using the developed simulation model and theoretical system, the following results were obtained regarding the generation and acceleration process of heavy ion plasma by high-intensity laser irradiation.

1. Multistage ionization process inside the solid film: Two types of ionization dynamics exhibiting different spatio-temporal structures are found to regulate the process predominantly, which emerge depending on the laser amplitude. One is the fast convective propagation for the charge state up to C^{4+}, which keeps a steep ionization front. The velocity of the front is in the same order as the speed of light. This results from the formation of the localized longitudinal electrostatic field and associated field ionization, which turns to propagate inside the film. The trigger of such a convective propagation takes place when the laser field becomes high enough that the electron bunch accelerated by the laser ponderomotive force reaches to a relativistic energy and tends to penetrate inside the film across the surface. The other is the fast non-diffusive propagation of ionization showing a long plasma density scale length for C^{5+} and C^{6+}. This process results predominantly from the electron impact ionization by high energy electron bunches successively produced by the laser. These electron bunches also excite wake fields which propagate insides the film and contribute to ionize the film to higher charge state, i.e. C^{5+} and C^{6+}, especially near the front surface.

2. Ionization dynamics in high-Z solid target: It is found that ionization wave propagates with the electron transport for laser transverse direction. Here, we investigated the ionization dynamics of an aluminum film in 2-dimensional. Around laser spot area, the field ionization to Al^{11+} which is the final state of L-shell proceeds with the electric field as discussed in the above. After the ionization to the propagation direction, the ionization wave of Al^{11+} also propagates to the laser transverse direction beyond the laser spot area. However, the amplitude of the electric field on the ionization front gradual decreases due to the electron diffusion with the spread to the transverse direction, and the impact ionization rate becomes larger than that of the field. Therefore, the velocity of the ionization wave with Al^{11+} is decelerated with the propagation to the transverse direction. Additional to these rapid ionization processes, Al^{12+} and Al^{13+} are ionized by the sheath field excited on both surfaces. They

are extracted through the acceleration mechanisms which are discussed as follows.

3. Acceleration of multiply ionized ions in a high-Z solid film: Ionization of a thin film irradiated by a high-intensity short pulse laser in the range of $I = 10^{20-22}\mathrm{W/cm}^2$ and associated acceleration of multiply charged high-Z ions are shown. Two kinds of acceleration mechanisms that cause different types of longitudinal electrostatic fields are found to attribute to the generation of highly charged ions with the kinetic energy in the order of 10 MeV/u. One is the radiation pressure acceleration (RPA) in which both the laser field dominantly ionizes atoms around the front surface of the film to higher charge state and accelerates them toward the inside of the film. The other is the target normal sheath acceleration (TNSA) in which the electrostatic sheath field penetrated inside the film from the rear surface also ionizes atoms to higher charge states and accelerates them into the vacuum region. For TNSA mechanism, we derived the theoretical scaling of the peak ion energy for each charge state, where the amplitude of the electric field corresponding to the ionization potential is assumed. It correctly describes the ion energy of each charge state in the range that the field ionization dominantly takes place. It is found that the multiply charged ion of the rear surface is accelerated to the maximum ion energy in considering only the gold film even if the highest charge state of ion is ionized at the front surface interacted by the laser field.

Contents

1 Introduction

1. 1 Development of the laser field

Towns and Schawlow theoretically proposed the principle of laser technology in 1958[1], and two years later, it was realized by Maiman using excitation of ruby laser.[2]. After the first excitation of the laser field, laser technology has been developed dramatically, and lasers with various frequency using various excitation media including gas, liquid, and solid have been developed. Recently, free electron lasers with variable frequency have been developed, and the shortest wavelength of 1.2 Å was realized from the resonant interaction between the high-speed electron beam and the electromagnetic field as represented by SACLA in Japan. The laser intensity can also reach to an unprecedented high-intensity field by collecting light to a small area of μm for a short time of fsec. Especially, high-intensity laser technology has been vigorously developed based on Ti: sapphire having a wide wavelength range. Q-switch technology that can output a very high power instantaneously and mode synchronization technique that oscillates at the same time by aligning the phases at multiple wavelengths has been taken for a laser amplification. In addition to these technologies, CPA technology[3] was a breakthrough method to increase the laser intensity. With the development of these technologies, the laser energy currently being developed reaches PW class. Furthermore, by focusing the laser field to the region close to the diffraction limit, the instantaneous laser intensity exceeded the field amplitude inside the atom, and it was possible to accelerate the electron to the relativistic region in only one period. By developing such a high-intensity laser, it becomes possible to generate the relativistic plasma state artificially.

The equation of motion for a charged particle qe is written as

$$\frac{d\boldsymbol{p}}{dt} = qe(\boldsymbol{E} + \frac{\boldsymbol{v}}{c} \times \boldsymbol{B}).$$

Here, $\boldsymbol{p}$ and $\boldsymbol{v}$ are a momentum and velocity of the particle, c is light velocity, and $\boldsymbol{E}$ and $\boldsymbol{B}$ are electric and magnetic fields of the laser, respectively. In non-relativistic motion, $\boldsymbol{v}/c \times \boldsymbol{B}$ term is negligible so that it is approximated to

$$\frac{d\boldsymbol{p}}{dt} \simeq qe\boldsymbol{E}.$$

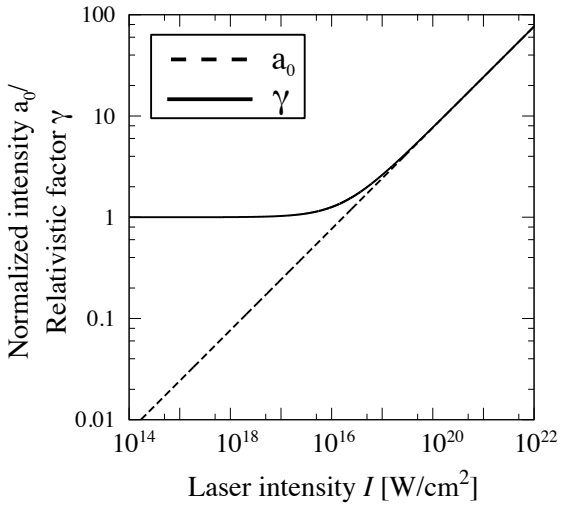

Fig 1.1: Dependece of normalized intensity a_0 and relativistic factor$\gamma = v/c$ on laser intensity I[W/cm^2]. The relativistic factor γ illustrated as solid line is related to the normalized laser intenity a_0 illustrated as dashed line as $\gamma = \sqrt{1 + a_0^2}/2$.

In simplified case, the laser field is assumed as plane wave, i.e., $\boldsymbol{E} = \boldsymbol{E_0} \exp \omega_L t$, where ω_L is laser frequency. From this equation, the momentum of quiver motion is determined by $p_0 = |q|E_0/\omega_L$. Here, we define the normalized unit for the electron motion as

$$a_0 \equiv \frac{p_0}{m_e c} = \frac{eA_0}{m_e c^2} = \frac{eE}{m_e c \omega_L}.$$

where, e and m_e represent the electron charge, electron mass, and A_0 is vector potential of the laser field. From this normalized unit, the speed of the electrons oscillating with the electric field v_e could be evaluated by $v_e \simeq a_0 c/(1 + a_0^2)^{\frac{1}{2}}$. Therefore, the electron motion is non-relativistic region ($v \gg c$) in $a_0 \gg 1$, and the electron motion reaches to relativistic region ($v \sim c$) in $a_0 \ll 1$.

The relation between the laser intensity I[W/cm^2] and a_0 is the following formula.

$$I = \frac{1.365 \times 10^{18} a_0^2}{\lambda} [\mathrm{W/cm^2}]$$

Figure. 1.1 shows the ratio between the relativistic factor v/c and the laser intensity I for the wavelength $\lambda (= 0.8\ [\mu m])$ assumed Ti: sapphire crystal. In the physical process for this intensity range, when the laser intensity exceeds 1.0×10^{14} [W/cm^2], a hydrogen atom is ionized by the electric field. The generated electrons are accelerated up to the relativistic region by receiving the field of $10^{16} \sim 10^{18}$ [W/cm^2]. By irradiation of such high-intensity laser to the solid target, high energy density plasma accompanying with high energy electrons is generated in the inside of the solid medium.

1. 2 Background of laser interaction with solid medium and laser applications

With development of laser technology in recent years, new research field named as high energy density science was also developed. This is a new science exploring ultra-high temperature and ultra high-density plasma in the laboratory system by taking advantage of the high-intensity laser pulse which could input energy in a small area ($\simeq$ μm) and in short time ($\simeq$ ps). Such extreme plasma state includes various elementary processes such as ionization process, nuclear reaction, electron-positron pair creation accompanied with energy sources of high energy ions, electrons and emission of high luminance X-rays and γ -rays. Therefore, this study could lead to a wide range of scientific fields such as atomic physics, astrophysics, etc., and advanced technology development such as laser fusion and particle acceleration. Internationally, large-scale laser facility covering the laser intensity of $I = 1.0 \times 10^{22-23}$ W/cm^2 with the aim of promoting these high energy density science was constructed in recent years. Furthermore, international magazine 「Journal of High Energy Density Physics」 starts to be published from 2005 for this science. Such new field of physics is being opened up.

Various application studies are being developed utilizing the interaction between such a high intensity laser and a solid medium. Among them, laser ion accelerator and laser fusion have been studied as one of the most interesting subjects in the laser-matter interaction.

The feature of laser ion acceleration is to generate high energy ions from small devices. High energy electrons are accelerated from the solid surface irradiated by a high-intensity laser pulse, and then these are injected into a solid thin film. These electrons are emitted into the vacuum region and then the steep electric sheath field with 10^{12} V/m is excited near the surfaces. It possible to accelerate ions up to MeV range through such mechanism. From the advantage that high energy ions can be obtained from the small size in the order of sub-ten μm, the laser-driven accelerator can be a main scheme instead of the conventional accelerator with over 100 m scale. It also has the attractive properties that the emittance, indicating the quality of the particle beam, can be suppressed to lower value than that of conventional one by two orders since the electric field mostly accelerates to the perpendicular direction of the film surface. From these properties, it is expected to be applied to fast ignition driven by the ion beam and compact ion beam cancer therapy, and so on. However, it has not been achieved to obtain particle beams exceeding 100 MeV/u required for cancer therapy. Also, there are some problems to be solved such as the wide range of ion energy and accelerated ion amount, and so on.

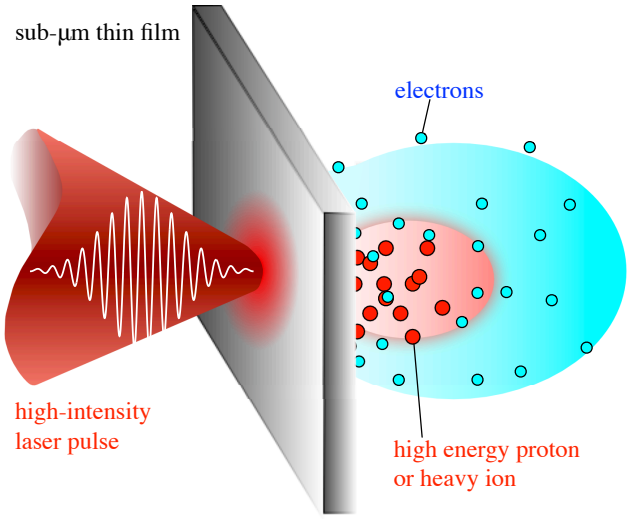

Fig 1.2: Laser driven ion acceleration. High energy electrons are accelerated from the solid surface by irradiating a high-intensity laser pulse, and strong sheath electric field is excited on the rear surface. Then, ions are accelerated to the vacuum region.

In laser fusion, a fuel ball filled with deuterium and tritium is compressed into a high density and high-temperature state by using a high-intensity laser. It is expected as an influential nuclear fusion reactor as same to confinement magnetic fusion technique. There are two methods for laser fusion: direct irradiation method and indirect irradiation method. In the direct irradiation method, the target surface is rapidly ionized and heated by an irradiation of laser field. Then, the target surface becomes a high-pressure state, and the plasma is rapidly ejected to the outside region (laser ablation process). By its counteraction of the expanded and accelerated plasma, the target is compressed into the inside into the core target. When the laser fields uniformly are irradiated to the target surface of a spherical target, laser implosion takes place in which the plasma is compressed to the center of the target with a high-density state. The performance of laser fusion is greatly influenced by the implosion condition. Therefore, a technique of re-heating for the compressed core has been carried out for such ignition by using a gold corn target and a high-intensity laser. Osaka University in Japan, Naval Research Laboratory (NRL) in the USA, etc. are conducting research using such method. On the other hand, in the indirect irradiation method, X-ray emitted from the gold hohlraum irradiated by multiple lasers is carried out for the uniform implosion as seen in Fig. 1.3(a). The indirect irradiation method realizes uniform implosion of the target surface, but on the other hand, it is inefficient for heating due to the energy conversion to X-rays. Since the target structure becomes complicated in this scheme, it is regarded that the system is not suitable for a practical nuclear fusion reactor in recent research. This method is adopted in the National Ignition Facility (NIF) and Laser MegaJoule (LMJ) etc. In 2014, they succeeded in releasing energy exceeded the input amount at the first time.

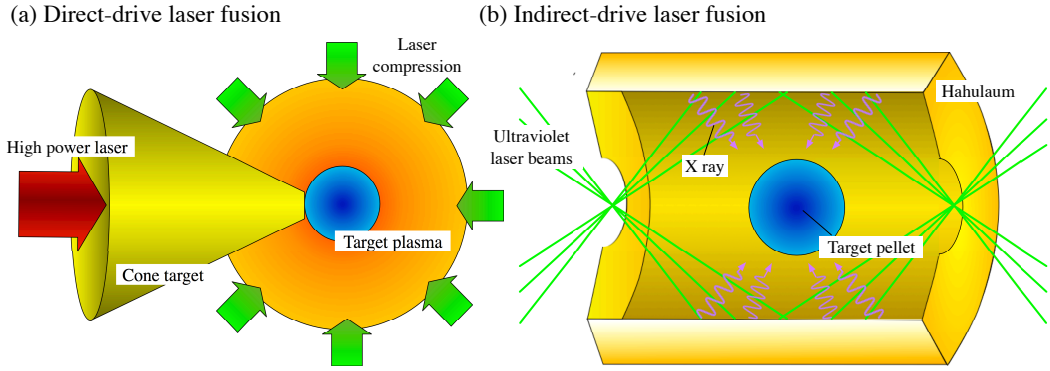

Fig1.3: Fusion mechanism of laser direct-implosion (a) and laser indirect-implosion (b)

In such applications, the high-Z material such as aluminum material utilized in the ion acceleration and gold material of cone target in fast ignition and hohlraum for indirect implosion has been used. In a study utilizing the interaction between such a high-intensity laser and a heavy element medium, ionization process plays an important role in the plasma dynamics. In such plasma, multiple particles such as neutral atoms, molecules, heavy ions, and electrons, etc., coexist through complex atomic, molecular processes, and collisional relaxation processes. Also that, the hot-dense plasma generated through such interaction shows a large number of non-stationary and non-thermodynamic features. Therefore, it is necessary to understand the ionization process for development and control of these applications.

1. 3 Basic properties in laser-matter interaction

Here, we introduce the basic properties in laser-matter interaction. The first is the single-particle interaction with the laser field and the electron motion in the non-relativistic and relativistic region. The second is the laser ponderomotive force as the collective effect in the plasma. It is derived by the dimensional separation to slow and fast scale to solve the fluid motion of electrons and ions in the interaction with the laser pulse. The third is the absorption process near the solid surface, which mechanism mainly depends on the laser incidence angle and the scale length of pre-plasma.

Considering in the laser interaction with a single electron, the electron motion is solved by the Lorenz equation (1.1-1). In non-relativistic regime, i.e., $a_0 << 1$, the electron oscillates along the laser oscillation in the polarized direction. Here, the magnetic field of the laser field becomes significant in $a_0 > 1$, and the election moves to the laser propagation

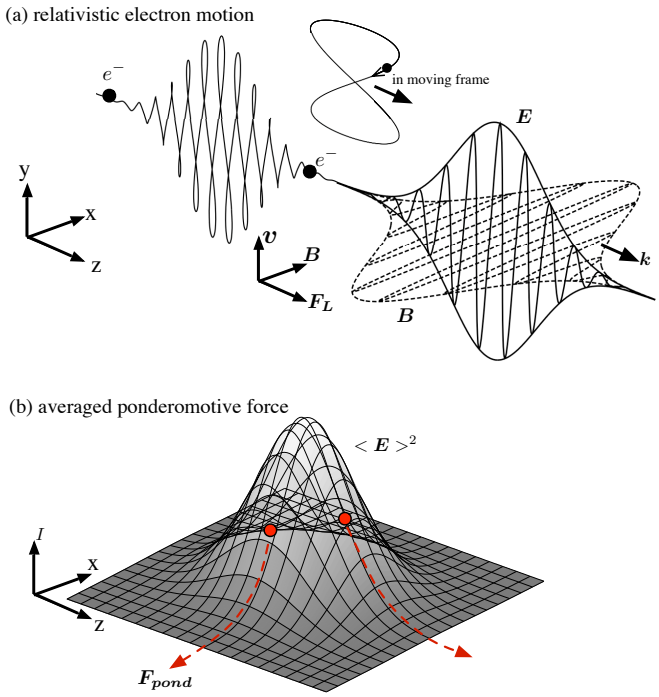

Fig 1.4: (a) The relativistic electron motion inside the linearly polarized laser field. The Lorenz force pushes the electrons forward which results from an eight-figure motion. (b) The intensity of the laser pulse for propagation direction z and radial directions. the averaged ponderomotive force pushes the electrons to the radial directions

direction due to $\boldsymbol{v} \times \boldsymbol{B}$ term. Such electron motion is called as eight-figure motion as seen in Fig. 1.4(a). If the electrons initially from to energetic electron beam, the incident laser field is scattered by them, and the secondary radiation emitted from the electron motion. This mechanism provides a way to generate brightness X-rays and γ-rays which can be used to resolve various physical, biological reactions with ultrashort spatiotemporal scales.

We derive the laser ponderomotive force in under-dense plasma. When laser field is irradiated to dense plasma, the electrons and ions are accelerated by the light pressure of the laser field as seen in Fig. 1.4(b), which is derived from the fluid equation of electron motion and ion motion as follows[4].

$$\frac{\partial \boldsymbol{v_i}}{\partial t} + (\boldsymbol{v_i} \cdot \nabla)\boldsymbol{v_i} = \frac{q}{M}\boldsymbol{E} + \frac{Ze}{M}(\boldsymbol{v_i} \times \boldsymbol{B}) - \frac{T_i}{M}\nabla \ln(\mathrm{n_i}) \tag{1.3-1}$$

$$\frac{\partial n_i}{\partial t} + \nabla(n_i \cdot \boldsymbol{v_i}) = 0 \tag{1.3-2}$$

$$\frac{\partial \boldsymbol{v_e}}{\partial t} + (\boldsymbol{v_e} \cdot \nabla)\boldsymbol{v_e} = \frac{q}{M}\boldsymbol{E} + \frac{q}{M}(\boldsymbol{v_e} \times \boldsymbol{B}) - \frac{T_e}{M}\nabla \ln(\mathrm{n_e}) \tag{1.3-3}$$

$$\frac{\partial n_e}{\partial t} + \nabla(n_e \cdot \boldsymbol{v_e}) = 0 \tag{1.3-4}$$

For these equation, we separate the parameters to slow scale and fast scale as

$$\begin{aligned}
\boldsymbol{E} &=< \boldsymbol{E} > +\tilde{\boldsymbol{E}} \\
\boldsymbol{B} &=< \boldsymbol{B} > +\tilde{\boldsymbol{B}} \\
\boldsymbol{v_e} &=< \boldsymbol{v_e} > +\tilde{\boldsymbol{v_e}} \\
n_e &=< n_e > +\tilde{n_e}.
\end{aligned} \tag{1.3-5}$$

Here, we assume that the ion moves in only slow time scale due to the large mass compared with that of the electron ($\tilde{\boldsymbol{v_i}} = 0,\ \tilde{\boldsymbol{n_i}} = 0$). In the development of the formula by using perturbation method, each equations are given by

$$\begin{aligned}
&\frac{\partial}{\partial t}(< n_e > +\tilde{n_e}) + \nabla[(< n_e > +\tilde{n_e})((< \boldsymbol{v_e} > +\tilde{\boldsymbol{v_e}}))] \\
&= \frac{\partial}{\partial t}(< n_e > +\tilde{n_e}) + \nabla[< n_e >< \boldsymbol{v_e} > +\tilde{n_e} < \boldsymbol{v_e} > + < n_e\tilde{\boldsymbol{v_e}} > \tilde{n_e}\tilde{\boldsymbol{v_e}}] = 0.
\end{aligned} \tag{1.3-6}$$

Since the averaged equation is

$$\frac{\partial}{\partial t} < n_e > +\nabla[< n_e >< \boldsymbol{v_e} > + < \tilde{n_e} \cdot \tilde{\boldsymbol{v_e}} >] = 0, \tag{1.3-7}$$

the equation (1.3-6) is rewriten as

$$\frac{\partial}{\partial t}\tilde{n_e} + \nabla[\tilde{n_e}\tilde{\boldsymbol{v_e}} + \tilde{n_e} < \boldsymbol{v_e} > + < n_e\tilde{\boldsymbol{v_e}} > - < \tilde{n_e} \cdot \tilde{\boldsymbol{v_w}} >] = 0. \tag{1.3-8}$$

The dimensions analysis of Eq. (1.3-8) is written by

$$\begin{aligned}
&\frac{\tilde{n_e}}{\tau} + \tilde{n_e}\tilde{v_e}\left(\frac{1}{\lambda}\right) + < n_e > \tilde{v_e}\left(\frac{1}{\lambda} + \frac{1}{L}\right) + \tilde{n_e} < v_e > \left(\frac{1}{\lambda} + \frac{1}{L}\right) \\
&- < \tilde{n_e} \cdot \tilde{v_w} > \left(\frac{1}{L}\right) = 0.
\end{aligned} \tag{1.3-9}$$

We compare each term of Eq. (1.3-9) as follows

$$\frac{v_e}{\lambda} \gg \frac{< v_e >}{\lambda} \tag{1.3-10}$$

$$\frac{v_e}{L} \gg \frac{< v_e >}{\lambda} \tag{1.3-11}$$

$$\tilde{n_e}\tilde{v_e} \approx < \tilde{n_e}\tilde{v_e} > \tag{1.3-12}$$

$$\frac{\tilde{n_e}\tilde{v_e}}{\lambda} \gg \frac{< \tilde{n_e}\tilde{v_e} >}{L} \tag{1.3-13}$$

And, they are related to

$$\frac{L}{\tau} \; > \; \frac{\lambda}{T} \; \gg \mid \tilde{v_e} \mid > < \tilde{v_e} > . \tag{1.3-14}$$

We solve the equations of each scale based on these dimensions. As fast scale equation of electron, the perturbation component is given by,

$$\frac{\partial \tilde{c_e}}{\partial t} + < v_e > \nabla \tilde{v_e} + \tilde{v_e} < v_e > + \frac{e}{m}[E + \frac{1}{c} < v_e > \times \tilde{B}] = 0. \tag{1.3-15}$$

From the relation of $\nabla \times \tilde{E} = -\frac{1}{c}\frac{\partial B}{\partial t}$, $\frac{B}{c} = \frac{\tau}{\lambda}E$. Thus, the dimension is written by

$$\frac{\tilde{v_e}}{\tau} = \frac{e}{m}[\tilde{E} + \frac{\tau}{\lambda} < v_e > \tilde{E}]. \tag{1.3-16}$$

Here, the dimension is compared as $\frac{\lambda}{\tau} \gg < v_e >$, and the equation of motion is written by

$$\frac{\partial \tilde{v_e}}{\partial t} = \frac{e}{m}\tilde{E}. \tag{1.3-17}$$

Furthermore, by using the average equation of electron motion, i.e.,

$$\frac{\partial < v_e >}{\partial t} + < v_e > \nabla < v_e > + < \tilde{v_e} \nabla \tilde{v_e} > \tag{1.3-18}$$

$$= \frac{e}{m}[< E > + \frac{1}{c} < v_e \times B >] - \frac{T_e}{M} \nabla \ln(\mathrm{n_e}), \tag{1.3-19}$$

and the averaged equation i.e.,

$$\frac{\partial}{\partial t} < n_e > + \nabla[< n_e >< \boldsymbol{v_e} > + < \tilde{n_e} \cdot \tilde{\boldsymbol{v_e}} >]. \tag{1.3-20}$$

we solve the slow scale equation. Here, $\tilde{v_e} \nabla \tilde{v_e}$ in Eq. (1.3-20) is de-formulated by $\nabla \times \tilde{v_e} = -\frac{e}{mc} \tilde{B}$, i.e.,

$$\begin{aligned} \tilde{v_e} \nabla \tilde{v_e} &= \frac{1}{2} \nabla < \tilde{v_e}^2 > - < \tilde{v_e} \nabla \tilde{v_e} > \\ &= \frac{1}{2} \nabla < \tilde{v_e}^2 > + \frac{e}{mc} < \tilde{v_e} \times \tilde{B} > \end{aligned} \tag{1.3-21}$$

Therefore, the slow scale equation of electron motion is rewritten by

$$\begin{aligned} &\frac{\partial < v_e >}{\partial t} + < v_e > \nabla < v_e > + \frac{1}{2} \nabla < v_e^2 > \\ &= \frac{e}{m}[< E >] - \frac{T_e}{M} \nabla \ln < \mathrm{n_e} > \end{aligned} \tag{1.3-22}$$

In considering the scale of $< E >= -\nabla \phi$, the dimension equation is rewritten by

$$\begin{aligned} &\frac{< v_e >}{T} + \frac{< v_e >^2}{L} + \frac{1}{2} \frac{< \tilde{v_e}^2 >}{L} \\ &= -\frac{e}{m} \nabla \phi - \frac{1}{2} \nabla < \tilde{v_e}^2 > - \frac{T_e}{M} \nabla \ln < \mathrm{n_e} > . \end{aligned} \tag{1.3-23}$$

$< \tilde{v_e}^2 > \gg < v_e >^2$ is satisfied due to $\frac{L}{T} \ll < v_e >$ and $\mid \tilde{v_e} \mid > < v_e >$ so that the slow scale equation is given by

$$\frac{1}{2} \nabla < \tilde{v_e}^2 > = -\frac{e}{m} \nabla \phi - \frac{T_e}{M} \nabla \ln < \mathrm{n_e} > \tag{1.3-24}$$

By the same calculation of ion, the ion fluid equation is given by

$$\begin{aligned}\frac{\partial v_i}{\partial t} + v_i \nabla v_i &= -\frac{me}{2M}\nabla < v_e^2 > -\frac{T_i}{M}\nabla \ln(\mathrm{n_i}) \\ &= -\frac{e^2 Z}{4mM\omega_0^2}\nabla < E >^2 -\frac{T_i}{M}\nabla \ln(\mathrm{n_i})\end{aligned} \tag{1.3-25}$$

Here, the laser ponderomotive force for ion is defined as the first term of righthand side equation.

$$F_{pi} = -\frac{e^2 Z}{4mM\omega_0^2}\nabla < E >^2 \tag{1.3-26}$$

And, the the laser ponderomotive force for electron is also written as

$$F_{pe} = -\frac{e^2}{4m^2\omega_0^2}\nabla < E >^2 \tag{1.3-27}$$

A laser field irradiated to a high density solid medium is reflected by free electrons near the surface. As a result, the laser couldn't directly interact with the solid material in the inside region, and electrons accelerated from the surface mainly determine the generated plasma states through the collisional process and excitation of the field. As for the physical mechanism of such accelerated electron, various models have been proposed depending on the incident angle of the laser field and the surface structure of the solid as seen in Fig. 1.5.

Among them, there are 「vacuum heating」 [11] and 「 J × B heating」 [12] as a typical solid surface acceleration mechanism. The heat absorption rate by vacuum heating can be estimated from the energy balance between the electric field driven by the charge separation in the vertical direction of the solid surface $E_p = 2E_0 \sin\theta$ and the electric field of the obliquely incident laser $E(x,t) = E_L \sin(\omega_L t - k_0 t)$. From Poisson equation, the electric field concerning the density of the electron, i.e., n_e, which is emitted into the vacuum area, is given by

$$\Delta E = -4\pi e \int_{-\Delta x}^{x=0} n_e \mathrm{dx} = 4\pi \mathrm{en_e \Delta x}. \tag{1.3-28}$$

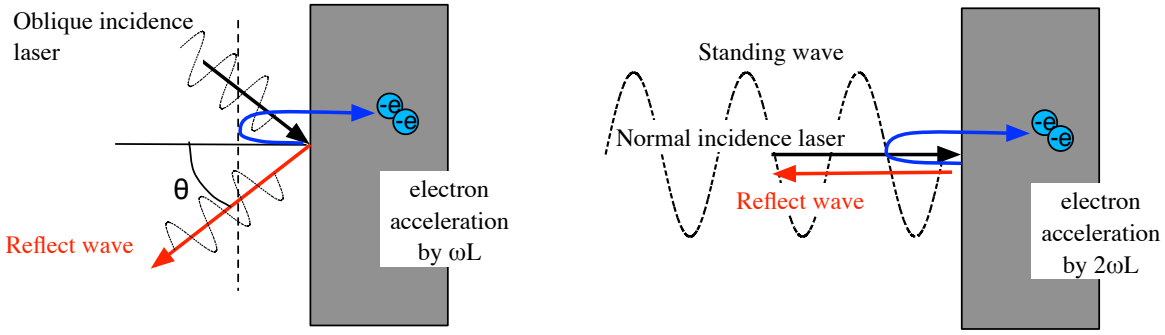

(a) Vacuum heating (b) J×B heating

Fig1.5: Electron heating model with sharp solid surface

From $n_e = N_e/A\Delta x$, where A is the surface area of the solid and N_e in the total electron number in the vacuum region, the electric field is derived from

$$\frac{N_e}{A} = \frac{2E_0 \sin\theta}{4\pi e}. \tag{1.3-29}$$

By assuming the absorbed energy for emitted electrons $\varepsilon_{arb} = \frac{1}{2}N_e m_e v_e^2$, the energy absorption rate per unit area f_{vh} is defined as

$$f_{vh} = \frac{1}{A}(\frac{d\varepsilon_{arb}}{dt}) \simeq \omega_L \frac{1}{2}\frac{N}{A} m_0 v_0^2 \simeq \omega_L \frac{E_0 \sin\theta}{4\pi e}\frac{1}{2} m_0 v_0^2 \tag{1.3-30}$$

From the addition of the laser field $E_L \cos\theta$ and the electrostatic field $E_0 \sin\theta$, since the electron velocity resulting from the acceleration to the perpendicular direction is $v_d = 4v_{osc}^2 \sin^2\theta (E_L \simeq E_0)$, the absorption rate for the oblique incidence laser field could be estimated as

$$f_{vh} = \frac{8eE_0}{m_0\omega_0 c \sin^3\theta} = 8\frac{v_{osc}}{c}\sin^3\theta. \tag{1.3-31}$$

On the other hand, Brunel et al proposed the more detailed model (Fig. 1.6(a)) as

$$f_{vh} = \frac{\eta}{2\pi}\frac{v_{osc}^3}{v_L^2 c\cos\theta} \tag{1.3-32}$$

Here, η is the energy loss of the election oscillation. Later on, Kato et al. assumed that this coefficient depends on the density of the solid, and derived the relation of $\eta \simeq 1/(1-\omega_0^2/\omega_{pe}^2$(Fig. 1.6(b)).

In these ways, in the obliquely incident laser, the electrons on the solid surface are

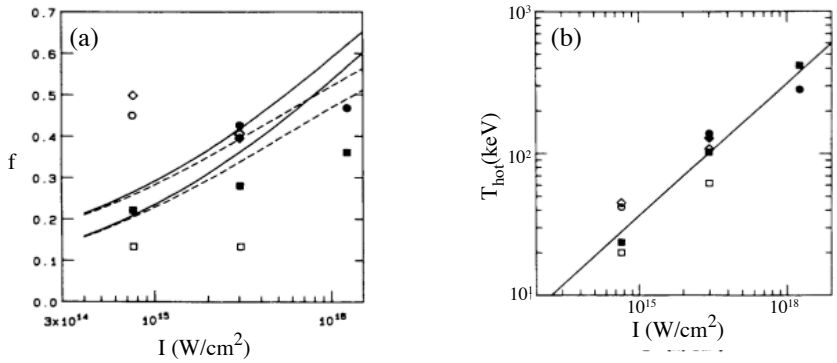

Fig1.6: Absorption rates of vacuum heating[11]

heated by the oscillation of the laser field. On the other hand, 「J × B heating」 for the vertical incidence of the laser field is also a heating mechanism driven by the laser ponderomotive field. It is obtained not by averaging of single particle motion, i.e.,

$$f_p = -\frac{1}{T_L}\int_0^{T_L} dt \frac{1}{4}\frac{e^2}{m_e\omega_L} \bigtriangledown E^2(\vec{r},t), \tag{1.3-33}$$

but from the field profile of the standing wave $E(x,t) = 2E_L(x)\sin(\omega_L t)$ including indent and reflected components, i.e.,

$$f_{p'} = -\bigtriangledown (\frac{m_e v_{osc}^2}{2}\frac{4\omega_0^2}{\omega_{pe}^2}e^{-2\omega_{pe}x/c})[\frac{1+\cos 2\omega_0 t}{2}]). \tag{1.3-34}$$

This equation shows the ponderomotive force acting within the epidermal length on the solid surface. This force oscillates twice as fast as the laser cycle, but the electrons on the solid surface are constantly received by forces in the solid inner direction. For this 「J × B heating」 , Malka and Miquel proposed a model equation of electron energy associated with laser energy[13, 14] as

$$T_{hot} \approx \left(\sqrt{1+\frac{I\lambda_p^2}{2.8\times 10^{18}}} - 1\right) 511\text{keV}. \tag{1.3-35}$$

The mechanism of electron heating depends not only on the incident angle of these lasers but also on the non-uniform structure of the plasma surface. Here, we assume a nonuniform plasma whose density increases in proportion to the propagation distance z as seen in Fig. 1.8. The S-polarized electric field irradiated with the incident angle θ has

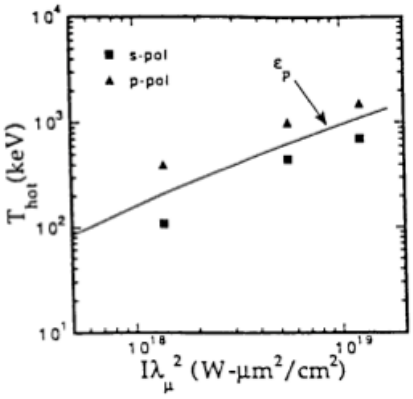

Fig 1.7: Electron energy scaling of $\boldsymbol{J} \times \boldsymbol{B}$ heating compared with the experimental results in the irradiation of P- and S-polarized lasers[14]

an x component $E(z)e^{-i\omega t+k_y y}$ and satisfy the relation as

$$\frac{\partial^2 E(z)}{\partial z^2} + (\frac{\omega}{c})^2(\epsilon - \sin^2\theta)E(z) = 0. \tag{1.3-36}$$

When $\epsilon - \sin^2\theta$ of this differential equation is 0, the electromagnetic field could not propagate to the inside. In the plasma, this field propagates as follows

$$E_x = 2(\frac{\omega}{ca})^{\frac{1}{6}} E_0 A_i(z) \tag{1.3-37}$$
$$E_y = 0 \tag{1.3-38}$$
$$E_z = 0 \tag{1.3-39}$$

Here, a is the scale length of the density and $A_i(z)$ is a Airy function which is determined by $\frac{1}{\sqrt{\pi}}\int_0^\infty \cos(\frac{u^3}{3} + uz)du$. In the same way, the S-polarized magnetic field irradiated with the incident angle θ has a y component $B(z)e^{i(-\omega t+k_y y)}$ and satisfy the relation as

$$\frac{\partial^2 B(z)}{\partial z^2} + \frac{\omega^2}{c^2}(\epsilon - \sin^2\theta)B(z) = 0 \tag{1.3-40}$$

From the relation of Faraday's law and the solution of this differential equation, the electromagnetic field in the plasma is given by

$$E_x = 0 \tag{1.3-41}$$
$$E_y = -\frac{i\omega}{ac}\ln(\frac{\omega}{c}z\sin\theta)B_i(z) \tag{1.3-42}$$
$$E_z = -\frac{1}{az}B_i(z) \tag{1.3-43}$$

$$B_i(z) = E_0 \frac{4\tau A_i(\tau^2)}{\sqrt{(2\pi\omega/ca)}} \sqrt{(\frac{A_i(\tau^2)}{A_i'(\tau^2)})}, \quad \tau = (\frac{\omega}{ca})^{\frac{1}{3}} \sin\theta \tag{1.3-44}$$

The P-polarized electromagnetic field has an electric field component in the propagation

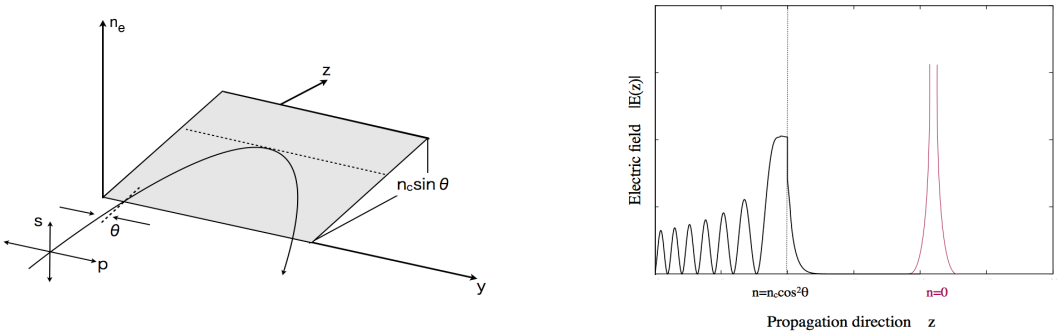

Fig1.8: Electron heating model with pre-plasma

direction. As a result, when the dielectric constant reaches 0, the electric field with large amplitude is excited. If it is similar to spring motion with a natural frequency, it will be easy to understand this mechanism. The frequency of the plasma coincides with the that of the electromagnetic field, and the energy of the electromagnetic field at that location is all converted into the oscillation energy of the plasma. This is the resonance absorption in the non-uniform plasma. Assuming that the plasma with a density structure of $n_e = n_c \mathrm{exp}\,(-\mathrm{z/L})$, the absorption rate is given by [17]

$$f_A = 1 - \exp\left(-\frac{8\nu_{\mathrm{e,i}}\mathrm{L}}{3\mathrm{c}}\cos^3\theta\right) \tag{1.3-45}$$

Here, $\nu_{e,i}$ are collisional frequency between each species of ion and electron, and it is proportion to $n_i Z^2/(T_e)^{3/2}$. Thus, the absorption rate becomes a higher value in the region where the plasma density is high. As the plasma temperature is high, the absorption rate also decreases with decreasing of the collision frequency.

1. 4 Significance of atomic process in laser and solid interaction and purpose of my research

Ionization and plasma dynamics typified as discharge and lightning process are the key to various academic applied technologies. The plasma including neutral atoms, molecules, multiply charged ions, and electrons are generated, which are coexisted through complicated atomic processes, collisional processes. Despite being studied about these problems during more than a century, such plasma generation mechanism has not been elucidated in principle. Therefore, it has old and new physical meaning. Furthermore, with the recent increase of the laser power, the high-intensity laser not only produces plasma but also accelerate the electrons to a relativistic region. The plasma generated through the interaction between such high-intensity laser and a solid medium will become a high energy density state in laboratory system[11]. The physical properties of the high-temperature plasma have a wide spatiotemporal scale with macro structure exceeding the Debye length from the micro atomic process inside the Debye length so that it becomes a synergistically complicated state.

Comparing with the gas/liquid medium, where the laser propagates inside the plasma, the generated plasma in the solid medium has a lot of states since the laser is reflected at the surface. Therefore, the ionization structure inside the solid progresses simultaneously with the various interaction phenomena resulting in a more complicated plasma state. However, the simulation and theoretical studies are assumed to the arbitrary plasma states as the initial condition so that the ionization process of the plasma, in which neutral atoms, multiply charged ions, and electrons are intermixed, has not been clarified yet. And also, the plasma involves the non-uniformity of the density and the instability of electromagnetic field. As a result, the divergence of high-speed electrons, diffusion due to the temperature gradient, etc. are caused by the complexity of the ionization structure increases. To predict and control these conditions, a new theory and simulation system that describes the time transition of the plasma state from multiple ionization models is required for that.

In this thesis, we investigated plasma dynamics coupled with ionization processes in an interaction between a solid medium and a high-intensity laser in the range of $I = 1.0 \times 10^{18-23}$ W/cm^2 as seen in Fig. 1.9. In the range of such laser intensity, high-Z atoms are ionized to the fully stripped state or the higher charge state. For instance, an aluminum is fully ionized by the field with more $I = 2.8 \times 10^{20}$ W/cm^2, and a iron is also fully ionized by the field with more than $I = 1.3 \times 10^{22}$ W/cm^2. However,

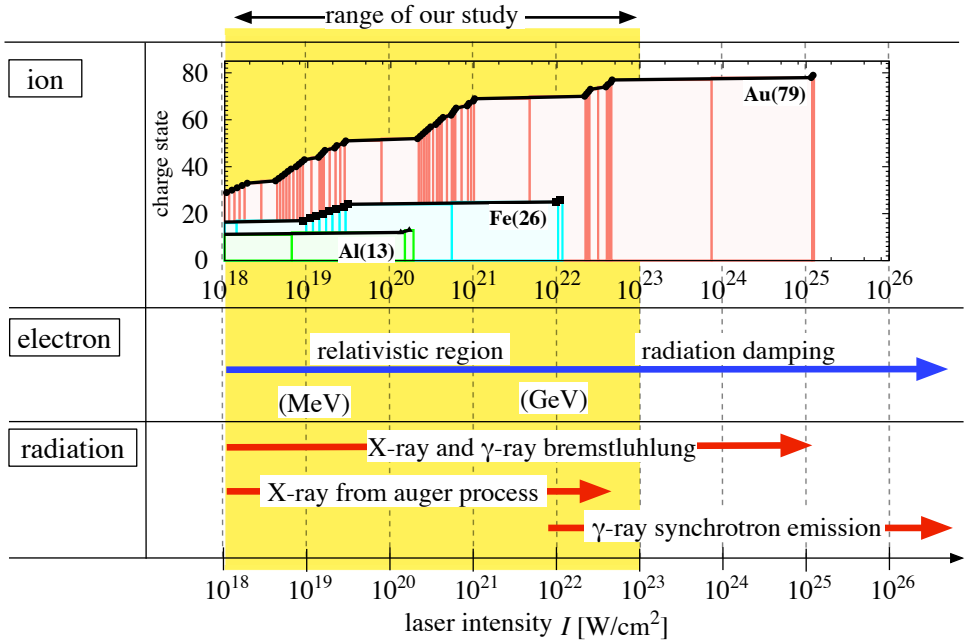

Fig1.9: Laser intensity range of this thesis and the expected dynamics

higher-Z atoms such as gold remain as multiply charged state even in the laser intensity $I = 1.0 \times 10^{23}$ W/cm^2. Furthermore, the ionization process inside of the solid becomes more complicated with the charge distribution ionized by the collisional process. On the other hand, electrons accelerated by such fields reaches to the relativistic region. In the solid medium, these transport characterizes the ionization and the heating processes, which is non-locally determined by the longer collisional mean free path. When the irradiated laser intensity reaches around $I = 1.0 \times 10^{22}$ W/cm^2, radiation damping effect for the accelerated electron takes place. Furthermore, intense-X-ray and γ-ray from the various process are emitted in this range. Bremsstrahlung process dominantly takes place in such high-density plasma, which energy depends on the ion charge state through ion-election collision. The other is radiative excitation from hollow ion which is generated by the inner-ionization process. And, in higher laser intensity more than $I = 1.0 \times 10^{22}$ W/cm^2, γ-ray synchrotron emission through the electron radiation damping takes place. Some experiment utilizes these X-ray and γ-ray spectrum for measurement of plasma condition. In high-density plasma composed of such high-Z material, these fields carry out the energy transport in the solid medium instead of the electron transport.

The outline of this thesis is as follows

- In section 2, we first introduce the plasma particle simulation code which self-

consistently incorporates ionization process and collisional relaxation process (EPIC; Extended Particle-based Integrated Code) and studies the ionization process using this code. In this research, I extend this code to include the detailed ionization process such as ionization loss and inner-ionization, etc, and radiation process of Bremsstrahlung, radiative excitation, and radiation damping effect.

- In section 3, the details of ionization dynamics of a carbon thin film irradiated by high power short pulse laser in the range of 10^{19-20} W/cm^2 are shown. Two types of ionization dynamics exhibiting different spatio-temporal structures are found to regulate the process predominantly, which emerge depending on the laser amplitude. One is the fast convective propagation for the charge state up to C^{4+}, which keeps a steep ionization front. The velocity of the front is in the same order as the speed of light. This results from the formation of the localized longitudinal electrostatic field and associated field ionization, which turns to propagate inside the film. The trigger of such a convective propagation takes place when the laser field becomes high enough that the electron bunch accelerated by the laser ponderomotive force reaches to a relativistic energy and tends to penetrate inside the film across the surface. The other is the fast non-diffusive propagation of ionization showing a long plasma density scale length for C^{5+} and C^{6+}. This process results predominantly from the electron impact ionization by high energy electron bunches successively produced by the laser. These electron bunches also excite wake fields which propagate insides the film and contribute to ionize the film to higher charge state, i.e. C^{5+} and C^{6+}, especially near the front surface. The effect of field ionization loss, which sensitively influences on the ionization dynamics in relatively lower laser power regime, is also discussed.

- In section 4, ionization dynamics in high-Z solid target is discussed for the laser propagation direction. It is found that ionization wave propagates with the electron transport for laser transverse direction. Here, we investigated the ionization dynamics of an aluminum film in 2-dimensional. Around laser spot area, the field ionization to Al^{11+} which is the final state of L-shell proceeds with the electric field as discussed in the above. After the ionization to the propagation direction, the ionization wave of Al^{11+} also propagates to the laser transverse direction beyond the laser spot area. However, the amplitude of the electric field on the ionization front gradual decreases due to the electron diffusion with the spread to the transverse direction, and the impact ionization rate becomes larger than that of the field. Therefore, the velocity

of the ionization wave with Al^{11+} is decelerated with the propagation to the transverse direction. Additional to these rapid ionization processes, Al^{12+} and Al^{13+} are ionized by the sheath field excited on both surfaces.

- In section 5, ionization of a thin film irradiated by a high-intensity short pulse laser in the range of $I = 10^{20-22}$ W/cm^2 and associated acceleration of multiply charged high-Z ions are shown. Two kinds of acceleration mechanisms that cause different types of longitudinal electrostatic fields are found to attribute to the generation of highly charged ions with the kinetic energy in the order of 10 MeV/u. One is the radiation pressure acceleration (RPA) in which both the laser field dominantly ionizes atoms around the front surface of the film to higher charge state and accelerates them toward the inside of the film. The other is the target normal sheath acceleration (TNSA) in which the electrostatic sheath field penetrated inside the film from the rear surface also ionizes atoms to multiple charge states and accelerates them into the vacuum region. For TNSA mechanism, we derived the theoretical scaling of the peak ion energy for each charge state, where the amplitude of the electric field corresponding to the ionization potential is assumed. It correctly describes the ion energy of each charge state in the range that the field ionization dominantly takes place. It is found that the multiply charged ion of the rear surface is accelerated to the maximum ion energy in considering only the gold film even if the highest charge state of ion is ionized at the front surface interacted by the laser field.

- In section 6, the main results are concluded and several open problems are proposed for the extension of this work.

2 Extended particle in cell code (EPIC)

2. 1 Introduction

We developed extended particle in cell code (EPIC) which includes ionization and radiation processes. In typical plasma simulation models, there are fluid model, Vlasov model, particle model as a method to numerically describe the plasma. The fluid model describes the macroscopic behavior of the plasma, and the Vlasov model describes the kinetics plasma by differentiating the phase space. Comparing with these models, the particle model can handle nonlinear and non-equilibrium plasma by solving the relativistic equation of motion and the Maxwell equation. In this model, the behavior of the plasma is calculated by considering super-particles having a finite weight as the collection of actual particles (electrons, ions). Generally, more than one-hundred super particles are prepared in each mesh so as to reduce noise of short wavelength. The electric field and magnetic field is calculated in every mech as lattice-like space. It is necessary to take the mesh size as the interval of the meshes smaller than Debye length which is based on electron temperature and electron density. While it is possible to analyze the behavior of relativistic plasma at microscopic time intervals, the analysis for the large size plasma and/or in long time requires the large computer memory and the computation time. Therefore, the size that the particle model can describe, is limited to a few hundred μm, and the time scale is limited to a few psec. Since the laser pulse width is assumed to the order of fsec, a particle model is known as an effective method for analyzing the interaction between the high intensity laser and the medium. The detail of such typical particle model has been explained in previous studies and past master's thesis[15]. Therefore, we mainly describe the details of atomic and collisional processes and radiative process which is the important processes in this research.

2. 2 Atomic process

All materials are ionized when they are placed in a high intensity field or high temperature, high density plasma. Particularly in the case of heavy element which has a large number of electrons, the plasma including the multiple charge states is generated through

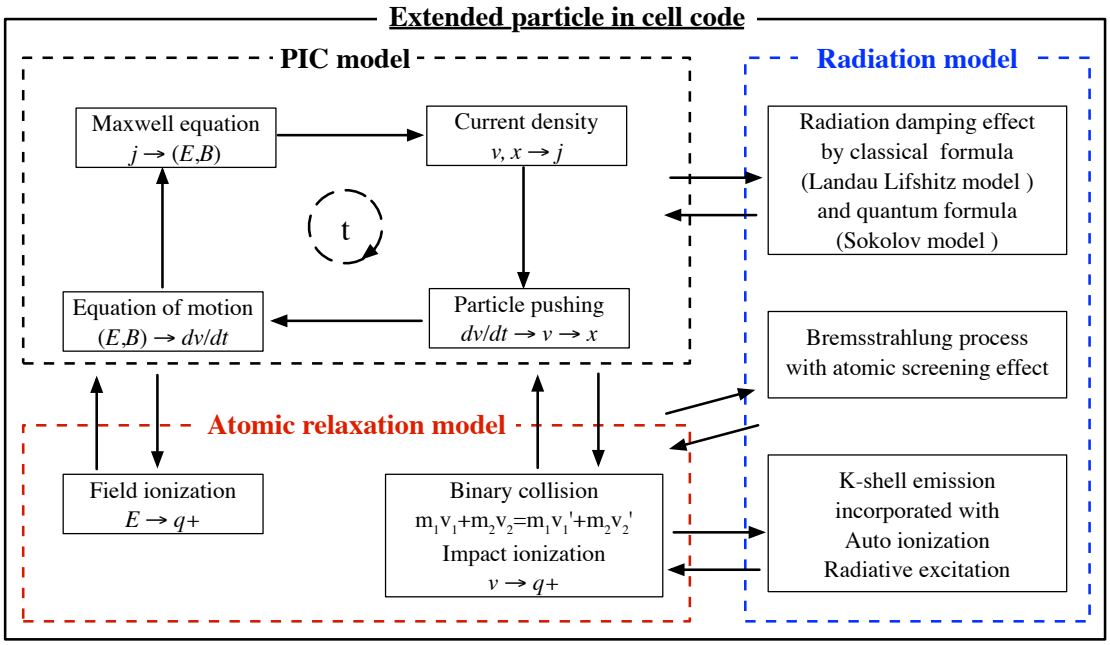

Fig2.1: Extended particle in cell code

some kind of the ionizations. In the interaction between a high-intensity laser and a solid medium, the ions are not only ionized by the laser field. Collisions with electrons heated by a laser field and excitation of an electromagnetic field complicatedly and synergistically progress with such ionization. Therefore, in order to simultaneously analyze these ionization processes, the atomic data that indicates a threshold of ionization are required. In this study, ionization model is constructed from the ionization energy predicted by the wave equation for each element. The ionization process can be analyzed by coupling with the particle model. Figure. 2.2 shows atomic datas which are fundamental properties of this analysis. The energy potential of hydrogen is 13.4 eV. As the atomic number increases, the ionization energy of the inner shell electrons increases. In the case of gold with atomic number 79, the ionization energy required for the inner shell reaches 95.2 keV, which is mostly 7000 times value of hydrogen. Since there is an energy threshold for each electron orbit and electron shell, it becomes possible to understand the plasma condition from the ionization degree.

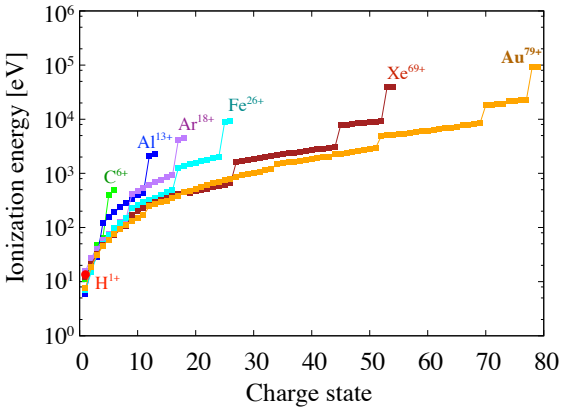

Fig 2.2: Ionization potential for each atom. Here, hydrogen(H), carbon(C), aluminium(Al), argon(Ar), iron(Fe), xenon(Xe), and gold(Au) are shown.

2. 3 Collisional ionization model

2. 3. 1 Collisional relaxation process

In the plasma, elastic collision or inelastic collision (ionization process) is caused by electrons and ions. Usually, the particle model describes each particle motion and electromagnetic field via mesh, and it does not consider the interaction of microscopic areas (microscale) such as the collisions and the scattering process among particles inside of the mesh. However, the solid medium has high density state, and the collisional relaxation process has an important role in such condition. In the EPIC codes, the collisional relaxation process including the relativistic effect has been introduced[16][17]. Information on the charge state of the target atom (quantum number, atomic energy potential, presence or absence of electron occupation, etc.) is assigned to each PIC particle. Here, we make three kind of pairs (electron-electron, ion-ion, and electron-ion) in one mesh by Monte Carlo method (Fig. 2.3(a)). If the number of particles in the mesh is an odd number, the group are generated for three particles. Since the distance between the particles does not have a physical meaning, it is possible to evaluate by the order of $N/2$ without considering all the pairs of which order is N^2.

For collision between particles, there are elastic collision and inelastic collision (impact ionization process) for each particle species. Let consider each collision probability P_K for the collision of K species. Here, the probability of some scattering is given by $P = \sum_{K=1}^{K} P_K$. By using Monte Carlo method, it is necessary to decide three process, i.e., (1) presence or absence of collision, (2) type of collision, and (3) momentum conservation through collision. We divide the unit interval [0, 1] for describing the collision of K species occurring with the probability P_K. If a uniform random number of [0.1] is in

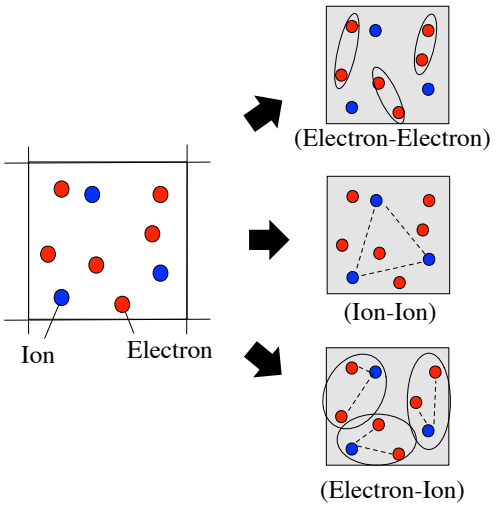

(a) Particle paring in mesh

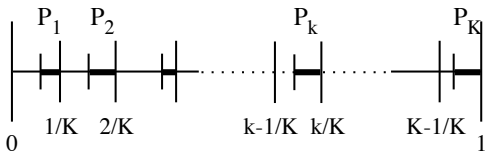

1. Generate a random number U.

2. Calculation of probability P_k by using $k=1+UK$

3. Collision of k is happen for $U>(k/K)-P_k$

(b) Evaluation of the collisional process by using Montecarlo method

Fig2.3: Pairing method using Montecarlo scheme

the interval P_k, then a collision of K occurs, and no collision occurs in otherwise (Fig. 2.3(b)). The collision process evaluates the velocity and scattering angle of the particle after the collision by the momentum conservation law between pair particles. By assumed the velocity in rest mass frame, and Lorentz factor are $\mathrm{v_j}$, $\mathrm{m_{j,0}}$, $\gamma_\mathrm{j}(\mathrm{j}=1,2)$ in the laboratory system of particles 1 and 2 selected by pairing, the particle velocity in the center of mass frame is given by

$$
\begin{aligned}
&v_{cm} = \frac{m_1 \boldsymbol{v}_1 + m_2 \boldsymbol{v}_2}{m_1 + m_2}. \\
&(*m_j = \gamma_j m_{j,0})
\end{aligned}
\tag{2.3-1}
$$

Here, Lorentz transformation to the laboratory system is as follows

$$
\begin{aligned}
&\boldsymbol{x}' = \boldsymbol{x} + \frac{\gamma_{cm} - 1}{v_{cm}^2}(\boldsymbol{v_{cm}} \cdot \boldsymbol{x_1})\boldsymbol{v_{cm}} - \gamma_{cm} t \boldsymbol{v_{cm}} \\
&\frac{d\boldsymbol{x_1'}}{dt} = \boldsymbol{v_1} + \frac{\gamma_{cm} - 1}{\boldsymbol{v_{cm}^2}}(\boldsymbol{v_{cm}} \cdot \boldsymbol{v_1})\boldsymbol{v_{cm}} - \gamma_{cm}\boldsymbol{v_{cm}} \\
&t' = \gamma_{cm}\left(t - \frac{\boldsymbol{v_{cm}} \cdot \boldsymbol{x_1}}{c^2}\right) \\
&\frac{dt'}{dt} = \gamma_{cm}\left(1 - \frac{\boldsymbol{v_{cm}} \cdot \boldsymbol{v_1}}{c^2}.\right)
\end{aligned}
\tag{2.3-2}
$$

Thus, the velocity of particle 1 in center of mass frame is given by

$$\begin{aligned} \boldsymbol{v_{1,cm}} &= \frac{d\boldsymbol{x'}}{dt}\frac{dt}{dt'} \\ &= \frac{(\gamma_{cm}-1)\frac{\boldsymbol{v_{cm}}\cdot\boldsymbol{v_1}}{v_{cm}^2}\boldsymbol{v_{cm}} + \boldsymbol{v_1} - \boldsymbol{\gamma_{cm}}\boldsymbol{v_{cm}}}{\gamma_{cm}(1-\frac{\boldsymbol{v_{cm}}\cdot\boldsymbol{v_1}}{c^2})} \end{aligned} \tag{2.3-3}$$

This relation also applies to particle 2.

Assuming the particle mass of the particle in the center frame to be $m_{j,cm}$, $m_{j,cm} = \gamma_{cm} m_{j,0}$. Using the relativistic mass formulation of particles, this relation is transformed as

$$\begin{aligned} m_{j,cm} &= \gamma_{cm}\frac{m_j}{\gamma_j} \\ &= \gamma_{cm}\left(1 - \frac{\boldsymbol{v_{cm}}\cdot\boldsymbol{v_{j,cm}}}{c^2}\right) \end{aligned} \tag{2.3-4}$$

As easily confirmed from Eqs. (2.3-3), (2.3-4), the sum of the particle momentum in the center of mass frame is preserved, i.e.,

$$\boldsymbol{p_{1,cm}} + \boldsymbol{p_{2,cm}} = m_{1,cm}\boldsymbol{v_{1,cm}} + m_{2,cm}\boldsymbol{v_{2,cm}} = 0 \tag{2.3-5}$$

Next, let consider the scattering process in the center of mass frame. The momentum is preserved before and after scattering as follows

$$\mid \boldsymbol{p_{1,cm}} \mid = \mid \boldsymbol{p_{2,cm}} \mid = \mid \boldsymbol{p'_{1,cm}} \mid = \mid \boldsymbol{p'_{2,cm}} \mid = p \tag{2.3-6}$$

For the velocity after the collision, we assume the transformation as Fig. 2.4. We show the relation between the momentum $\boldsymbol{p}$ and the coordinate axis, and the process of rotating the momentum vector to the z axis. First, the matrix that rotates $\boldsymbol{p}_{1,cm}$ around the z axis by $-\phi$, is determined by

$$\boldsymbol{M_1} = \begin{pmatrix} \cos\phi & \sin\phi & 0 \\ -\sin\phi & \cos\phi & 0 \\ 0 & 0 & 0 \end{pmatrix} \tag{2.3-7}$$

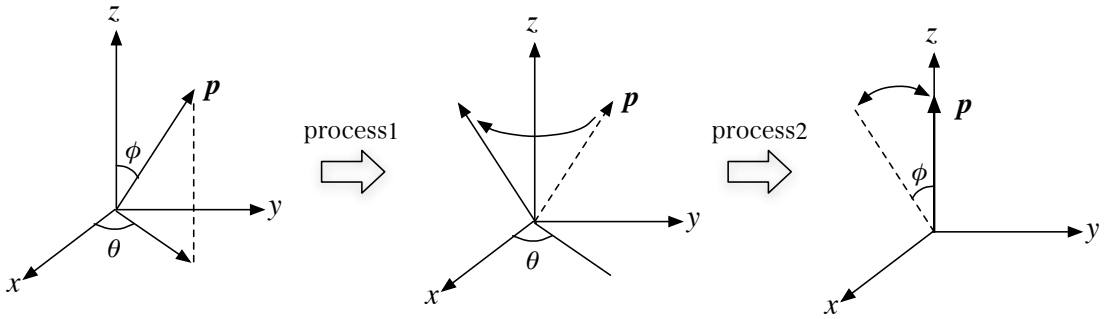

Fig2.4: Conversion of particle momentum vector toward the z axis

The matrix that rotates by θ around the y axis is determined by

$$\boldsymbol{M_2} = \begin{pmatrix} \cos\phi & 0 & -\sin\phi \\ 0 & 1 & 0 \\ \sin\phi & 0 & \cos\phi \end{pmatrix} \tag{2.3-8}$$

The rotation matrix that overlaps arbitrary vectors on the z axis is given by

$$\begin{aligned} \boldsymbol{M} &= \boldsymbol{M_2} \circ \boldsymbol{M_1} \\ &= \begin{pmatrix} \cos\phi\cos\phi & \cos\phi\sin\phi & -\sin\phi \\ -\sin\phi & \cos\phi & 0 \\ \sin\phi\cos\phi & \sin\phi\sin\phi & \cos\phi \end{pmatrix} \end{aligned} \tag{2.3-9}$$

Therefore, the momentum matrix transformed as

$$\begin{pmatrix} 0 \\ 0 \\ p \end{pmatrix} = \begin{pmatrix} \cos\phi\cos\phi & \cos\phi\sin\phi & -\sin\phi \\ -\sin\phi & \cos\phi & 0 \\ \sin\phi\cos\phi & \sin\phi\sin\phi & \cos\phi \end{pmatrix} \begin{pmatrix} p_{x,cm} \\ p_{y,cm} \\ p_{z,cm} \end{pmatrix} \tag{2.3-10}$$

Next, let consider the collision and scattering process. We assume the momentum vector after the collision as

$$(0\ 0\ p) \rightarrow (p\sin\Theta\cos\Phi\ \ p\sin\Theta\sin\Phi\ \ p\cos\Theta) \tag{2.3-11}$$

Here, Θ is determined from the collision frequency of small angle scattering, and Φ is a uniform random number between $(0, 2\pi)$. The matrix M^{-1} is determined by

$$\boldsymbol{M^{-1}} = \begin{pmatrix} \cos\phi\cos\phi & -\sin\phi & \sin\phi\sin\phi \\ \cos\phi\sin\phi & \cos\phi & \sin\phi\sin\phi \\ -\sin\phi & 0 & \cos\phi \end{pmatrix} \tag{2.3-12}$$

The momentum after the collision in the center of mass frame is given by

$$\begin{aligned} \begin{pmatrix} p'_{x,cm} \\ p'_{y,cm} \\ p'_{z,cm} \end{pmatrix} &= \boldsymbol{M^{-1}} \begin{pmatrix} p\sin\Theta\cos\Phi \\ p\sin\Theta\sin\Phi \\ p\cos\Theta \end{pmatrix} \\ &= \begin{pmatrix} p\cos\phi\cos\phi\sin\Theta\cos\Phi + -p\sin\phi\sin\Theta\sin\Phi + p\sin\phi\sin\phi\cos\Theta \\ p\cos\phi\sin\phi\sin\Theta\cos\Phi + p\cos\phi\sin\Theta\sin\Phi + p\sin\phi\sin\phi\cos\Theta \\ -p\sin\phi\sin\Theta\cos\Phi + p\cos\phi\cos\Theta \end{pmatrix} \end{aligned}$$

Here, assuming the momentum to vertical direction is defined as $p_{perp} = (p_x^2 + p_y^2)^{\frac{1}{2}} = p\sin\theta$, the variation of the momentum due to scattering $\Delta\boldsymbol{p_{cm}} = \boldsymbol{p'_{cm}} - \boldsymbol{p_{cm}}$ is given by

$$\begin{pmatrix} \delta p_{x,cm} \\ \delta p_{y,cm} \\ \delta p_{z,cm} \end{pmatrix} = \begin{pmatrix} \frac{p_{x,cm}}{p_{perp}} p_{z,cm}\sin\theta\cos\phi - \frac{p_{x,cm}}{p_{perp}} p\sin\Theta\sin\Phi - p_{x,cm}(1-\cos\Theta) \\ \frac{p_{y,cm}}{p_{perp}} p_{z,cm}\sin\theta\cos\phi - \frac{p_{y,cm}}{p_{perp}} p\sin\Theta\sin\Phi - p_{y,cm}(1-\cos\Theta) \\ p_{perp}\sin\Theta\sin\Phi - p_{z,cm}(1-\cos\Theta) \end{pmatrix}$$

The momentum in the center of mass frame for the particles 2 is determined by

$$\boldsymbol{p'_{1,cm}} = \boldsymbol{p_{1,cm}} + \Delta\boldsymbol{p_{cm}} \quad \boldsymbol{p'_{2,cm}} = \boldsymbol{p_{2,cm}} + \Delta\boldsymbol{p_{cm}}. \tag{2.3-13}$$

Thus, the speed in the center frame after collision is calculated using the expression Eq. (2.3-4) is given by

$$\boldsymbol{v'_{j,cm}} = \frac{\boldsymbol{p'_{j,cm}}}{m_{j,cm}} \tag{2.3-14}$$

By transformation of the velocity $\boldsymbol{v_j} \rightarrow \boldsymbol{v'_{j,cm}}$, $\boldsymbol{v_{cm}} \rightarrow -\boldsymbol{v_{cm}}$, the velocity in laboratory frame is given by

$$\boldsymbol{v'_{j,cm}} = \frac{(\gamma_{cm}-1)\frac{\boldsymbol{v_{cm}}\cdot\boldsymbol{v'_{j,cm}}}{v_{cm}^2}\boldsymbol{v_{cm}}+\boldsymbol{v'_{j,cm}}+\gamma_{cm}\boldsymbol{v_{cm}}}{\gamma_{cm}(1+\frac{\boldsymbol{v_{cm}}\cdot\boldsymbol{v'_{j,cm}}}{c^2})}. \tag{2.3-15}$$

Here, we solve the scattering angle after collision. the collisional frequency with respect to charges q_1, q_2 from the theoretical Coulomb scattering formula is given by

$$\nu = \frac{4\pi n(q_1 q_2)^2}{m_r^2 \gamma_2 u^3}\ln\Lambda. \tag{2.3-16}$$

Where, n is particle density, u is relative velocity in the center of mass frame, γ is relativistic factor for u, and m_r is conversion mass. And, $\ln\Lambda$ is Coulomb logarithmic which is determined as 10 in this thesis. Assuming that the time step for collision calculation is Δt_c, the scattering angle Θ is determined by

$$\tan\left(\frac{\Theta}{2}\right) = \delta \tag{2.3-17}$$

, which is determined by the random number along

$$< \delta^2 > \equiv \nu\gamma_{cm}\Delta t_c. \tag{2.3-18}$$

Based on these collisional process, collision for each PIC particle is able to be described.

2. 3. 2 Electron impact ionization

If the energy of electrons is larger than the binding potential of the charge state during the collision between the free electron and the charged ion, the ionization probability occurs. One of the formulas for obtaining the ionization cross section σ is proposed by Kim et al. as follows

$$\sigma^{BEB} = \frac{4\pi a_B^2 N(R/B)^2}{t+\frac{1}{n(q+1)}}\left(\frac{\ln t}{2}\left(1-\frac{1}{t^2}\right)+1-\frac{1}{t}-\frac{\ln t}{t+1}\right) \tag{2.3-19}$$

Where, $a_B = \hbar^2/m_2^2 = 5.29\times10^{-9}$cm is Bour radius, N is bounded electron number, $R(=13.6\text{eV})$ is Rydberg energy, and B is bounded energy for the charge state. And,

$t = E/B$ is kinetic energy of the free electron normalized by the bounded energy, n is quantum number, q is netcharge. The theoretical model that derives the cross-section is

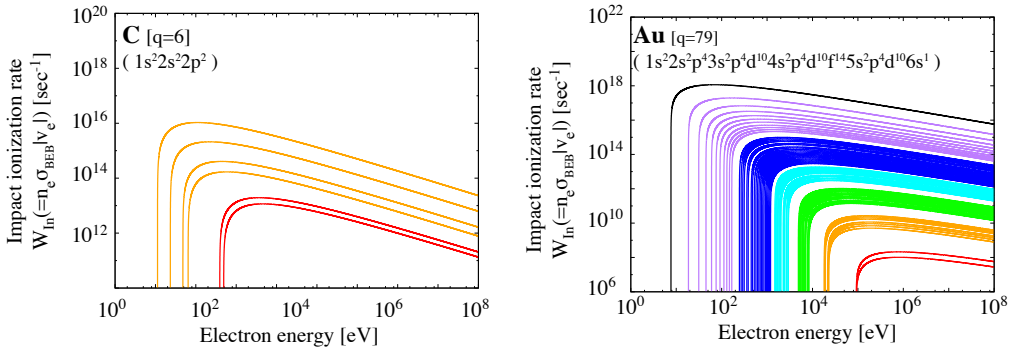

Fig2.5: Electron impact ionization rate based on BEB model[18]

named as the BEB (Binary Encounter and Bethe approximation) model by Kim et al[18]. With respect to the electron impact ionization cross section, various formulas in each condition have been proposed including empirical formulas have been proposed. Among them, the expression (2.3-19) is known to coincide well with experiments on a wide range of studies. Therefore, in this simulation code, the collisional ionization rate was obtained by adopting the equation (2.3-19) as the electron impact ionization cross section. The collision ionization rate is calculated as $W_{ln} = n_e \sigma_{BEB} |ve| \Delta t_c$ using the local free electron density n_e and the collision electron velocity v_e.

Figure 2.5 shows the relations between the collision ionization rates of the carbon C with up to $q = 6$ and the gold Au with $q = 79$ with respect to the colliding electron energy. When the energy of colliding electrons reaches the ionization potential, the ionization rate rapidly increases, and then the rate tendency gradually decreases as same in both atoms. In addition to that, as the number of bounded electrons increases, the ionization potential of the inner shell increases. Compared to the inner shell electrons of gold, the energy of bounded electrons at which the inner shell electrons of carbon is as small as two orders.

2. 4 Field ionization

2. 4. 1 Boundary between multi photon absorption process and tunnel ionization process by Keldysh parameter

When the intensity of the electromagnetic field is weak, multi photon ionization dominantly takes place. On the other hand, when the electromagnetic field becomes strong, the electromagnetic field ionizes the electrons through the tunnel effect which changes the Coulomb field of the atom. Whether the ionization processes is determined by the Keldysh parameter[19], i.e.,

$$\gamma = \omega \frac{\sqrt{2mB}}{eE} = (\frac{B}{2\phi_p})^{\frac{1}{2}} \tag{2.4-20}$$

Where, ω is laser frequency, m_e is electron mass, B is ionization potential, E_0 is the intensity of the laser electric field, and $\phi_p (= e^2E^2/4m_w\omega^2)$ is ponderomotive potential. The mutiphoton ionization becomes dominant in $\gamma \gg 1$ while the tunnel field ionization in $\gamma \ll 1$. If the ionization rate W is obtained, the probability of ionizing Δt in the simulation time step is given by $R = 1 - \exp[-W\Delta t]$. From the uniform random number U of [0,1], ionization occurs in $R > U$.

Figure 2.6 shows Keldysh parameters of carbon (C) and gold (Au) with respect to the laser wave length λ = 800nm. In common property with both atoms, the boundary of the ionization types $\gamma = 1$ changes at 10^{13} W/cm^2. At less than this intensity, multi photon absorption process dominantly takes place. As the atomic number increases, the ionization potential of the inner shell increases, and the multi photon absorption process dominates in a wide intensity range. However, in this multi photon absorption process, the numerical noise of the electric field has to be considered. Noise level when 100 particles are added per mesh ($Te = 1\text{eV}, \text{n}_{\text{i,e}} = 6.0 \times 10^{22}\text{cm}^{-3}$) reaches to 10^7 W/cm^2, and the multi photon ionization will occurs. Furthermore, if the particles are more heated, the noise level increases. It is suggesting that the noise also affects ionization process to higher charge state. Therefore, by considering only tunnel ionization in this simulation, the influence of ionization process due to noise is reduced.

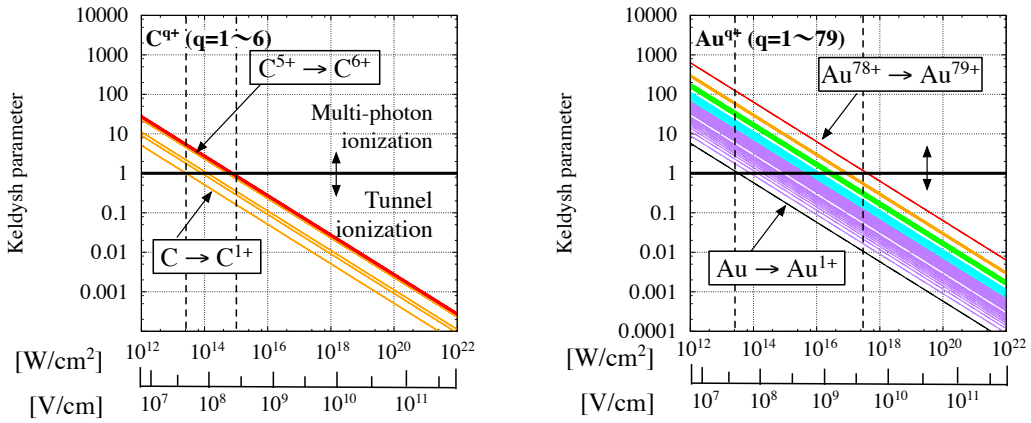

Fig2.6: Keldysh parameters of carbon (C) and gold (Au) with respect to the laser wave length $\lambda = 800$nm

2. 4. 2 Tunnel field ionization

When an electromagnetic field affects on a single atom, the probability of the tunnel ionization during time Δt is determined by

$$R = 1 - \exp[-W_F \Delta t]. \tag{2.4-21}$$

Here, W_F is the tunnel ionization rate proposed by Ammosov et al [20] as follows

$$W_F = \omega_A C^2 n, l\bar{U} \frac{(2l+1)(l+m)!}{2^m m!(l-m)!} \left(\frac{2\bar{E}_0}{\bar{E}}\right)^{2n^*-m-1} \exp\left(-\frac{2\bar{E}_0}{2\bar{E}}\right) \tag{2.4-22}$$

$$C^2_{n^*,l^*} = \frac{2^{2*}}{n^*\Gamma(n^*-l^*)\Gamma(n^*+l^*+1)}.$$

Where, $\omega_A = me^4/\hbar = 4.134 \times 10^{16}\text{sec}^{-1}$ is atomic frequency, $n^* = Z(2\bar{U})^{-\frac{1}{2}}$ is quantum number for Z, $\bar{U} \equiv U/E_H$ is Hartree potential, and $E_H = 27.4$eV is normalized ionization potential. l, m are azimuthal quantum number and magnetic quantum number, respectively. And, $l^* = n_0^* - 1$ is effective azimuthal quantum number for the effective quantum number n_0^*. From $\bar{E}_0 = (2\bar{U})^{\frac{2}{3}}$, $\bar{E} = E/E_A$ is normalized by $E_A = 5.14 \times 10^9$ V/cm, the gamma function is determined by $\Gamma = \int_0^\infty x^n e^{-x} dx$. This formula is a standard model for tunnel ionization, and the ionization probability of PIC particles is determined. Figure 2.7 shows the tunnel ionization rate of the carbon and gold. The carbon atom starts to be

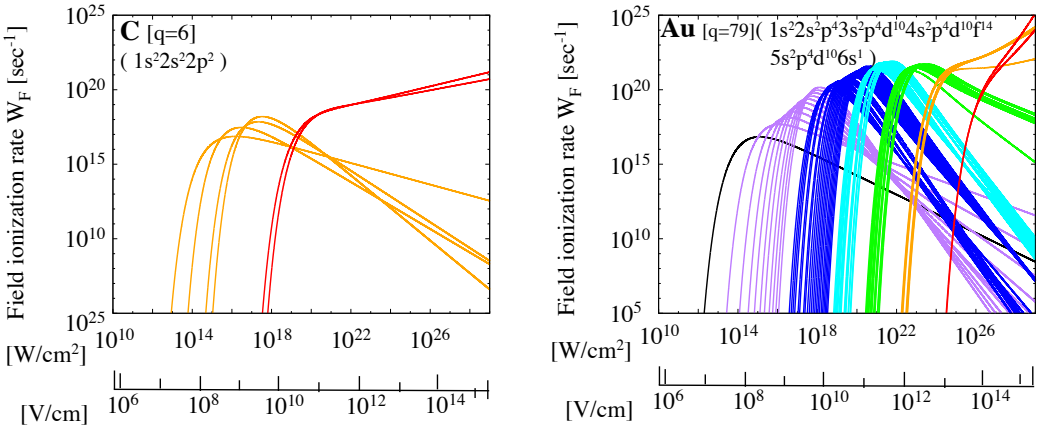

Fig2.7: Tunnel ionization rate proposed by Ammosov et al[20]

ionized to the outer shell electrons from approximately 10^{13} W/cm^2, and the fully ionized state is generated by the laser intensity 10^{13}W/cm^2. Also, there is a large gap between the ionization potentials among the atomic nuclei constituted by carbon, and correspondingly the electric field intensity as the ionization threshold becomes large. For the result of this carbon atom, the larger electric field intensity is required for tunnel ionization of gold with $q = 79$. The ionization threshold of the outer shell electrons is of the same order, but the ionization to the inner shell state requires the larger intensity than the ionization threshold of the carbon atom. This tunnel ionization to the full ionized state requires an electric field intensity more than 10^{25} W/cm^2, resulting in a larger 12 digit than the carbon threshold. With the development of the laser technology, achievement of the laser intensity 10^{22} W/cm^2 has been reported. If the direct interaction with the laser field is considered, the transition of the carbon atom to the fully ionized state is easily possible, but for gold only ionization to the M shell occurs. The ionization degree inside the solid where the laser does not directly affect becomes an important parameter to measure the plasma state.

2. 5 Radiation process

When a target medium is irradiated by a high intensity laser, high energy density plasma is generated. If the material is low-Z, a fully ionized plasma is generated, and the absorbed energy is carried mainly by electron heat transport. In this case, the electron heat transport isn't able to handle by diffusion approximation, and non-local transport becomes important. On the other hand, in a case that the high intensity laser is irradiated to a high-Z medium, a model for determining the ionized state of ions is required. And, the absorbed laser energy becomes to be transported through the radiation process, which will influence the plasma dynamics and the ionization process in some cases. For example, if the material is gold (Z=79), the majority of absorbed laser energy is converted to X-rays, and the radiation transport dominates the formation of the high energy density plasma instead of the electron heat transport. Even in a lower-Z material such as plastic (CH), a several % of the absorbed energy is converted to X-ray energy and preheats the solid at the front region. From these contexts, in laser plasma research, it is necessary to describe the X-ray and γ-ray emission by using numerical models and combine with the particle model to solve the transport and the absorption. In recent research, by using high intensity lasers in the range of $I = 10^{22-23}$ W/cm^2, it is also expected that the plasma dynamics are dominated by quantum electromagnetism (QED) processes such as radiation and pair generation.

In the interaction between the higher intensity laser field and the high-Z medium, not only high-energy particles but also high-brightness X-rays and γ -rays are responsible for the energy transport and the transition of the generated plasma state. To study the complex plasma science, in which the particles and the radiations are strongly coupled, it is required the analysis of the fundamental characteristics of theoretical and numerical calculation. However, due to the performance of current computers, the mesh size is limited around 1 nm only with the conventional particle model that tracks the behavior of plasma, and radiation fields with shorter wavelengths aren't able to be described. Therefore, even if the environment where high-intensity lasers can be easily used in the laboratory, it is difficult to design the detailed experiments under the present condition that the theoretical system and numerical analysis method are not established.

Here, we introduce the radiation models, (1) Bremsstrahlung process coupled with the collisional process, (2) the excitation radiation process caused by the inner shell ionization, and (3) the radiation damping by electron accelerating motion in the field. In nest sections, the detail of each radiation model is explained.

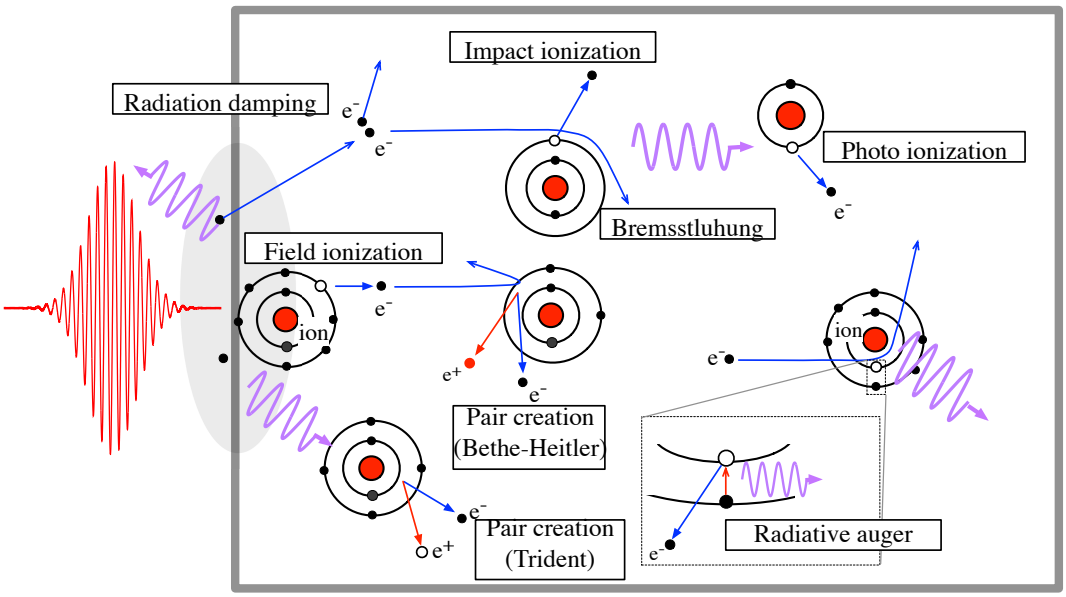

Fig2.8: Atomic and radiative processes in the high intensity laser interaction with high-Z solid

2. 5. 1 Bremsstrahlung process

In an interaction between a high-intensity ($I > 1.0 \times 10^{18}$ W/cm^2) laser and plasmas, many applications utilizing high-Z medium have been studied as heavy ion accelerator, laser fast ignition, and so on. In these studies, high brightness X-ray with the energy over 20 keV from the high energy density plasma has also been reported in Ref[23, 23] It results from the non-thermal bremsstrahlung process through the collisions of the high energy electrons e^- with multiply charged ions qe^+. Here, the collided electrons are generated by the direct laser acceleration on the target surface, and their energies reach the relativistic region according to the laser ponderomotive force. On the other hand, the ion charge state q depended on the atomic number Z theoretically contribute to increasing the X-ray brightness with $\propto q^2$. Therefore, the radiation loss becomes a non-negligible for the plasma dynamics in the condition without the re-absorption to the plasma in the optically thin system. This escaped component also becomes a measurement source for the information of plasma temperature, density, etc.

In previous theoretical research, the X-ray emission has been evaluated by using particle-in-cell code (PIC) coupled with the relativistic binary collision model by using the Monte Carlo method[25]. It is useful for the evaluation of the hard-X-ray emission from the non-stationary plasma composed of the non-thermal and non-isotropic electrons. Most of the simulation work using PIC scheme initially assume the full ionized state or arbitrary state

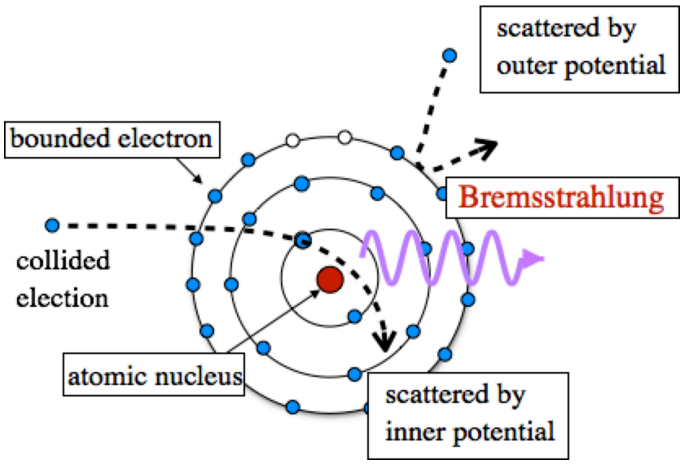

Fig 2.9: Illustration of the bremsstrahlung process. the collided electron is scattered from the outer potential or the inner potential of the multiply charged ion. In our code, these processes included into PIC scheme.

predicted by thermal equilibrium theory. However, the ionization state is non-stationary during the laser interaction and transits in response to the excitation of the electric fields and the heating of electrons and ions. Especially in solid media such as iron and gold, the internal ionization structure becomes an important parameter for bremsstrahlung process since the laser field is reflected from the surface. In the collision of the high energy electron with the multiply charged ion, the injected electron is probabilistically scattered from the inner atomic potential of each bounded state. It has an important role in evaluating electron scattering angle and emitted X-ray energy.

In this code, bremsstrahlung process is integrated to PIC scheme by using the Monte Carlo method for the differential cross sections of the electron-ion collision and the relativistic bremsstrahlung. First, an electron scattering angle is estimated from the binary collisional process based on the cross-section in Spitzer thermal theory;

$$\nu_{e-i} = \frac{4\pi n q^2 e^4}{m_e^2 \gamma_2 v_e^3} \ln\Lambda. \tag{2.5-23}$$

Where, n is ion density, v_e is electron velocity, γ is relativistic factor for v_e, and m_e is electron mass. And, $\ln\Lambda$ is Coulomb logarithmic defined as λ_D/b_{min}, where λ is Debye length, and b_{min} is minimum impact parameter which approximated to $h/\gamma m_e v_e$ from Plank constant h as de Broglie wavelength. Here, we extend the Coulomb logarithmic term to include the screening Coulomb potential of the partially charged ion as follows

$$\nu_{e-i} = \frac{4\pi n e^4}{m_e^2 \gamma_2 v_e^3} \left[q^2 \ln\frac{\lambda_D}{a_q} + Z^2 \ln\frac{a_{Z-1}}{b_{min}} + \sum_{q'=q+1}^{Z-1} q'^2 \ln\frac{a_{q'-1}}{a_{q'}} \right], \tag{2.5-24}$$

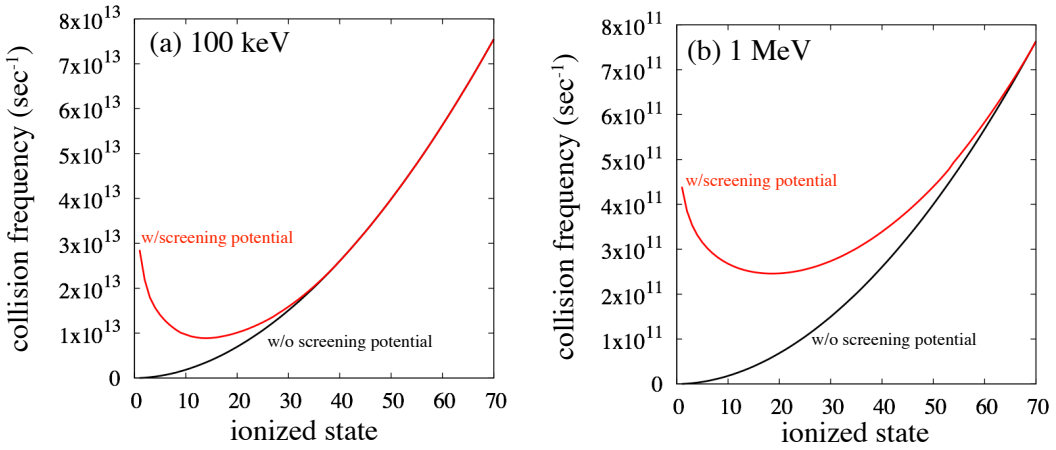

Fig2.10: Collisional cross-section with- (red line) and without- (black line) screening potential for the injected electron energy 100 keV and 1.0 MeV

where, each atomic radius a_q is approximated from ionization potentialE_q, i.e.,

$$a_q = \frac{2E_q}{qe^2}.$$

Figure 2.10 shows the collisional cross-sections with- and without the screening potential of the ion with the ionized state q, which are calculated for the injected electron energy 100 keV (a) and 1.0 MeV (b), respectively. In the case without the screening effect, the electron is scattered by the only outer potential of the ion so that the cross-section with lower charged ion is small. However, the cross-section with the screening effect becomes larger than that since the injected electron could penetrate into the ion. This process remarkably affects in the collision of the injected electron with the higher energy as seen in Fig. 2.10. Thus, the screening effect coupled with the ionization process becomes the important role in evaluating the bremsstrahlung process in the laser interaction with the high-Z medium. When the uniform random number r is less than the cross-section $\nu_{e-i}\Delta t$, where Δt is simulation time step, the photon is emitted, and the electron scattering angle is determined by r following

$$\tan\left(\frac{\Theta}{2}\right)^2 \equiv \nu\gamma_{cm}\Delta t_c. \tag{2.5-25}$$

Second, we calculate the photon energy from the differential cross-section of bremsstrahlung. The range of the emitted photon energy $[\hbar\omega_{min} : \hbar\omega_{max}]$ is determined. ω_{min} is determined

by simulation mesh size, i.e., $\omega_{min} = 2\pi\Delta/c$. ω_{max} is determined from Born approximation which is based on the radiation cross-section of the bremsstrahlung. After the collision with the injected kinetic energy $m_e c^2(\gamma - 1)$, the scattered kinetic energy $m_e c^2(\gamma' - 1)$ should be satisfied the condition $Ze^2/\hbar << v'_e$. Thus, the maximum photon energy is determined as $\hbar\omega_{max} = m_e c^2(\gamma - \gamma')$. The emission energy of photon is calculated from the differential cross-section as

$$\begin{aligned}\frac{d\sigma}{d\log_{10}(\omega)} =& Z^2\left(\frac{e^2}{mc^2}\right)^2 \alpha\log(10)\frac{|\boldsymbol{p}'|}{|\boldsymbol{p}|}\left\{\frac{4}{3} - 2\epsilon\epsilon'\frac{p^2+p'^2}{c^2p^2p'^2} + \left(\frac{\eta\epsilon'}{c^3p^3} + \frac{\eta'\epsilon}{c^3p'^3} - \frac{\eta\eta'}{c^2pp'}\right)\right. \\ &+ L\left[\frac{8\epsilon\epsilon'}{3c^2pp'} + \frac{k^2}{p^3p'^3}(\epsilon^2\epsilon'^2/c^4 + p^2p'^2) + \frac{\beta^2 k}{2pp'}\left(\frac{\epsilon\epsilon'/c^2 + p^2}{p^3}\eta\right.\right. \\ &\left.\left.\left. - \frac{\epsilon\epsilon'/c^2 + p'^2}{p'^3}\epsilon' + \frac{2k\epsilon\epsilon'}{c^2p^2p'^2}\right)\right]\right\}\end{aligned} \tag{2.5-26}$$

where $\alpha = e^2/\bar{c}$ is the fine structure, p^i, p'^i, k^i are the momentums of an injected electron, a scattered electron, a photon, respectively. And, the variables are $L = \log[(p^2 + pp' - \epsilon k/c)/(p^2 - pp' - \epsilon k/c)]$, $\eta = \log[(\epsilon/c + p)/(\epsilon/c - p)]$, and $\eta' = \log[(\epsilon'/c + p')/(\epsilon'/c - p')]$. The energy conservation through the emission process should be satisfied as $\epsilon = \epsilon' + \hbar\omega$. In this energy range [$\hbar\omega_{min}$:$\hbar\omega_{max}$], we determine the photon energy by using the random number of $\log[\omega]$ following the cross-section.

Third, the emission angle of photon is calculated from the differential cross-section as

$$\begin{aligned}\frac{d\sigma}{d\omega d\Omega_p\Omega_s} =& \frac{1}{\omega}\frac{Z^2\alpha^3}{4\pi^2}\frac{|\boldsymbol{p}'|}{|\boldsymbol{p}||\Delta\boldsymbol{p}|^4}\left[\frac{\Sigma_\mu(\boldsymbol{\mu}\cdot p'^i)^2}{(p'^i\cdot k^i)^2}(4\epsilon^2/c^2 - |\Delta\boldsymbol{p}|^2)\right. \\ &+ \frac{\Sigma_\mu(\boldsymbol{\mu}\cdot p^i)^2}{(p^i\cdot k^i)^2}(4\epsilon'^2/c^2 - |\Delta\boldsymbol{p}|^2) - 2\frac{\Sigma_\mu(\boldsymbol{\mu}\cdot p^i)(\boldsymbol{\mu}\cdot p'^i)}{(p^i\cdot k^i)(p'^i\cdot k^i)}(4\epsilon\epsilon'/c^2 \\ &\left. - |\Delta\boldsymbol{p}|^2) + 2\frac{k^2\Delta\boldsymbol{p}|^2 - (p^i\cdot k^i - p'^i\cdot k^i)]^2}{(p^i\cdot k^i)(p'^i\cdot k^i)}\right],\end{aligned} \tag{2.5-27}$$

where $d\Omega_p = d\cos\theta_p$ is a solid angle of photon, $d\Omega_s = d\phi d\cos\theta$ is a scattering angle of photon, respectively. For the calculation, the momentum of the injected electron is rotated to z-axis, and the other momentums with each scattering angle and emission angle is given by

$$\begin{aligned} pi &= (\epsilon/c, 0, 0, p) \\ p'i &= (\epsilon'/c, p'\sin\theta\cos\phi, p'\sin\theta\sin\phi, p'\cos\theta) \\ ki &= (k, k\sin\theta, 0, k\cos\theta)\end{aligned}$$

Here, the polarization tensors is determined as perpendicular to momentum $\boldsymbol{k}$, i.e.,

$$\begin{aligned} \mu^{(1)} &= (0, 0, 1, 0) \\ \mu^{(2)} &= (0, -\cos\theta_p, 0, \sin\theta_p). \end{aligned}$$

In this coordinates, the total transfered momentum is given by $|\Delta \boldsymbol{p}|^2 = \boldsymbol{p}^2 + \boldsymbol{p'}^2 + \boldsymbol{k}^2 - 2\boldsymbol{p}\cdot\boldsymbol{k} + 2\boldsymbol{p'}\cdot\boldsymbol{k} - 2\boldsymbol{p}\cdot\boldsymbol{p'}$. From this calculation, the bremsstrahlung process is evaluated with PIC calculation including the time transition of the ion charge state. In the simulation, the energy loss due to the emission is also described correctly from the conservation of the energy and the momentum.

2. 5. 2 Radiative excitation

When high pressure gas is injected into the vacuum, the gas is cooled by an adiabatic expansion, and a part of the gas is condensed to the micro solid clusters. In an irradiation of laser field, clusters effectively absorb laser energy, and partially ionized plasma is generated. It results from both properties of a wide interacted area with laser field as gas material and a large thermal capacity as a solid material. Such interesting feature provides not only understanding of fundamental physics in extreme plasma and also exploring a lot of applications such as an ion acceleration and a generation of the blast wave. One of the important evidence of such interaction is that neutrons originating in the nuclear fusion reactions were observed by using deuterium clusters irradiated with a laser pulse [26]. It indicates that a hot-dense plasma is efficiently generated in cluster media, which was discussed for accelerated ion energy and fusion reaction rate for each cluster size by 2-dimensional particle simulation. [27].

On the other hand, X-ray emission from rare gas clusters such as Ar has been also developed as an intense radiation source driven by a laser pulse. Through an interaction with high intensity laser field above $I = 10^{17}$ W/cm^2, a large number of electrons is heated to over keV, and an Ar cluster is easily ionized up to Ar^{8+}. In such hot-dense plasma, ions are ionized to K-shell state by a collisional process with a high energy electron, and also hollow ions of these states are partially produced through an inner shell ionization. Then, a number of photon in range of X-ray is emitted from a radiative excitation to K-shell. From experimental results, it is found that a brightness of X-ray lines mainly depends on typical times scales of hydrodynamic cluster expansion compared with laser pulse duration. One of the important features in such interaction is that a cluster re-

mains over cut-off density during an irradiation of laser pulse for obtaining high energy absorption to plasma. Recently, strong K-shell X-ray signals are observed from large size Ar cluster ($\simeq 1.0$ μm) irradiated with high intensity ($I > 1.0 \times 10^{19}$ W/cm^2) and short pulse ($\tau = 30$ fs) laser. It indicates that the higher absorption process contributed to the relativistic effect of the oscillated electron more increases the radiation efficiency by selecting the cluster size which is large enough to keep the high density state.

In this code, the transition of the ion charge state q could be described by the both of the optical field ionization and the electron impact ionization corresponded to the time variation of the irradiation of the laser pulse and the heating of the plasma. The field ionization rate is estimated from the ADK formula which based on the local electric field including electromagnetic and electrostatic component. The energy conservation in the simulation system is satisfied to include the field ionization loss which is calculated by applying the virtual current corresponding the ionization energy. On the other hand, the successive binary collisions of particle pairs between electron-electron, electron-ion, and ion-ion are also included for describing the collisional relaxation process. By using this scheme, the electron impact ionization is evaluated for each ion according to the BEB formula. Here, the generation of the hollow ion is also calculated by using the Monte Carlo technique taking into account the ionization rates of the outer shell and the inner-shell. The cross sections of the electron impact ionization in K-shell charge state $q = 8 - 14$ are included in this code, where the ionizations for the valence electron are above lines as $Ar^{8+} - Ar^{14+}$, and that for inner shell electron are below lines as $Ar^{8+*} - Ar^{14+*}$. The rates of $Ar^{8+} - Ar^{14+}$ rise up in the range of less than the electron energy 1.0 keV and then reach the maximum value. The inner shell electrons are strongly coupled with the atom by the higher ionization potential than that of the outer electron so that these ionization thresholds of the electron energy shift to the higher value around the range of a few keV. Furthermore, the cross-section of the inner shell ionization becomes smaller value than that of the outer shell ionization by roughly two orders due to the decreasing of the impact parameter limited within the atomic size. Thus, the generation of double hollow ion is negligible in this scheme since the probability is smaller than that of single hollow generation. Through such ionization, the electron energy impacted with the charged ion is lost to correspond to each ionization potential. By using these schemes, the transition of the ion charge state and the hollow ion generation are described along the laser interaction with the cluster.

After the production of the hollow ion, the electron bounded in K-shell transits to the atomic vacancy through the radiative excitation or the auto-ionization. The coefficients

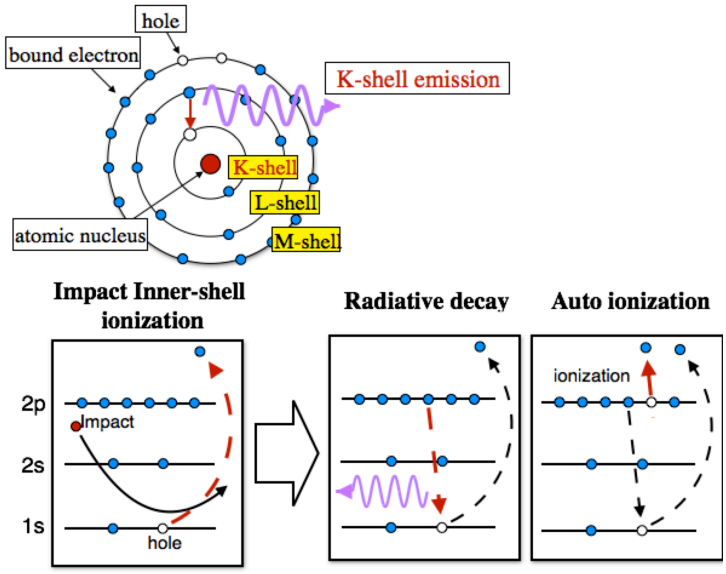

Fig2.11: Illustration of the auger process. The hollow ion is generated by the inner ionization process, and the radiative excitation and the auto ionization takes place.

A_r^q and A_a^q defines the transition rates of the radiative excitation (Einstein's A factor) and the auto-ionization rate as follows

$$A_r^q(q \to 1) = 4.34 \times 10^7 \frac{g_1}{g_q} f_{q,1} E_{q,1}^2 \tag{2.5-28}$$

$$A_a^q(q \to 1) = \frac{2q^2 E^q}{\hbar q^3 \pi^2 a_0^2} \frac{g_1}{g_q} \sigma(q \to 1) \tag{2.5-29}$$

For each hollow ion, the transition or not is also calculated by using the Montecarlo technique based on these rates, i.e., $A_r^q + A_a^q$. Either the radiative excitation or the auto ionization is stochastically selected by the ratio of A_r^q and A_a^q. Each rates of A_r^q and A_a^q in K-shell are mostly same order around $1.0 \times 10^{14}(1/\text{sec})$ so that the same amount of the transition takes place with time scale of 10 fs which is not negligible for the interaction with sub-ten fs laser pulse. The photon number of each X-ray lines is evaluated by the transition amount of such radiative excitation. In this scheme, the ion state is reflected such transitions as the times goes on.

In the cluster irradiated by the high intensity laser field, the ions dynamically move to the expanded direction compared with the interaction with the film target. Thus, the

doppler shift of energetic ion spreads the X-ray spectrum, i.e.,

$$\hbar\omega_q' = \frac{\hbar\omega_q}{1 - |\boldsymbol{v_i}|/c\cos\theta} \tag{2.5-30}$$

Here, ω_q and ω_q' are the emission frequency corresponding the X-ray energy for q and the observed frequency in experimental flame. And, θ is the angle of the ion velocity $\boldsymbol{v_i}$ for the emission direction which is randomly determined for each excitation process. By adopting such scheme for the emission calculation, the broadening of the X-ray spectrum could be described to correspond to the ion temperature.

Here, We performed the test simulation of the ionization and characterized X-ray emission in the interaction between the single Ar cluster and the high intensity laser pulse. The simulation model has assumed the square domain in (x,y) plane with the length $L_x = L_y = 5.12$ μm. The spatial grid size is chosen to $\Delta = 5.0 \times 10^3$ which is small enough to describe the sub-micron cluster shape. Here, the single Ar cluster with the radius $r = 0.1$ μm is settled at the center of that. The ion density is $n_0 = 2.44 \times 10^{22}$ cm^{-3} which is the real value of the Ar solid, and the electron density is initially equal to 0 since the initial charge of the ion is assumed to the neutral state. The laser field with pulse width $\tau = 30$ fs is irradiated into the simulation domain from $y = 0.1$ μm as uniformly in x-direction. The peak laser intensities are assumed to $I = 1.0 \times 10^{18},\ 1.0 \times 10^{19}$ W/cm^2 with the wave length $\lambda = 0.8$ μm, in which the electron is accelerated to the relativistic region. Comparing this simulation, rate equations for each charge state which is mostly used in previous simulation approach is also calculated as

$$\frac{\mathrm{d}N^q}{\mathrm{d}t}(t) = \alpha N_0^q(t) - (A_r^q + A_i^q)N^q(r,t) \tag{2.5-31}$$

$$\alpha = \int < n_e(t) > \sigma_{BEB}^{q=1}(E) v_e f_e(E,t)\mathrm{d}E,$$

where each parameters is averagely calculated in the same simulation.

Figure 2.12 shows the time history of the radiative excitation amount for each analysis in the case of $I = 1.0 \times 10^{18}$ W/cm^2 (a) and $I = 1.0 \times 10^{19}$ W/cm^2 (b). The ion amount of the radiative excitation calculated by the rate equation becomes larger than that which is calculated for each particle. This is due to that the field ionization takes place for the charged ions with $q = 8 - 14$ near the cluster surface. In rate equation, the ionization type is only the electron impact ionization so that this analysis estimates a lot of ion amount

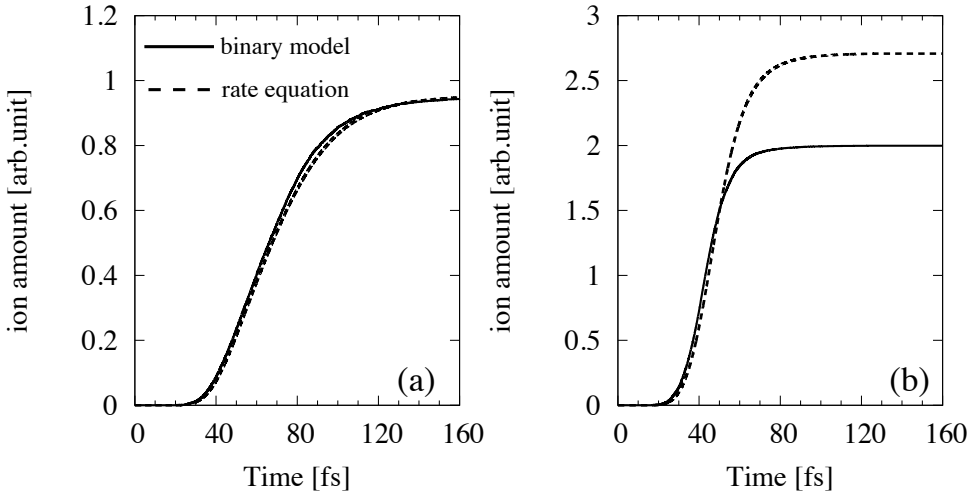

Fig2.12: Ion amount of the radiative excitation evaluated by the rate equation (dashedd line) and the binary model (solid line) for the laser intensity $I = 1.0 \times 10^{17}$ W/cm^2 (a) and $I = 1.0 \times 10^{19}$ W/cm^2 (b)

of the radiative excitation which is originated in the inner collision process. Especially, the field ionization rate has a important role for the radiation in the cluster radius which consists of the large superficial area compared with the film medium. The difference of each analysis becomes larger with increasing of the irradiated laser intensity as seen in Fig. 2.12 (b). Thus, the our apploach integrated into PIC scheme is applicable to the laser interaction with cluster medium.

2. 5. 3 Radiation damping

In the recent development of the laser pulse, the laser intensity tends to exceed $I = 1.0 \times 10^{22}$ W/cm^2 and electrons accelerated by such an intense laser field will reach energies beyond 100 MeV and start to emit radiation. Then the radiation loss from an accelerated electron will no longer be negligible and will affect its motion, i.e., radiation damping takes place. To evaluate the radiative damping effect, we extend the equation of particle motion to Lorentz-Abraham-Dirac equation in PIC scheme. For single particle calculation, the first order damping equation of the LAD equation which is known as Landau-Lifshitz (LL) equation mostly describes the stationary solution of the LAD equation in the classical regime[27]. The applicability of the LAD equation based on classical electrodynamics to the extreme intense laser-matter interaction regime is also discussed using the Schwinger parameter[28,29]. The critical electric field for quantum electrodynamics, i.e., Schwinger

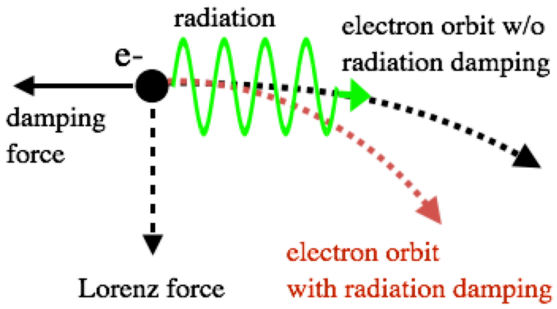

Fig 2.13: Illustration of the radiation damping process. The accelerated electron receive the damping force with radiation reaction.

field E_s is given by

$$E_s = \frac{m_e^2 c^3}{e\hbar}, \tag{2.5-32}$$

which corresponds the intensity $I \simeq 1.0 \times 10^{29}$ W/cm^2. Quantum effects for an accelerated electron within the Compton wavelength $\lambda_c = \hbar/m_e c$ is based on the dimensionless parameter $\chi = E/E_s$. In relativistic electron motion, it is extended to Lorentz and gauge invariant parameter as

$$\chi = \frac{[F^{ik} v_k]^{1/2}}{E_s}, \tag{2.5-33}$$

where

$$u^i = \begin{pmatrix} \gamma \\ \beta_x \gamma \\ \beta_y \gamma \\ \beta_z \gamma \end{pmatrix}, F^{ik} = \begin{pmatrix} 0 & -E_x & -E_y & -E_z \\ E_x & 0 & -B_z & B_y \\ E_y & B_z & 0 & -B_x \\ E_z & -B_y & B_x & 0 \end{pmatrix}$$

. Thus, the dimensionless parameter in a plane electromagnetic wave is described as

$$\chi = \frac{[m_e c\gamma \boldsymbol{E} + \boldsymbol{p} \times \boldsymbol{B}]^{1/2}}{m_e c E_s} \simeq \gamma(1 - \beta_{//}) \frac{E}{E_s}, \tag{2.5-34}$$

where $\beta_{//}$ is the velocity along the wave propagation. When the laser intensity reaches to $I \simeq 1.0 \times 10^{24}$ W/cm^2 with $\gamma(1 - \beta_{//}) > 300$. In this regime, the classical approach is not applicable to describe the damping force, and the non-perturbative generalization of LAD equation which is proposed by Sokolov[30] account for the quantum effect.
From Larmor formula in the approximation of the non-relativistic limit, the energy con-

servation for the single charged particle is given by

$$\frac{d}{dt}\left(\frac{1}{2}m\boldsymbol{v}^2\right) = \boldsymbol{F}\cdot\boldsymbol{v} - \frac{dI}{dt}, \tag{2.5-35}$$

where

$$\begin{aligned}\frac{dI}{dt} &= m\tau_0 c^2\dot{\beta}^2,\\ \tau_0 &= \frac{e^2}{2mc^3}\end{aligned}$$

It is reformulated as the integral form, i.e.,

$$\int_{-\infty}^{\infty} dt(m\dot{\boldsymbol{v}} - \boldsymbol{F} - m\tau_0\dot{\dot{\boldsymbol{v}}}\cdot\boldsymbol{v}) + [m\tau_0\dot{\boldsymbol{v}}\cdot\boldsymbol{v}]_{-\infty}^{\infty}. \tag{2.5-36}$$

In the condition that $[m\tau_0\dot{\boldsymbol{v}}\cdot\boldsymbol{v}]_{-\infty}^{\infty} = 0$, the equation is rewritten as four dimensional form of LAD equation

$$m\frac{d^2u^i}{d\tau} = \frac{e}{c^2}F^{ik}u^i + \frac{2e^2}{3c^2}\left[\frac{d^2u^i}{d\tau^2} - u^iu^k\frac{d^2u^k}{d\tau^2}\right]. \tag{2.5-37}$$

If the damping term is a small perturbation, the damping term g is extend as Landau-Lifsiz equation

$$m\tfrac{d^2u^i}{d\tau} = \tfrac{e}{c^2}F^{ik}u^i + \sum_{j=0}^{\infty} g_j^i, \tag{2.5-38}$$

where

$$\begin{aligned}\left(\frac{du^i}{d\tau}\right)_0 &= \frac{e}{mc^2}F^{ik}u_k\\ \left(\frac{du^i}{d\tau}\right)_1 &= \left(\frac{du^i}{d\tau}\right)_0 + \frac{2e^2}{3mc^2}g_1^i.\end{aligned}$$

Thus, 1st order damping force and 2nd oder damping force are given by

$$\begin{aligned}g_1^i &= \left[\left(\frac{du^i}{d\tau}\right)_1 - u^iu^k\left(\frac{du_k}{d\tau}\right)_1\right]\\ &\approx -\left(\frac{e}{mc^2}\right)^2\gamma^2 c\beta[(E+\beta\times B)^2 - (\beta\cdot E)^2]\end{aligned} \tag{2.5-39}$$

$$
\begin{aligned}
g_2^i &= [\left(\frac{d^2u^i}{d\tau^2}\right)_1 - u^i u^k \left(\frac{d^2u_k}{d\tau^2}\right)_1] \\
&\approx -\left(\frac{e}{mc^2}\right)^3 \gamma^4 c\beta^2[(E+\beta\times B)^2 \\
&- (\beta\cdot E)^2](E+\beta\times B)
\end{aligned}
\tag{2.5-40}
$$

The effect of each order is compared as follows

$$
\frac{f_{i+1}}{f_i} = \frac{2r_e\omega_0\gamma^2 a_0}{3c^2} = 1.18\times 10^{-8}\gamma^2 a_0.
$$

Here, 2nd damping force affects as same to 1st order one from the laser intensity $I \simeq 10^{22}$ W/cm^2. In this paper, we investigate the laser interaction in the rage of $I = 1.0^{18-23}$ W/cm^2, so that the 1st and 2nd order damping term is introduced into our PIC code.

In this code, the emission energy is determined by the distribution function:

$$
Fr,\chi = 3^{5/2}(8\pi)^{-1} r\left[\int_{r_\chi}^{\infty} K_{5/3}(r')dr' + rr_\chi\chi^2 K_{2/3}(r_\chi)\right], \tag{2.5-41}
$$

where $r = \omega/\omega_c$, and $r_\chi = r/(1-\chi^r)$. Here, the critical frequency ω_c is determined by the survive radius of the particle orbit as $3\dot{\boldsymbol{v}}\gamma^3/2c$ which is calculated using the rotation coordinate as discussed in collisional process. The photon energy $h\bar{\omega}$ is decided by the random number along with the distribution function, and photon number is calculated by the differential cross-section:

$$
\frac{dI}{d\omega} = \frac{1}{\omega} Fr,\chi(g_1+g_2)c. \tag{2.5-42}
$$

In this code, the photon number is given by

$$
n_{pho} = (\frac{dI}{d\omega}\Delta t\Delta^2)/dn_{par}, \tag{2.5-43}
$$

where n_{pho} is photon number and dn_{par} is particle weight, respectively. And, the emission angle is also calculated by the random number following the differential angle cross-section

$$
\frac{dI}{d\Omega} = \frac{7}{16}e^2\frac{\dot{v}}{c}\frac{1}{(1/\gamma^2+\theta^2)^{5/2}}[1+\frac{5}{7}\frac{\theta^2}{(1/\gamma^2+\theta^2)}]. \tag{2.5-44}
$$

In strong relativistic regime, it is approximated to $\delta\left(\Omega - \frac{\boldsymbol{p}}{p}\right)$.

We carried out the test calculation of the laser interaction with the injected single electron as seen in Fig. 2.14. The laser field is irradiated to y direction with the intensity

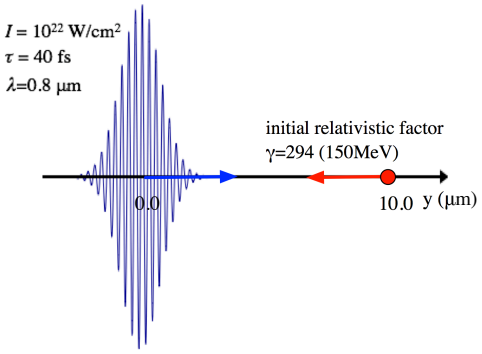

Fig2.14: Simulation model of the laser interaction with single electron.

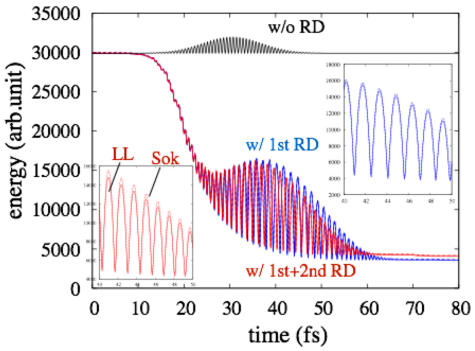

Fig2.15: Time histories of electron energy w/o radiation damping (black line) and w/ 1st order damping (blue line) and 1st and 2nd order damping (red line).

$I = 1.0 \times 10^{22}$ W/cm^2 and the pulse duration $\tau = 40$ fs. The electron is injected from $y = 10.0$ μm to $-y$ direction with the initial electron energy 150 MeV. The simulation time step is chosen to satisfy the CFL condition $\Delta t = 0.05\Delta/c$. Figure 2.15 shows the time history of the electron energies w/o the radiation damping and w/ damping terms g_1 and $g_1 + g_2$, respectively. For checking the damping effect, the radiation damping of Sokolov model is also integrated to the PIC and calculated. In this laser intensity, the damping effect could be described by the classical formula so that the electron energies in Landau-Lifshitz model and Sokolov model mostly becomes the same result. The electron energy with damping effect decrease after the laser interaction compared with that in the case w/o radiation damping. In this case, the difference between each order is only small value. However, the difference will become larger in the case with higher laser intensity.

3 Multi-phase ionization dynamics in solid thin film

3. 1 Introduction

High power short pulse lasers in the range of 10^{18-21} W/cm^2, which easily ionize even heavy atoms and accelerates electrons to relativistic regime, open up a wide class of academic and practical applications such as high energy compact particle accelerator for both ions and electrons[32, 33, 34], high intensity radiation source from tera-hertz[35] to X-rays[36] and also γ-rays[37], generation of high energy density plasma and/or super-shot matter[38], electron-positron pair plasma generation[39], photo-nuclear reaction[40] and neutron generation[41], fast ignition in laser fusion[42, 43]. etc. Various kinds of targets with different state and structure, e.g. gas and/or plasma, solid, clusters[44] etc., are employed according to the purpose.

Correspondingly, many theoretical and computational works have been done for elucidating the interaction such as the propagation and absorption of laser field[45, 46, 47], and associated heating and, heat transport [48, 49], excitation of various kinds of electrostatic and electromagnetic fields[50], etc. Here, it is noted that many of them assume a priori fully and/or partially ionized plasmas, e.g. predicted by the averaged ion model in thermal equilibrium state [51] as their initial condition and simulate subsequent dynamics. However, targets are initially in a neutral state and is ionized during the interaction with laser field through complex atomic process and relaxation process. Specifically, in the case using femto-second short pulse laser, atomic process and also collisional relaxation process are of specifically importance since it provides the initial condition from which primary interaction takes place. As a result, a plasma with highly non-stationary and non-thermodynamic equilibrium is produced, where the electron energy distribution, ion charge state distribution and corresponding ion energy distribution, their temperature and density, etc. evolves transiently[52, 53].

To simulate such a complex state, kinetic model of plasma is crucial since the process is transient and the state is far from non-thermodynamic equilibrium. In this work, by using the extended particle-based integrated code (EPIC) which includes atomic process and collisional relaxation process, we study the details of ionization dynamics of a carbon

thin film in one dimensional configuration irradiated by high power short pulse lasers in the range of 10^{19-20}W/cm^2. It is noted that the study provides a common understanding for the ionization of matter even for those made by high-Z heavy element.

Here, we found that the ionization of the film exhibits multi-phase nature with different spatio-temporal structures depending on the ionization state. Namely, the ionization shows qualitatively different feature for those smaller than C^{4+}, and for C^{5+} and C^{6+}, which results from a large energy gap between $n = 1$ and $n = 2$ (n: principle quantum number). The former leads to the fast convective propagation keeping a steep ionization front with the velocity of 0.6-0.7c for low charge states up to C^{4+}, where c is the speed of light in the vacuum. This results from the formation of localized longitudinal electrostatic field and associate field ionization[54, 55, 56], which turns to propagate inside the film leading to the fast convective propagation. This feature is regarded as a transition from stationary mode to that of propagation, which takes place when the laser field becomes high enough that the electron bunch accelerated by the laser ponderomotive force near the front surface reaches to a relativistic energy and then tends to penetrate inside the film across the surface. The latter is the subsequent fast non-diffusive propagation of ionization displaying long plasma density scale length for C^{5+} and C^{6+}. This process results predominantly from the electron impact ionization by high energy electron bunches successively produced by the laser. These electron bunches also excite wake fields which propagate insides the film and contribute to ionize the film to higher charge state, i.e. C^{5+} and C^{6+}, especially near the front surface. The wake fields are then suffered from damping not only by such ionizations but also by collisions by bulk particles, leading to the heating of the film.

3. 2 Simulation condition

Here, we carry out the simulation of interaction between a diamond-like carbon (DLC) film[62, 63] and a short pulse laser using the EPIC, which is described in Sec.Ⅱ. The simulations are performed in one dimensional capability of the EPIC along y-direction with a computational domain of $-0.62\mu\text{m} \leq \text{y} \leq 3.28\mu\text{m}$, where the system size is $L_y = 3.90$ μm and $y = 0$ μm is chosen at the left-hand side (LHS) surface of the thin film as explained in the folloing. The thin carbon film with a constant density n_1 is set in $y_1 \leq y \leq y_2$, where $y_1 = 0$ μm and $y_2 = 2.87$ μm, so that y_2 corresponds to the thickness of the film. The pedestal (pre-plasma) which density gradually increases from n_0 to n_1

as $n(y) = n_1 \exp(-(y_1 - y)/L_p)$ in $y_0 \leq y \leq y_1$ is assumed, where L_p is the scale length. Here, the density at the front, i.e. $n_0 = n(y_0) = pn_1$, is determined by $p = 10^{-3}$, so that $y_0 = -0.20$ μm. The carbon density is typically chosen to $n_1 = 0.352 \times 10^{23}\text{cm}^{-3}$, which is 1/5 of the diamond carbon density, i.e. $n_{solid} = 1.75 \times 10^{23}\text{cm}^{-3}$. We define the non-relativistic plasma frequency of the charge state q by $\omega_p^{(q)} = (4\pi q n_1 e^2/m)^{1/2}$. Then, the corresponding electron skin depth is defined as $\delta_p^{(p)} = c/\omega_p$. For instance, for a plasma with the ion charge state of $q = 1$ and $q = 6$ (fully ionized plasma), $\delta_e^{(1)}(= c/\omega_p^{(1)}) = 2.84 \times 10^{-2}$ μm and $\delta_e^{(6)}(= c/\omega_p^{(6)}) = 1.16 \times 10^{-2}$ μm are given, respectively.

A linearly polarized short pulse laser which electric and magnetic fields are in x- and z-directions is irradiated along y-direction from the antenna placed at $y = -0.61\mu$m near the LHS boundary. The laser wavelength is $\lambda_\ell = 0.82$ μm, so that the corresponding cut-off density in non-relativistic limit is given by $n_c = 1.658 \times 10^{21}$ cm^{-3}. The laser pulse width is chosen to $\tau_\ell = 40$ fsec (FWHM), which shape is given by a gaussian form as $\exp[-4(t - t_p)^2/\tau_\ell^2]$, where t_p is the time that the laser intensity becomes the peak value. The maximum laser intensity is typically set to $I = 3.247 \times 10^{19}$ W/cm^2, which corresponds to $a_0(\equiv eA_0/mc^2) = 4$ in normalized unit. The mesh number and the width in the y-direction are $N_y = 2432$ and $\Delta y = 1.6 \times 10^{-3}$ μm, respectively. Note that the skin depth is well reproduced even for the charge state $q = 6$ since $\Delta y/\delta_e^{(6)} \sim 0.138$. The time step Δt satisfies the CFL condition as $c\Delta t/\Delta y/ = 0.1$.

3. 3 Simulation result of ionization dynamics

Here, we present the simulation result for the ionization dynamics of the carbon film in the case without and with the field ionization loss in Sec. 3.31 and 3.3.2, respectively.

3. 3. 1 The case without field ionization loss

In Figure 3.1(a), we show the time histories of field energy E_f, which includes both electromagnetic and electrostatic components, electron kinetic energy E_e, ion kinetic energy summed up for all different charge states, $E_i(= \sum_{q=1}^{6} E_i^{(q)})$, where $E_i^{(q)}$ denotes the ion energy for the charge state q, and total energy $E = E_f + E_e + E_i$, respectively. These energies are averaged over whole the system. Also shown the corresponding logarithmic plot for each energy in Fig.3.1(b). From $t \simeq 30$ fsec, the ionization starts when the laser fits the surface of the film. Then the electron energy increases and saturates at $t \simeq 100$ fsec which

roughly corresponds to the time that the laser irradiation ends. The electron energy then decreases while the ion energy increases gradually, suggesting the energy transfer from electrons to ions. Note that even after the laser field reflected at the front of the carbon film is escaped from the LHS boundary, the field energy E_f survives with a certain level as marked by $(*)$ in Fig.3.1 (b) at $t \simeq 110$ fsec from which it decreases gradually with the exponential time dependence. This field mainly corresponds to the sheath field produced at both surface, which accelerates ions into the vacuum.

Figure 3.2(a) illustrates the time histories of ion abundance $\bar{N}_i^{(q)} (\equiv N_i^{(q)}/N_i)$ for each

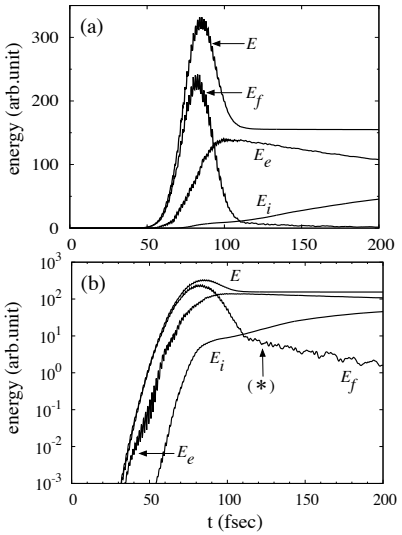

Fig3.1: Time histories of electron energy E_e, ion energy E_i, field energy energy E_f, and total energy $E = E_e + E_i + E_f$ in linear scale (a) and logarismic scale (b).

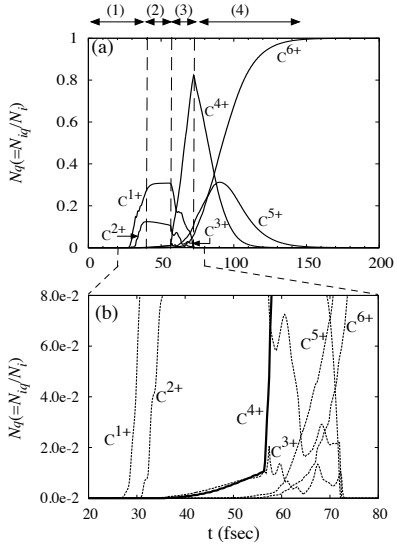

Fig3.2: Time histories of electron energy E_e, ion energy E_i, field energy energy E_f, and total energy $E = E_e + E_i + E_f$ in linear scale (a) and logarismic scale (b).

ion charge state q, where $N_i^{(q)}$ and N_i are the ion number with q and the total ion number contained in the carbon film, respectively. In order to see the details of the ionization dynamics, the region of $20 \leq t \leq 80$ fsec in Fig.3.2(a) is enlarged in Fig.3.2(b). As the laser hits the carbon film, the ionization of C^{1+} and subsequently C^{1+} start to proceed and then saturate around $t = 40$ fsec to $\bar{N}_i^{(1)} \simeq 0.31$ and $\bar{N}_i^{(2)} \simeq 0.12$, respectively. On the other hand, $\bar{N}_i^{(3)}$ and $\bar{N}_i^{(4)}$ gradually increase up to $t \simeq 56$ fsec. Then, $\bar{N}_i^{(4)}$ changes the increasing rate to a higher value and reaches to $\bar{N}_i^{(4)} \simeq 0.8$ at $t \simeq 72$ fsec. Note that C^{3+} produced in $56 \leq t \leq 72$ fsec is quickly ionized to C^{4+}. From $t \simeq 56$ fsec, C^{5+} and C^{6+} are produced gradually with slower rates than those for C^{4+}. C^{5+} saturates around

$t = 90$ fsec while C^{6+} keeps increasing, leading to a fully ionized plasma around $t = 120$ fsec.

In order to understand the complex ionization process shown in Figs.3.1 and 3.2, we classify the process into four phases, i.e., the phase that (1) C^{1+} and C^{2+} increase and saturate ($0 \leq t \leq 40$ fsec), (2) C^{3+} and C^{4+} gradually increase ($40 \leq t \leq 56$ fsec), (3) C^{4+} increases rapidly (almost linearly) and saturates, while C^{5+} and C^{6+} start to increase ($56 \leq t \leq 72$ fsec), (4) C^{6+} gradually increases and saturates leading to a fully ionized plasma ($t \geq 120$ fsec).

Here, we define the quantities $T_F^{(q)}$ and $T_{EI}^{(q)}$, which represent the ratio of ionization

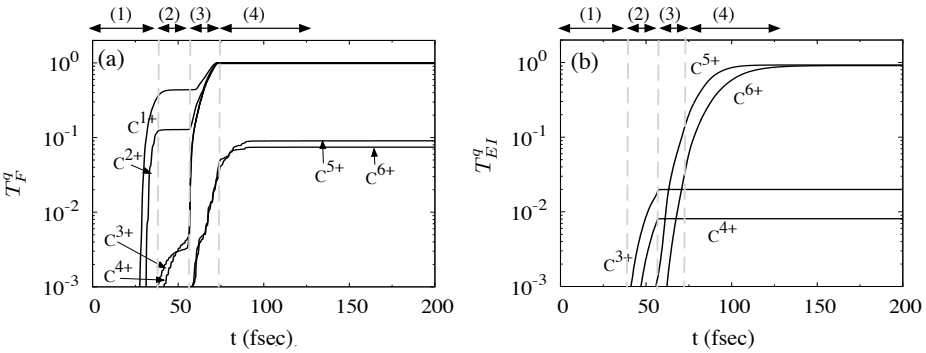

Fig3.3: Time history of ionization ratio generated by field component (a) and impact component (b) for each charge state in logarismic scale. The dashed lines also classify the ionization phases.

component to the charge state q produced by the field (F) and the electron impact (EI) for the total ion number, respectively. Figure 3.3(a) and (b) show the time histories of $T_F^{(q)}$ and $T_{EI}^{(q)}$. In phase (1), C^{1+} and C^{2+} are found to be produced by the field ionization predominantly up to the saturation at $t \simeq 40$ fsec, where $T_F^{(1)} = 0.42$ and $T_F^{(2)} = 0.13$, respectively. In phase (2), the carbon is mainly ionized to C^{3+} and C^{4+} by the electron impact ionization as found from $T_{(EI)}^{(q=3)} = 0.021$ and $T_{(EI)}^{(q=4)} = 0.008$, while $T_{(F)}^{(q=3)} = 0.003$ and $T_{(F)}^{(q=4)} = 0.004$, respectively. However, in phase (3), i.e. after $t \simeq 56$ fsec, C^{3+} and C^{4+} increase predominantly by the field ionization as found from $T_F^{(3)} = 0.979$ and $T_F^{(4)} = 0.992$. On the other hand, C^{5+} and C^{6+} are produced by both field and electron impact ionizations as found from $T_{EI}^{(5)} = 0.12$ and $T_{EI}^{(6)} = 0.028$ at $t \simeq 72$fsec, respectively. In phase (4), C^{5+} and C^{6+} are mainly produced by the electron impact ionization while the field ionization saturates as $T_{(F)}^{(5)} = 0.096$ and $T_{(F)}^{(6)} = 0.079$ at $t \simeq 90$ fsec, respectively.

The distributions of the normalized electron density $n_e(y)/n_a$, where $n_e(y)$ is the elec-

tron density and n_a is the initial atomic density in the carbon film, and the electric field at six representative times in each phase are shown in Fig.3.4 (phase (1)), Fig.3.5 (phase (2)), Fig.3.7 (phase (3)), and Fig.3.9 (phase (4)), respectively. Here, the transverse electric field E_x is shown for phase (1) while the longitudinal one E_y for phases (2)-(4). The distribution of $n_e(y)/n_a$ shown in (a)-(e) are also illustrated in (f) for each phase. The phase space distributions of $(y, v_y/c)$ at different times are shown in Fig.3.6 for phase (2), in Fig.3.8 for phase (3), respectively.

Phase (1); The laser field which amplitude is smaller than that causing field ionization for C^{1+} can penetrate into the film as seen in Fig.3.4 since the carbon is assumed to be optically transparent in the present simulation. As the laser field increases to the ionization threshold, the field starts to ionize to C^{1+} and C^{2+} from the front part toward inside as seen in Fig.3.4 (a) which results from the field ionization. As the electron density exceeds that of the cut-off, the laser field is reflected at the critical density established near the surface. On the other hand, the laser field already penetrated inside the film causes ionization weakly. During this time ($t = 30 - 40$ fsec), ionization to C^{1+} and C^{2+} proceeds convectively leading to an ionization front as seen in Fig.3.4 (f) while they tend to stagnate at $t \simeq 40$ fsec corresponding to the saturation of C^{1+} and C^{2+} seen in Fig.3.3. As a result, a quasi-stationary staircase structure which corresponds to the charge state C^{1+} and C^{2+}, i.e. $n_e(y)/n_a = 1$ and $= 2$, is formed in $t = 40 - 50$ fsec. The velocity of the ionization front for C^{1+} and C^{2+} in phase (1) is estimated as $v_f/c \simeq 0.28$.

Phase (2); The ionizations to C^{1+} and C^{2+} are saturated around $t \simeq 40.0$ fsec as seen in Fig.3.4 while those for C^{3+} and C^{4+} gradual increase near the surface of the film as seen in Fig.3.5 (d). The propagation velocity of the front for C^{3+} is evaluated to $v_f/c \simeq 0.02$ from Fig.3.5(f). This corresponds to the time that the densities for C^{3+} and C^{4+} exhibit the gradual increases with time seen in Fig.3.2(b). Then, the transition takes place in the ionization dynamics at $t \simeq 56.4$ fsec, at which $\bar{N}_i^{(4)}$, i.e. the density $n_e(y)/n_a = 4$, increases rapidly. Namely, the ionization wave for C^{4+} is just triggered at this time and starts to propagate inside the film convectively keeping a sharp density front as seen in Fig.3.5 (e). Note here that a localized hump of longitudinal electric field E_y appears around the film surface as seen in Fig.3.5 (d) and (e), which also propagates with the front. Here, it is worthwhile to investigate the physical mechanism of the ionization trigger by relating with the electron dynamics in phase space. In Fig.3.6(I), we show the spatial distributions of longitudinal electrostatic force $f_{es} = -eE_y(t, y)$, ponderomotive force $f_p = -mc^2\partial\gamma/\partial y$, and total force acting on each electron $f_{tot} = f_{es} + f_p$ near the front, i.e. $-0.4 \leq y \leq 0.4\mu$m, where $\gamma = (1 + e^2E_x^2/m^2c^2\omega^2)^{1/2}$ in f_p is the relativistic factor estimated by the trans-

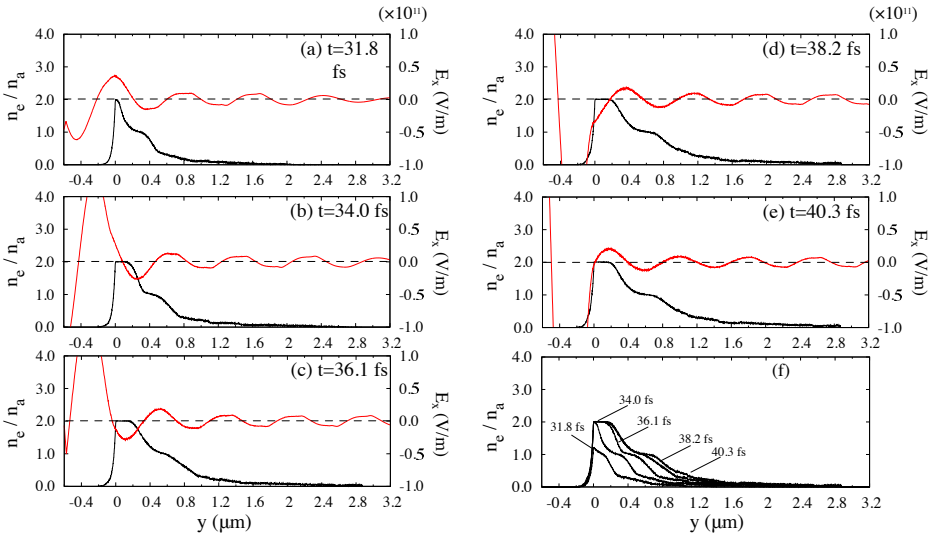

Fig3.4: In (a)-(e), spatial distributions of electron density (black) and electric field for transverse direction (red). In (f), the electron density profiles from (a) to (d) as ionization phase (1).

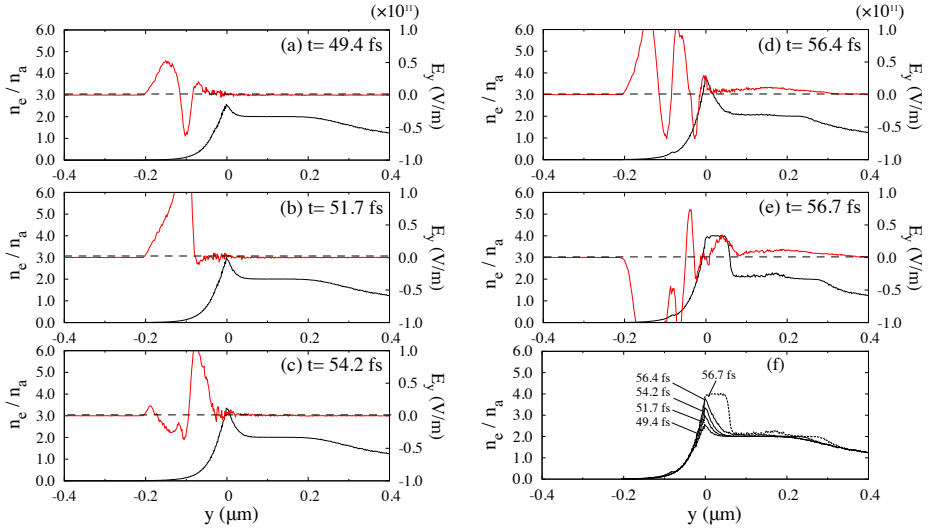

Fig3.5: In (a)-(e), spatial distributions of electron density (black) and electric field for longitudinal direction (red) near the front surface ($-0.4 \leq y \leq 0.4\mu$m). In (f), the solid lines are electron density profiles from (a) to (e) as ionization phase (2), and the dashed line is that at (d) as ionization phase (3).

verse electric field $E_x(t, y)$ observed in the simulation. In Fig.3.6(Ⅱ), we show the electron distributions in phase space (y, v_y) together with that of the electron density $n_e(y)/n_a$. These distributions are presented in every $\tau_l/4$ fsec ($\tau_l = 2.74$ fsec: laser period) from (a) to (f). Note that Fig.3.6 (c) and (f) corresponds to Fig.3.5 (c) and (d), respectively. An electron bunch is found to be extracted from the bulk plasma in the pedestal region indicated by an arrow in Fig.3.6 (a)(Ⅱ) due to the longitudinal electrostatic force E_y as seen in Fig.3.6(a). It is then accelerated to the negative direction approximately during the next time interval $\tau_l/4$. Note that the oscillating electrostatic field E_y results from the electrons pushed forward inside the film due to the oscillating laser ponderomotive force. Then, the electron bunch changes the direction and is accelerated to the positive direction due to the ponderomotive force during the next time interval $\tau_l/2$ as seen in Fig.3.6 (b) and (c), and reaches to the surface of the film. Thus, during the time interval τ_l, the electron bunch extracted from the bulk plasma is rotated in the clockwise direction, and then injected into the film. This process is repeated with the period $\tau_l/2$, i.e. the oscillating ponderomotive force leading to a train of electron bunches. The next bunch is also indicated by the arrow marked by (*) in Fig.3.6 (c)-(f), which is considered to trigger the ionization dynamics as seen in Fig.3.5 (d).

Phase(3); The electrostatic field E_y starts to propagate inside of the film accompanied by an ionization front leading to the plasma with the charge state C^{4+} as seen in Fig.3.7(a) and (b). Note that the amplitude of the electrostatic field located at the ionization front is $E_y = (0.2 - 0.4) \times 10^{10}$ V/m, which is a level in ionizing carbon atoms to C^{4+}. The ionization front is found to propagate convectively keeping a sharp density gradient as seen in Fig.3.7(f). Then, it can be seen that the longitudinal oscillating field E_y with the plasma frequency $\omega_p^{(4)}$ is excited near the surface of the film, i.e. $y = 0$, and propagate inside the plasma with C^{4+} as indicated by the arrow in Fig.3.7(b) and (c). This is found to be the wake field driven by the electron bunch which triggers the ionization front as discussed in the above. The propagation speed of the electron bunch is faster than that of the ionization front, so that the wake catches up the front. However, the wake is suffered from a damping during the propagation as seen in Fig.3.7(d) and (e), and the amplitude becomes weaker. Since the electron bunches are produced successively by the frequency $2\omega_L$ due to the ponderomotive force, the wakes are produced accordingly. Corresponding to the dynamics studied in Fig.3.7 (a)-(d), we also investigate the distribution of electron phase space and the electron density distribution as seen in Fig.3.8. Note that Fig.3.8 (a) ($t \simeq 56.7$ fsec) is just after Fig.3.6 (f) ($t \simeq 56.4$ fsec) while the distribution in wider spatial region, i.e. $-0.4 \leq y \leq 3.2\mu$m, is illustrated. In Fig.3.8, in order to study the

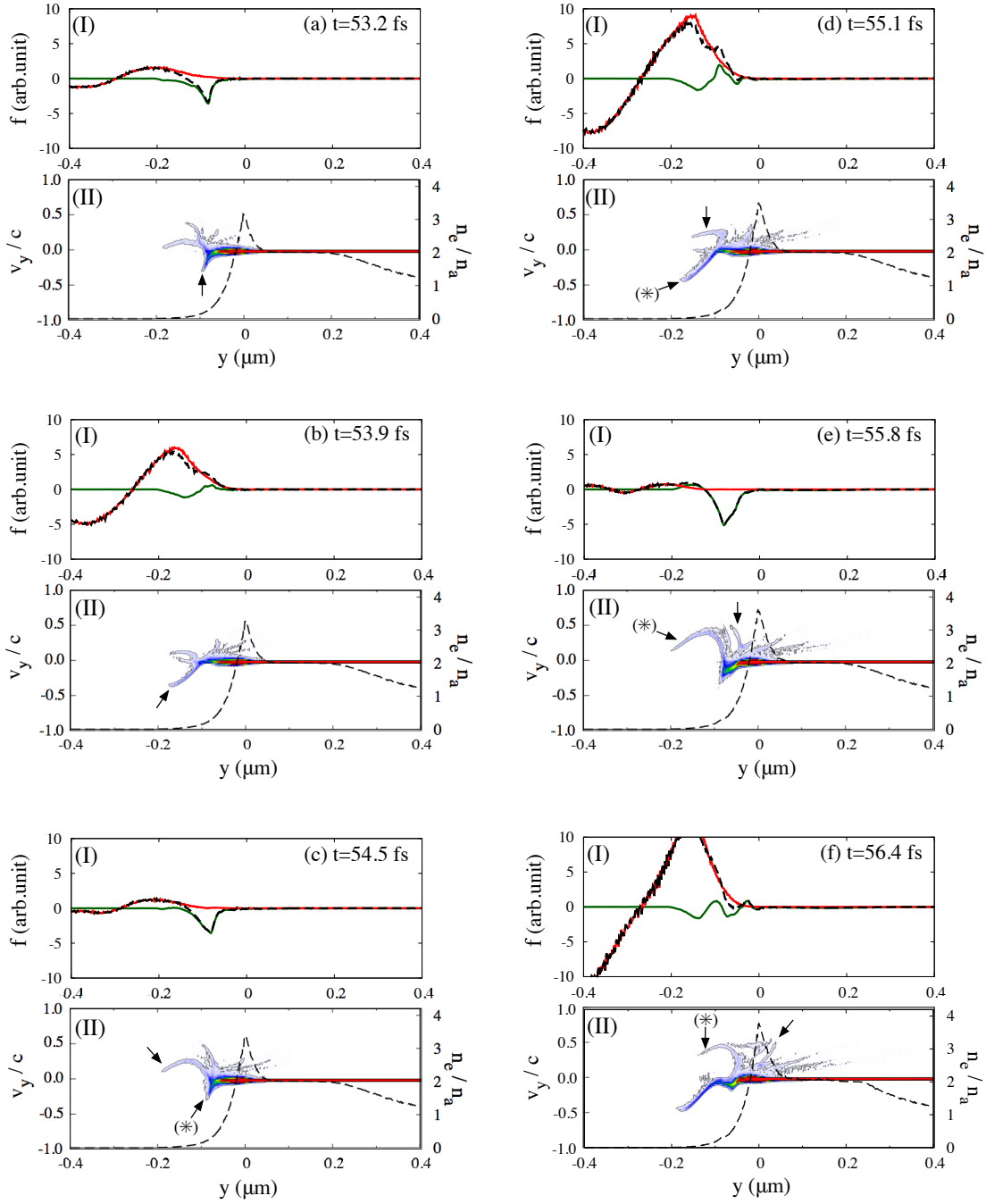

Fig3.6: (I) Spatial distributions of the pomderomotive force (red), electrostatic force (green), and total force (black) near the front surface ($-0.4 \leq y \leq 0.4\mu$m). (II) Phase space densities (y, v_y) of electrons and electron density profiles as dashed lines from 53.2 to 56.4 fsec. The electron bunches which drive the ionization front are marked by an arrow and (*) in phase space.

ionization dynamics, each electron bunch is indicated by a number. After the bunch (1) in Fig.3.8 (a) initiate the localized longitudinal electric field and triggers the propagation of the ionization front, it is then decelerated behind the front as seen in Fig.3.8 (b). This indicated that a part of the energy of the electron bunch is used to sustain the electric field. The next bunch (2), which has a larger energy than that of the bunch (1), catches up the ionization front and then decelerated. This process is repeated the propagation of the ionization front is sustained as seen in Fig.3.8(c) and (d).

Phase (4); the ionizations to C^{5+} and C^{6+} proceed from the front surface as seen in Fig.3.9, which illustrates n_e/n_a and E_y around the front region ($-0.4 \leq y \leq 1.2\mu$ m) in Fig.3.9 (a)-(e), and n_e/n_a at every 5.2 fsec from $t = 70.4$ fsec in Fig.3.9 (f). It can be seen that wake fields are excited near the front surface successively by the laser as discussed in Fig.3.7 and propagate inside the film with suffering from damping. As already discussed in Fig.3.3, the ionization is driven partially by the field ($\simeq 7\%$) but mainly by the electron impact. The evolution of ionization in the film can be seen in Fig.3.9 (f). It is found that the ionization front which scale length is the order of the thickness of the film, $1 - 2\mu$m, propagate slowly with the velocity $v_{f,q=5}/c = 0.2$ for C^{5+} and then whole the film tends to be a fully ionized plasma with C^{6+}.

In order to understand the ionization dynamics to C^{5+} and C^{6+}, we shows the phase space of electron together with n_e/n_a at six representative times as seen in Fig.3.10. One can see that an moderately high energy electron distribution which velocity ranges $0.05 \leq v_y/c \leq 0.40$ is produced at the interaction surface and propagates inside the film. The typical energy of the distribution, i.e. 0.50 keV $\leq$ E_e $\leq$ 46.5 keV, roughly corresponds to the energy that ionizes a carbon atom to C^{5+} and C^{6+} as seen in Fig.3.10 (b). Therefore, the propagation of the distribution coincides to that of the ionization front as seen in Fig.3.9 (f). In later time, electrons are recirculated by the sheath field at both surface which also contribute to the ionization to C^{5+} and C^{6+}. The electron velocity distribution $f(v_e/c)/N_{ion}$ integrated over the system are shown in Fig.3.10 corresponding to the representative times in Fig.3.10 (a)-(e). The electron distribution around v=0.9c is originated from the electron bunches which is accelerated by the laser ponderomotive force. After the laser ceases, the electron distribution around v=0.9c saturates and remains due to the recirculation between the both surface of the film. From $t = 73.0$ fsec to $t = 88.3$ fsec, the electron distribution with the velocity $v_e/c \geq 0.02$ ($E_e \geq 0.1$keV), which is bulk component of the film is accelerated to the high velocity region around $v_e/c = 0.1$ ($E_e = 5.1$keV). Namely, it can be seen that that the ionization to C^{5+} and C^{6+} and the bulk plasma heating is proceeded simultaneously. Two processes can be consid-

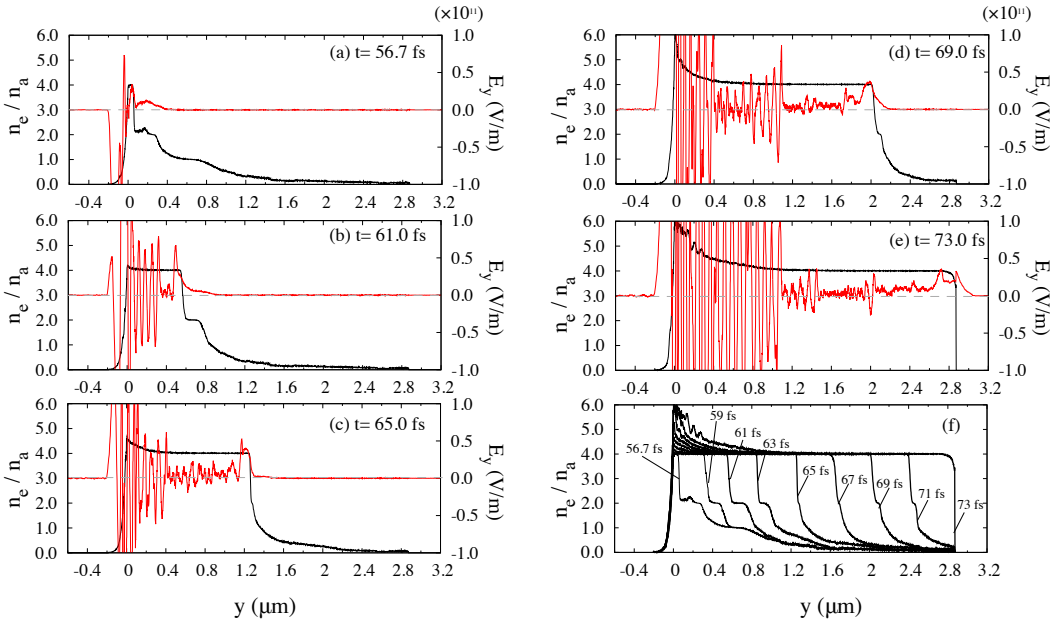

Fig3.7: In (a)-(e), spatial distributions of electron density (black) and electric field for longitudinal direction (red) in total simulation domain ($-0.6 \leq y \leq 3.2\mu$m). In (f), the electron density profiles every 1.9 fsec from 56.7 fsec as ionization phase (3).

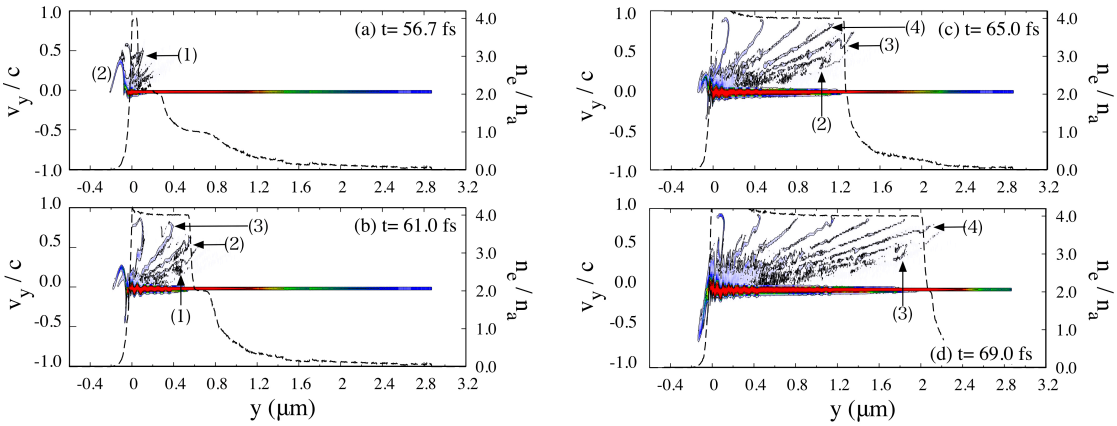

Fig3.8: Phase space densities (y, v_y) of electrons, and electron density profiles as dashed lines at same to Fig.3.7 (a)-(e). Each electron bunches are assigned with a number for explaining about the ionization front propagation.

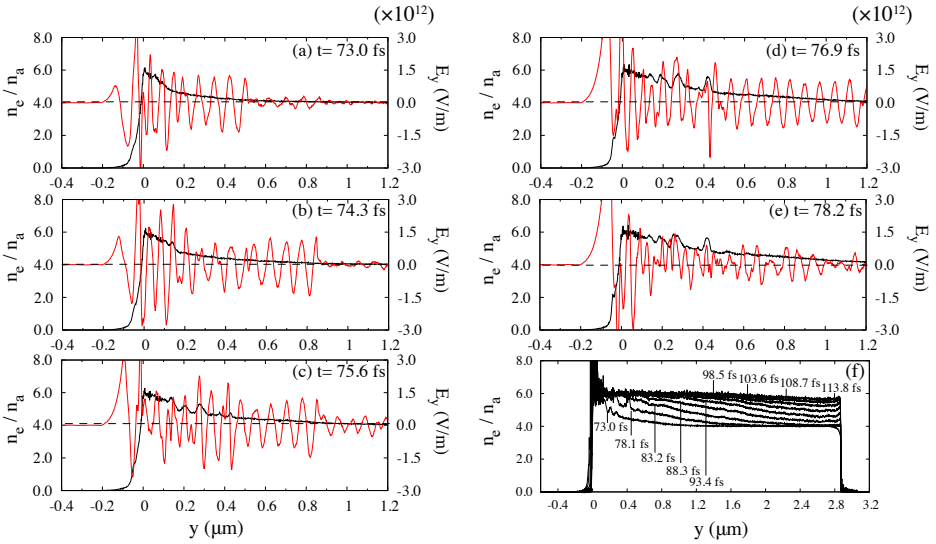

Fig3.9: In (a)-(e), spatial distributions of electron density (black) and electric field for longitudinal direction (red) in total simulation domain ($-0.6 \leq y \leq 3.2\mu$m). In (f), the electron density profiles from (a) to (e) as ionization phase (4).

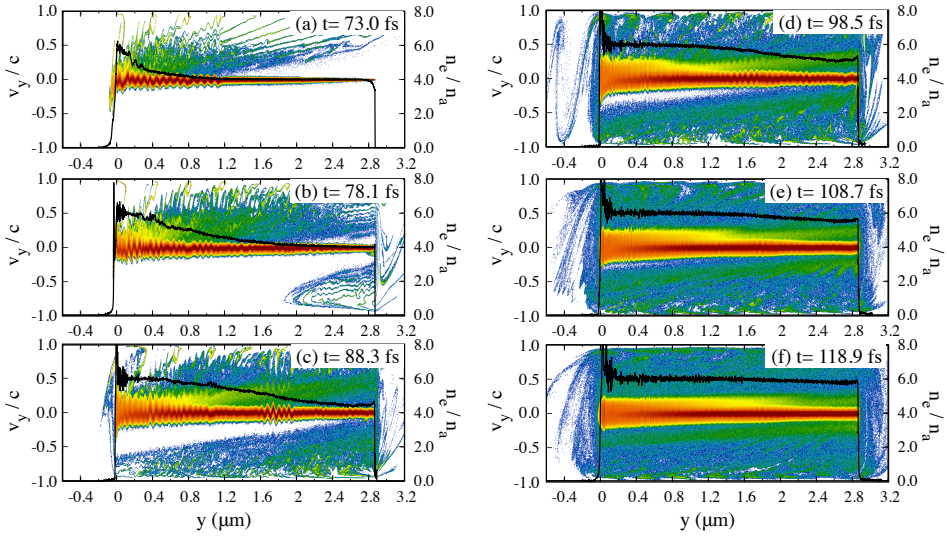

Fig3.10: Phase space densities (y, v_y) of electrons, and electron density profiles as solid lines.

ered as the candidate of heating. One is the thermal conduction by electrons heated near the surface, which belongs to those that ionize the plasma to C^{5+} and C^{6+}. The potential energy for C^{5+} and C^{6+} are $U_{q=5} \simeq 0.39$ keV and $U_{q=6} \simeq 0.49$ keV, respectively, so that the electrons which energy is larger than Up not only transfer heat but also ionize the plasma. The other is the heating by quivering electrons due to the wake fields. It is noted that more detailed study is necessary to know the ratio of the heating for each different mechanism quantitatively, which will be discussed in separated paper.

3. 3. 2 The case with field ionization loss

In order to clarify the effect of field ionization loss in the interaction, here we investigate the same ionization dynamics as discussed in Sec.Ⅳ A but including the effect described in Appendix A.

As seen in Fig.3.11 which illustrates the same time history of each ion abundance $\bar{N}_i^{(q)}$ as Fig.3.2, overall dynamics are similar besides those in phases (1) and (2). Namely, $\bar{N}_i^{(1)}$ and $\bar{N}_i^{(2)}$ in Fig.3.11 increase with slower rates than those in the case without field ionization loss in phase (1) as seen in Fig.3.2 while keep increasing even in phase (2). Around $t = 56.4$ fsec, i.e. the time at the end of phase (2). Both abundance, $\bar{N}_i^{(1)}$ and $\bar{N}_i^{(2)}$, reach to 0.05, which are approximately 1/5 of those observed in the case without field ionization loss. On the other hand, the ionization to C^{4+} corresponding to $\bar{N}_i^{(4)}$ exhibits similar dependence in Fig.3.2 in phase (2), that is, $\bar{N}_i^{(4)}$ changes the rate suddenly at $t = 56.4$ fsec in phase (3), suggesting that the ionization to C^{4+} is triggered accompanied by the rapid decreases of $\bar{N}_i^{(1)}$, $\bar{N}_i^{(2)}$, and $\bar{N}_i^{(3)}$. The rate is smaller than the case in Fig.3.2 slightly, so that the time that $\bar{N}_i^{(4)}$ reaches the maximum value is delayed to $t = 76.4$ fsec compared with that in Fig.3.2, $t = 72.0$ fsec.

Here, we discuss the difference between the cases with and w/o the field ionization loss in the spatial distributions of the electron density and electric field for the ionization phases (1), (2), and (3) as described in the following.

Phase (1); In the case without field ionization loss, the damping of the laser field penetrated into the film is originated from only the cut-off of the generated plasma. Additional to that, the field ionization loss also affects the damping of the laser field which ionizes the film in the first time scale of the laser. When the laser field starts to ionize the front of the film to C^{1+}, it is immediately damped to zero value since the local energy density of the laser field, $E_x^2/8\pi$, is smaller than that of the ionization, $n_i U_{q=1}$. After the generation of the plasma around the front surface, the ionization front with C^{1+} and C^{2+} proceed into

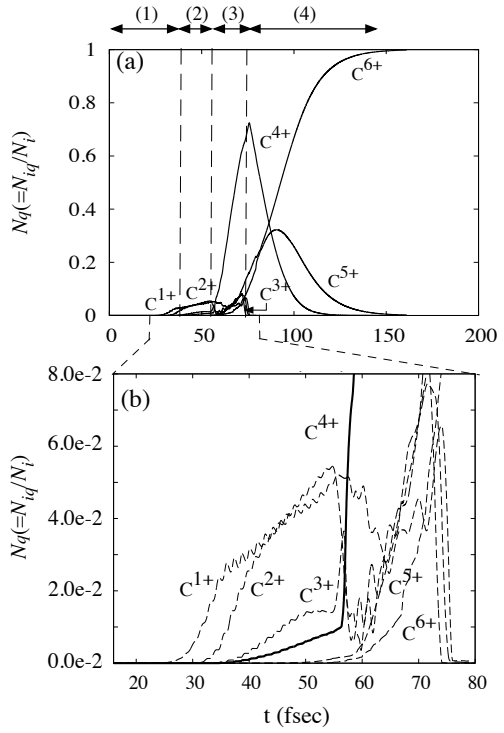

Fig 3.11: (a) Time history of ion abundance for each charge state C^{q+}. The dashed lines classify the time region for each ionization phase as different dynamics. (b) Expanded time history of that in the region of $20 \leq t \leq 80$ fsec as focused on rapid transition of ionization to C^4.

the film with the stepwise structure synchronized with the penetration and the oscillation of the irradiated laser field. Note that the field pattern, which propagates inside the film with the ionization front in Fig.3.4 (a)-(e), almost disappears in the case with the field ionization loss in Fig.3.12 (a)-(e). This difference with the result in Fig.3.4 (f) also can be seen in the structure of the electron density at representative times in Fig.3.12 (f), which is restricted in the narrower region than that without the loss due to the damping of the field. At the end of phase (1), the front positions of $n_e/n_a = 1$ and $n_e/n_a = 2$ relatively stagnate to $y_{(n_e/n_a=1)} = 0.16$ μm and $y_{(n_e/n_a=2)} = 0.08$ μm as seen in Fig.3.12 (e) compared with that, $y_{(n_e/n_a=1)} = 0.78$ μm and $y_{(n_e/n_a=2)} = 0.21$ μm as seen in Fig.3.4 (e).

Phase (2); The ionization to C^{1+} and C^{2+} keeps proceeding with the increasing of the laser field while those without the field ionization loss saturate as seen in Figs.3.5 (f) and 3.13 (f). In the same phase, the ionizations to C^{3+} and C^{4+} proceed in the front region due to both the field and the electron impact, which is also similar to that in the case without field ionization loss. The field ionization loss weakens the longitudinal electrostatic field E_y which satisfies the force balance with the laser pondero-motive force in the case without the field ionization loss as discussed in Fig.3.6. Thus, the some electrons accelerated to the high energy region can penetrates to the inside across the electric field E_y. These

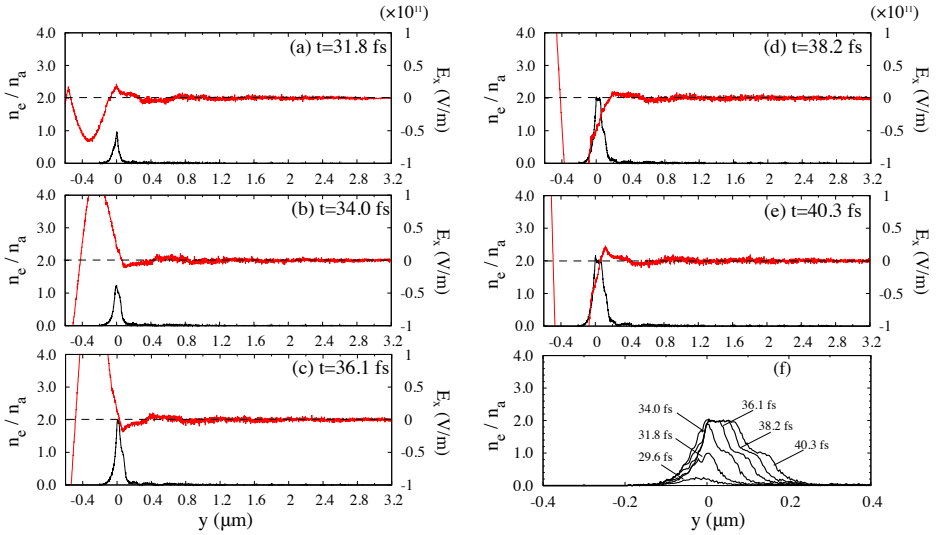

Fig3.12: In (a)-(e), spatial distributions of electron density (black) and electric field for transverse direction (red). In (f), the electron density profiles from (a) to (d) as ionization phase (1).

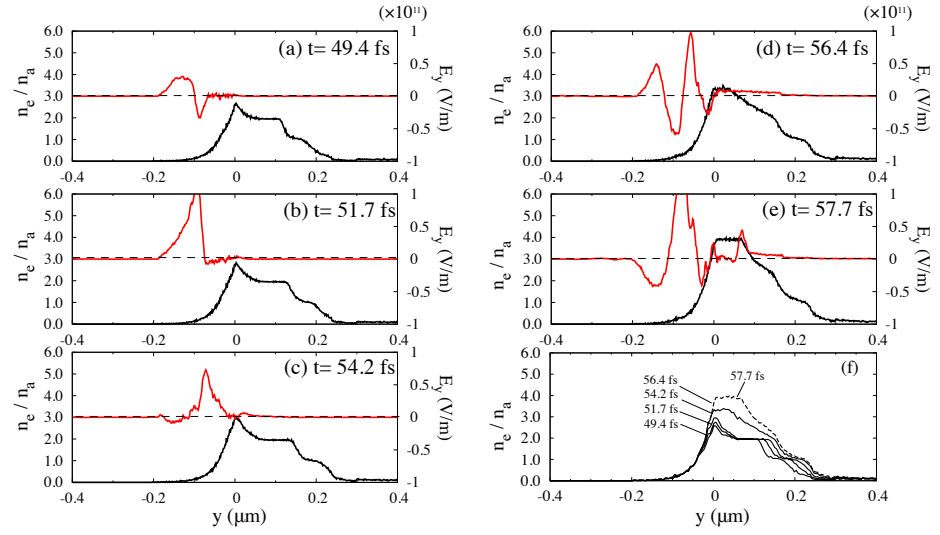

Fig3.13: In (a)-(e), spatial distributions of electron density (black) and electric field for transverse direction (red). In (f), the electron density profiles from (a) to (d) as ionization phase (1).

electrons excites the weak electrostatic field $E_y \simeq 10^{10}$ V/m in the inside of the film as seen in Fig.3.13 (e). It extends the density region with C^{3+} and C^{4+} to $y \simeq 0.15$ μm which is larger than that without the field ionization loss, $y \simeq 0.05$ μm. Although the dynamics and structure in phase (2) are slightly different compared with those in the case without field ionization loss, the transition that the ionization to C^{4+} starts to propagate convectively takes place at the almost same time, i.e. $t = 56.4$ fsec.

Phase (3); the ionization front of C^{4+} accompanied by the localized electrostatic field E_y propagates keeping sharp gradient with a staircase structure corresponding to C^{2+} as seen in Fig.3.7, while the gradient of the ionization front shows a relaxation gradually as it propagates inside the film in the case with field ionization loss as seen in Fig.3.14. This is due to that the localized electrostatic field near the ionization front is suffered from the damping for ionizing the plasma to C^{4+}. Namely, the high energy component of the electron bunches which successively injected into the film from the front surface goes through the potential barrier of E_y. These high energy electrons being ahead of the ionization front widens the electrostatic field, which also contribute in ionizing plasmas leading to the broadening of the ionization front. At $t = 71.8$ fsec, the electrons reaches to the rear surface of the film, which is clear from the generation of the sheath field while the front of $n_e/n_a = 4$ paths through $y = 2.1$ μm in Fig.3.14 (d). It is also noted that the front without the field ionization loss already reaches to the rear surface at this time, so that the propagation velocity in Fig.3.14 (f) become slightly slower due to the field ionization loss than that in Fig.3.7 (f).

The features of ionization dynamics to C^{5+} and C^{6+} is almost similar as those seen in Fig.3 since the electron impact ionization dominantly takes place in phase (4).

3. 3. 3 Comparing the ionization fronts without and with field ionization loss

The location of the ionization fronts in each cases of A and B with respect to time are investigated in Fig.3.15(a) and (b), respectively. Here, the both fronts of $n_e/n_a = 2$ and $n_e/n_a = 4$ are plotted as dashed and solid lines in this figure. Note that the front and rear surface of the film initially locate at $y = 0$ μm and $y = 2.87$ μm, respectively, so that the analysis of the front propagation is limited in this region. The front of $n_e/n_a = 2$ locates around $y = 0.18\mu$m, which is result from the ionization process in phase (2) until the ionization transition to C^{4+} ,i.e. $t = 56.4$ fsec. The front velocity of $n_e/n_a = 2$ is estimated as $v_f/c \simeq 0.45$ after the ionization trigger. It is accelerated from $t \simeq 63$ fsec

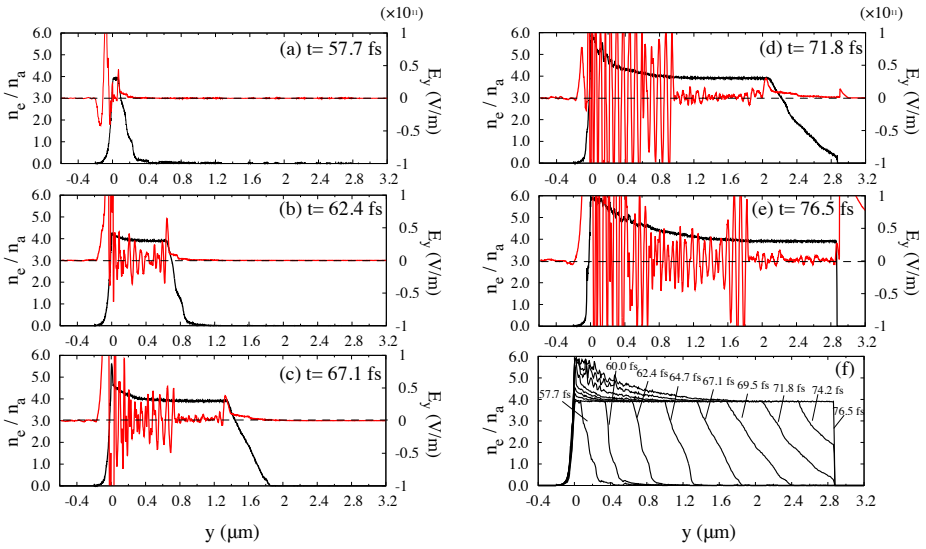

Fig3.14: In (a)-(e), spatial distributions of electron density (black) and electric field for longitudinal direction (red) in total simulation domain ($-0.6 \leq y \leq 3.2\mu$m). In (f), the electron density profiles every 1.9 fsec from 56.7 fsec as ionization phase (3).

to $v_f/c \simeq 0.68$, which is result from the increase of the irradiated laser intensity with gaussian peak at $t = 80.0$ fsec. The front of $n_e/n_a = 4$ also start to propagate at the same time, and the velocity is $v_f/c \simeq 0.57$ which is faster than that of $n_e/n_a = 2$. The front propagation of $n_e/n_a = 4$ catches up with that of $n_e/n_a = 2$ at $t \simeq 63$ fsec, and then the both front propagate to the rear surface with the same velocity. On the other hand, the velocities of $n_e/n_a = 2$ and $n_e/n_a = 4$ with the loss are estimated as $v_f/c \simeq 0.53$ and $v_f/c \simeq 0.48$ averaged in the whole propagation. Thus, the density gradient between $n_e/n_a = 2$ and 4 expands with the propagation. The each velocity is smaller than that in (a) which is shows that the energy of the electron bunches are more required for the front propagation in considering the field ionization loss to C^{4+}.

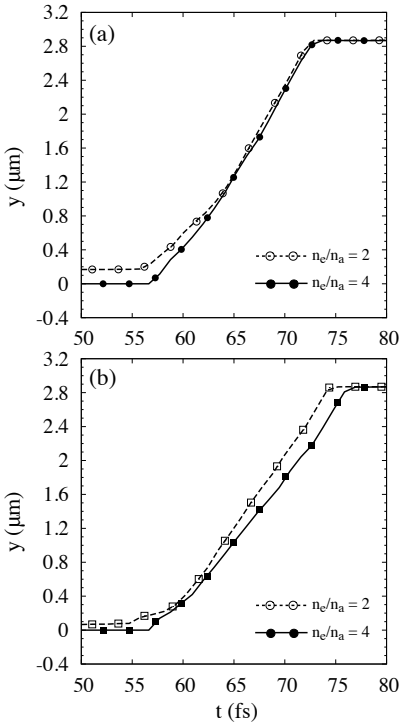

Fig3.15: Time history of the ionization front location of C^2 and C^4 in the time region of $50 \leq t \leq 80$ fsec. dashed line represents that of $n_e/n_a = 2$ and solid line represents that of $n_e/n_a = 4$ without field ionization loss (a) and with field ionization loss (b)

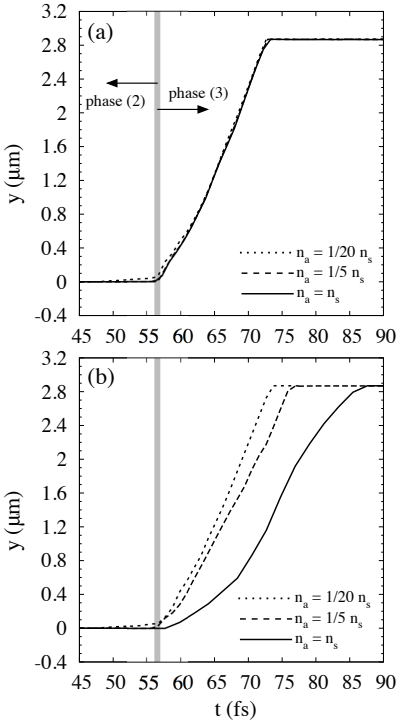

Fig3.16: Time history of the ionization front location of C^4 in the carbon density n_a =1/20n_s(dotted line), n_a =1/5n_s(dashed line), and n_a =n_s(solid line) without field ionization loss (a) and with field ionization loss (b), where n_a is the atomic density and n_s is the solid carbon density.

3. 4 The parameter dependence of the ionization propagation

In phase (3), the front propagation with C^{4+} is the dominant factor throughout the ionization in the film, so that this feature is worth to investigate in various condition. Here, we discuss about the parameter dependence of the film density and the laser intensity for the ionization dynamics in phase (3).

Figure 3.16 represents the propagation of the ionization front with C^4 in each atomic density which corresponds the 1/1, 1/5, 1/20 of the diamond carbon density n_s. Here we also investigate the effect of the field ionization loss compared between (a) the front propagation of C^4 without field ionization loss and (b) that with the loss. In Fig.3.16 (a), the ionization fronts of C^4 are just triggered at $t = 56.4$ fsec and also propagates with the same velocity in all density cases. It is due to that the electron acceleration is independent of the density of the film since the conditions at each location of the cut-off density in the pre-plasma are almost same. On the other hand, the fronts with the loss are also triggered at the same time of that without one in each density as seen in Fig17. However, the front velocity becomes slower than that in case A with the increasing of the density since the energy loss of the ionization wastes the field energy from solitary electrostatic field E_y around the front. They are averaged in whole region as $v_f/c \simeq 0.61$, $v_f/c \simeq 0.47$, and $v_f/c \simeq 0.32$ in each density $1/20n_s$, $1/5n_s$, and n_s, respectively. Eventually, the front velocity in the density n_s is attenuated with the propagation after the peak time of the laser intensity, i.e. $t = 80.0$ fsec. This result shows that the propagation of C^4 will saturate inside of the film with longer thickness.

Figure 3.17 shows the time history of the front of C^4 in each laser intensity ($a_0 = 0.5-5$). Note that we change the only peak laser intensity, so that these laser profiles are settled on the same pulse width and the same delay to peak amplitude. In the case of $a_0 = 5$, the front of C^4 is just triggered at $\tau_{tri} = 54.5$ fsec. The time of the transition to C^4 becomes late with decreasing of the peak laser intensity, and it delays to $\tau_{tri} = 71.2$ fsec in the case of $a_0 = 1$. These front are also accelerated during propagation inside the film due to the increase of the electron energy following the laser pulse, and the front velocity averaged in the whole thickness reaches to $v_f/c \simeq 0.62$ in $a_0 = 5$ and $v_f/c \simeq 0.51$ in $a_0 = 1$, respectively. On the other hand, in the case of $a_0 = 0.5$, the ionization to C^4 suddenly decrease, and the front saturates around the surface, i.e. $y = 0.15\mu$m. These difference of the ionization dynamics also appear in the energy distribution of the electron as seen in Fig.3.18. It shows the distributions normalized by the total ion number of the film at

each transition time τ_{tri} to phase (3) in the region of $a_0 \geq 1$ and that at the time of the laser peak intensity in $a_0 = 0.5$. In $a_0 \geq 1$, the electron energy reaches around 100 keV, and these electrons can propagate to the inside as the bunch with ionizing the carbon to C^4. However, in $a_0 = 0.5$, the generated election number totally decrease compared with the case in $a_0 \geq 1$, and the peak energy is less than 20 keV. Furthermore, in the relativistic region $a_0 \geq 1$, the laser amplitude observed at the surface of the film is within $a(\tau_{tri}) = 0.68 - 1.02$ at each transition time. This threshold is contributes to that the electron bunch is accelerated to the relativistic region and can propagate to the inside passing through the electrostatic field on the surface or not. Its amplitude keeps over the threshold during the front propagation in $a_0 \geq 1$, so that the field ionization becomes dominant. In $a_0 = 0.5$ which is less than the threshold value, the field ionization takes place only 8% for the whole carbon, so that the impact ionization changes the dominant component instead of that. Due to the threshold nature of the field ionization rate, the ionization is evolved in a stepwise manner synchronized with the laser frequency.

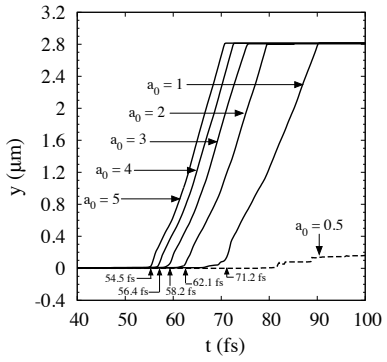

Fig3.17: Time history of the ionization front location of C^4 in each laser intensity ($a_0 = 0.5 - 5$). The solid lines show that on the laser peak intensity $a_0 \geq 1$, and dotted line shows that in the laser peak intensity $a_0 = 0.5$

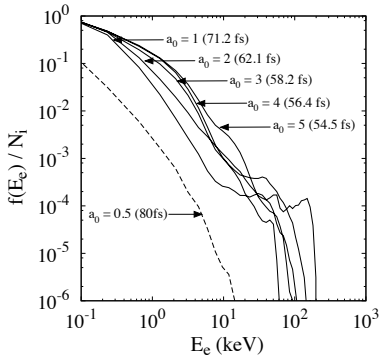

Fig3.18: The normalized electron distribution $f(E_e)/N_i$ with respect to the electron energy E_e, where the electron distribution $f(E_e)$ and total ion number N_i.

3. 5 Ionization dynamics of carbon film irradiated by circularly polarized laser pulse

Here, we investigate the ionization dynamics of the carbon film irradiated by the circularly polarized laser pulse. The simulation parameters are same for the above simulation so that the electrons are accelerated without the perturbation of the laser oscillation.

When the ionization dynamics transits to phase (3), the electrons are accelerated as beam near the front surface. We evaluate the potential balance of the electron which is result of the normalized fluid equation

$$\frac{d(\gamma\tilde{\boldsymbol{u}})}{d\tilde{t}} = -\tilde{\boldsymbol{E}} + \frac{\tilde{e}^2}{4\tilde{m_e}\tilde{\omega_L}^2}\tilde{\nabla}\tilde{\boldsymbol{E}}^2 + \frac{\tilde{\nabla}[\tilde{T_e}\tilde{n_e}]}{\tilde{n_e}}. \tag{3.5-1}$$

From the force terms of the right-hand side equation, the laser ponderomotive potential, electrostatic potential, and electron pressure are defined by

$$\tilde{\phi_p} = \int_0^{Ly} dx \frac{\tilde{e}^2}{4\tilde{m_e}\tilde{\omega_L}^2}\tilde{\nabla}\tilde{\boldsymbol{E}}^2 \tag{3.5-2}$$

$$\tilde{\phi_e} = \int_0^{Ly} dx(-\tilde{\boldsymbol{E}}) \tag{3.5-3}$$

$$\frac{\tilde{P_e}}{\tilde{n_e}} = \int_{l_x}^{Ly} dx \frac{\tilde{\nabla}[\tilde{T_e}\tilde{n_e}]}{\tilde{n_e}}, \tag{3.5-4}$$

where the pressure is calculated from the film surface with over $n_e(y) = n_i/10$ since high-velocity electrons emitted to the vacuum region are described by kinetic theory. Figure 3.19 shows the electron phase space for the laser propagation direction $y - v_{ey}$ and each potential near the front surface of the film. Before the electron acceleration takes place, the potentials of $\tilde{\phi_p}$ and $\tilde{\phi_e}$ are mostly balanced, and the electrons in pre-plasma are pushed into the inside of the film gradually. Then, the electron pressure gradual increases with increasing of the laser amplitude. From $t = 52.2$ fsec, the electrons located on the surface are emitted to the vacuum region by the pressure gradient, and they are pushed back by the laser ponderomotive force. In the linear polarized laser pulse, the ponderomotive force oscillates along $2\omega_L$ so that the accelerated electrons forms the bunch. However, in the circularly polarized laser pulse, the ponderomotive force keeps pushing the election to the

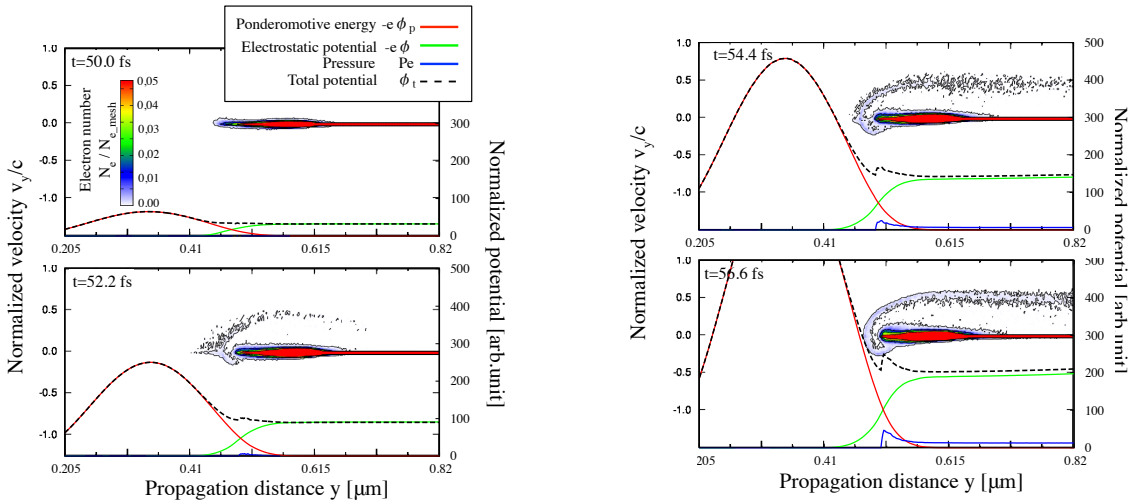

Fig3.19: Electron phase space for the laser propagation direction $y - v_{ey}$ and each potential $\tilde{\phi}_p$ (red line), $\tilde{\phi}_e$ (green line), $\tilde{P}_e$ (blue line) and near the front surface of the film

inside so that the accelerated electrons form the mono-energetic beam. In this condition, the fast ionization dynamics in the solid film is simplified compared with that in the case of the linear polarized laser.

Figure 3.20 shows the electron phase space for whole film region and the normalized ion charge density coupled with the electric field E_y. From $t = 59.6$ fsec which is the same time of phase (3) in the case with linear polarized, the ionization front C^{4+} is formed from $y = 1.23$ μm beyond the front region of the film. This is due to that the trapping of the accelerated electron with excitation of the electrostatic field E_y. After the trigger of the ionization to C^{4+}, the ionization front convectively propagates to the inside. The front velocity averagely reaches to $v_f/c \simeq 0.3$ which corresponds to the half value of the accelerated electron velocity. On the other hand, the ionization to C^{4+} near the front surface which isn't ionized by the electrostatic field with the high-velocity electron beam proceeds by electron impact with heat transfer after the propagation of the ionization front.

Here, we derive the self-stationary model for the front propagation of C^{4+} including the field ionization loss. First, the continuity equations of the electron and ion are given by

$$\frac{\partial n_i^q}{\partial t} = w_{fq}(n_i^{q-1} - n_i^q) \tag{3.5-5}$$

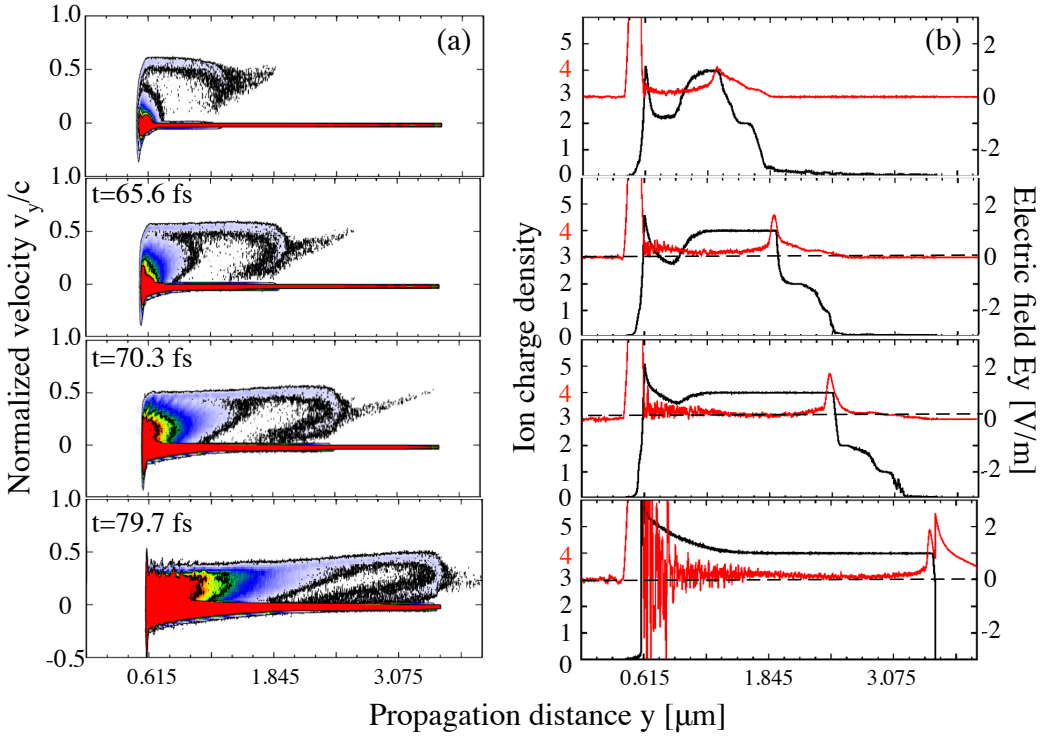

Fig3.20: Electron phase space for whole film region and the normalized ion charge density coupled with the electric field E_y

$$\frac{\partial n_e^q}{\partial t} + \frac{\partial}{\partial x}(n_e^q v_e) = w_{fq}(n_e^{q-1} - n_e^q), \tag{3.5-6}$$

where, w_f is cross-section of the field ionization, the ion velocity is approximated to $v_i = 0$. And, the approximation is assumed to satisfy $n_i^{(q-1)} \simeq n_e^{(q-1)}$. Therefore, the relation is given by

$$\frac{\partial n_e^q}{\partial t} + \frac{\partial}{\partial x}(n_e^q v_e) = \frac{\partial n_i^q}{\partial t}. \tag{3.5-7}$$

By using the relation between the moving frame $\xi = x + v_b t$ of the electron beam velocityv_b and the laboratory frame

$$\begin{aligned} \frac{\partial}{\partial x} &= \frac{\partial \xi}{\partial x}\frac{\partial}{\partial \xi} \\ &= \frac{\partial}{\partial \xi} \end{aligned}$$

$$\begin{aligned}\frac{\partial}{\partial t} &= \frac{\partial \xi}{\partial t}\frac{\partial}{\partial \xi} \\ &= -v_b\frac{\partial}{\partial \xi},\end{aligned}$$

the equation is rewritten as

$$-v_b\frac{\partial n_e^q}{\partial \xi} + \frac{\partial}{\partial \xi}(n_e^q - v_e) = v_b\frac{\partial n_i^q}{\partial \xi}$$

$$\left(1 - \frac{v_e}{v_b}\right)\frac{\partial n_e^q}{\partial \xi} = \frac{\partial n_i^q}{\partial \xi}. \tag{3.5-8}$$

On the other hand, equation of electron motion near the ionization front, i.e.,

$$m_e\frac{\partial v_e}{\partial t} = -eE - \nu m_e v_e.$$

From stationary solution is given by

$$v_e = \frac{-eE}{\nu m_e}, \tag{3.5-9}$$

where, ν is collisional frequency of the electrons, m_e is electron mass. From this formula, the difference of the electron density and the ion density is given by

$$n_i - n_e = -\frac{eE}{m_e\nu v_b - eE}(n_i^1 + n_i^1 ... + n_i^Z) \tag{3.5-10}$$

$$= -\frac{eE}{m_e\nu v_b - eE}\sum_{q=1}^{Z} n_i^q. \tag{3.5-11}$$

Here, we introduce the virtual current density to satisfy the energy conservation including the field ionization loss. The virtual current density is defined by assuming that the ionization loss is same to the energy loss of Ohmic heating as

$$-\boldsymbol{E}\cdot\boldsymbol{J}_{\mathbf{ioz}} = -\frac{\partial n_i^q}{\partial t}U^q. \tag{3.5-12}$$

Where the we consider one-dimensional model for the laser propagation direction as $\boldsymbol{E} \simeq E\boldsymbol{e_y}$, and the virtual current density is rewritten in the moving frame, i.e.,

$$J_{\mathrm{ioz}} = -\frac{ev_b}{E}\sum_{q=1}^{Z}\partial n_i^q \partial\xi U^q \tag{3.5-13}$$

From Maxwell-Ampere's low, the electric field in the moving frame is given by

$$\frac{\partial E}{\partial \xi} = 4\pi e(n_b - \frac{eE}{m_e\nu v_b - eE}\sum_{q=1}^{Z} n_i^q - \frac{1}{E}\sum_{q=1}^{Z}\frac{\partial n_i^q}{\partial t}U^q). \tag{3.5-14}$$

The stationary solution is calculated coupled with the density equation for each charge state, i.e.,

$$\begin{aligned}
\frac{\partial n_{i1}}{\partial \xi} &= \frac{w_{f1}}{v_b}(N_a - n_{i1}) \\
\frac{\partial n_{i2}}{\partial \xi} &= \frac{w_{f2}}{v_b}(n_{i1} - n_{i2}) \\
&\cdot \\
&\cdot \\
&\cdot \\
\frac{\partial n_{iz}}{\partial \xi} &= \frac{w_{fz}}{v_b}(n_{i(z-1)} - n_{iz}).
\end{aligned}$$

Here, we compare the simulation result by using the cross-section of the tunnel field ionization

$$W_q^{\mathrm{ADK}} = \quad \omega_A C^2 n, l\bar{U}\frac{(2l+1)(l+m)!}{2^m m!(l-m)!}\left(\frac{2\bar{E}_0}{\bar{E}}\right)^{2n^*-m-1}\exp\left(-\frac{2\bar{E}_0}{2\bar{E}}\right). \tag{3.5-15}$$

Figure 3.21 shows the normalized ion density of the simulation result and the stationary solution with- and without- field ionization loss. The model is calculated from the electron beam density and the velocity from the simulation result. The model with field ionization loss correctly describes the ionization profile of the simulation result compared with that w/o field ionization loss. It is due to that local energy of the electrostatic field near the ionization front mostly balanced to the ionization energy of C^{4+}. In the higher-Z film, the difference between each model becomes large not to be negligible for the ionization dynamics.

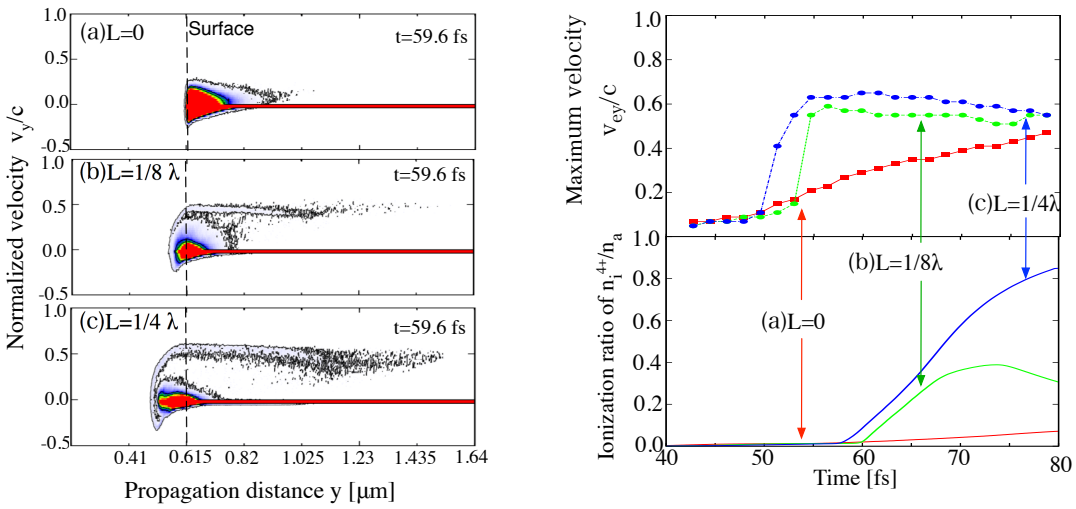

Fig3.21: normalized ion density of the simulation result (black line) and the stationary solution w/ (blue line) and w/o field ionization loss (red line)

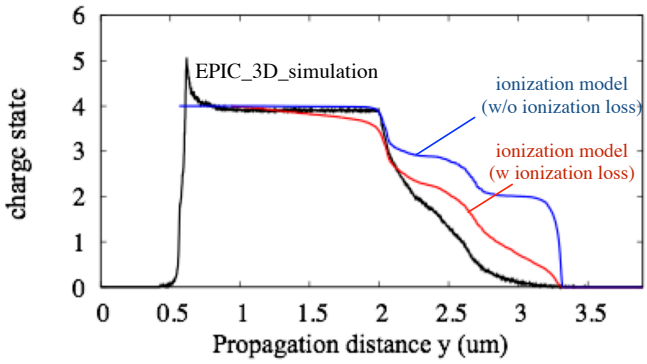

Fig 3.22: Electron phase space, peak election velocity, and ionization rate of C^{4+} in the case with the pre-plasma scale length $L_p = 0,\ 1/8\lambda,\ 1/4\lambda$

Figure 3.22 shows the electron phase space in the case with the pre-plasma scale length $L_p = 0,\ 1/8\lambda,\ 1/4\lambda$. From this result which is chosen at the ionization transition time of phase (3), it is found that the accelerated electron velocity becomes high with increasing the scale length. In the case without the pre-plasma, the electrons remain in the film region even if the increase of the electron pressure near the front surface of the film. Therefore, the electron impact ionization becomes dominant for the ionization to C^{4+}. However, a part of the electrons are emitted to the vacuum region due to the pre-plasma so that the electron beam injected into the film is generated. The electron velocity increases to $v_b = 0.6$ even in same laser intensity so that the ionization rate of C^{4+} also, depending on

the pre-plasma.

3. 6 Discussion and Conclusion

Ionization dynamics resulting from the interaction between a high power femto-second short pulse laser in the range of 10^{19-20} W/cm^2 and a carbon thin film in one-dimensional configuration was investigated using the particle-in cell code including atomic process and collisional relaxation process (EPIC). In this work, we found that the ionization of the film exhibits a multi-phase nature with different spatio-temporal structures due to the different ionization mechanism as summarized in the following. Specifically, the different charge state with different principal quantum number n, e.g. those for lower than or equal to C^{4+} and for higher than it, i.e. C^{5+} and C^{6+}, in the case of carbon film, shows different ionization dynamics qualitatively.

Phase (1): In the early phase that the laser amplitude is low as $I \simeq 10^{13-14}$ W/cm^2, the laser field penetrates into the film without causing ionization. Once the amplitude exceeds the value that ionizes carbon atom, the ionization to C^{1+} and C^{2+} starts from the front of the film to the inside. Once the electron density near the front surface exceeds the critical density, the laser field is reflected near the front so that further ionization does not take place. However, a part of the laser field penetrates to the inside of the film with the low ionization level due to the tunnel effect across the dense plasma with C^{1+} and C^{2+}. Due to this field, the ionization is evolved in a stepwise manner synchronized with the laser frequency while it is stagnated leading to a quasi-stationary staircase structure which corresponds to C^{1+} and C^{2+}. Here, it is noted that the ionization in this low laser power regime is sensitively influenced by the modeling for the field ionization loss since the relative ratio of the energy exhausted by the ionization to the laser becomes large. When the effect of field ionization loss is included, the penetration of laser field into the film is suppressed significantly. This suggests that the ionization dynamics in a low laser power regime has to be properly treated.

Phase 2: After the formation of the quasi-stationary staircase structure in phase 1, the ionization is further proceeded near the front surface to C^{4+} via electron impact ionization predominantly so that the electron density increases slowly leading to a density hump near the surface. When the electron bunch accelerated by the ponderomotive force injected from the front surface of the film, the field ionization up to C^{4+} is triggered abruptly, displaying a transition from a slowly evolving quasi-stationary mode to a fast

propagating mode.

Phase (3): After the trigger, the ionization front for C^{4+} exhibits a convective propagation keeping sharp ionization front. The localized longitudinal electrostatic field is found to be produced near the front and propagate with it, suggesting that the ionization is ascribed to the field. The velocity of the front is approximately $0.5 - 0.7c$ in the case without and with the field ionization loss, respectively. It is noted that that the front velocity is accelerated about 20% in later time that the laser field becomes larger. Then, the ionization front for C^{4+} reaches to the rear side, so that the whole film becomes a plasma with C^{4+}. The localized longitudinal electrostatic field by which the ionization takes place is sustained by the successive electron bunches induced by the laser ponderomotive force near the front surface. It is noted that the velocity of the electron bunch, which is $V_b \simeq c$, is faster than that of the ionization front, $V_f \simeq 0.7c$, so that the electron bunch overtakes the front and provides an energy to the electrostatic field. Then, the electron bunch is decelerated and the energy is decreased. This process is repeated by the electron bunches which are produced subsequently produced, so that the localized longitudinal electrostatic field and then the resultant ionization are sustained keeping the nearly constant propagation of the ionization front. This mechanism is found to be essentially similar to that discussed in ref[9],[10] while the electron dynamics emerged in the simulation is more complex. It is interesting to note that each electron bunch is found to excite quasi-coherent wake field which co-propagates with the bunch. The wake field is then suffered from the damping before the bunch overtakes the front, which causes the spread in the energy distribution and also the decrease in the average energy for the electron bunch. The velocity of fast propagation of the ionization front for C^{4+} is insensitive to the density of the film though it weakly depends on the model for the field ionization loss.

Phase (4): During the fast convective propagation of the ionization front for C^{4+}, the ionization to higher charge state, i.e. C^{5+} and C^{6+}, is proceeded exhibiting also a propagation via electron impact predominantly. It is noted that the gradient of the density is gentle, i.e. the same level as the width of the film, and the propagation velocity is estimated approximately $0.4c$, which is slower than that for C^{4+}. Namely, it can be seen that the propagation of the ionization for C^{5+} and C^{6+} is non-local in the sense that the wider range of the film is simultaneously ionized through the impact by high energy electrons which are bounded by the sheath potential at both boundaries and circulating. We found that part of the ionization to C^{5+} and C^{6+} near the front surface originates from the wake field which observed in phase 4, i.e. wake field driven ionization. It is excited by the successive electron bunches. The bunch density suddenly increase to a few % of the

solid electron density, i,e., $n_e \simeq 10^{23} cm^{-3}$ from the propagation front. Thus, it is enough to excite to high field level ionizing to C^{5+} and C^{6+}.

Here, we only studied the ionization dynamics in one dimensional simple configuration while it should be studied in 2 and/or 3 dimension where the longitudinal dynamics, specifically that for the trigger and/or transition for the ionization front, is coupled with transverse dynamics. We also investigated the ionization dynamics for a carbon film. It is interesting to study that for higher Z (heavier) material with more complex ionic state, where the fast propagation of ionization front not only for C^{4+} but also for higher charge state which make the ionization dynamics richer.

4 Ionization dynamics in high-Z solid target

4. 1 Introduction

The relatively lighter elements such as hydrogen, carbon, etc., which easily become the fully ionized state with the largest charge-to-mass ratio q/A as discussed in sec. III, and then are accelerated efficiently, have been widely used for laser-matter applications. In contrast to such lighter elements[64], heavier ones irradiated by the high power laser exhibit complex structure and dynamics dominated by plural physical processes such as ionization, recombination, and collisional relaxation processes, etc. These processes have to be taken into account in the analysis simultaneously and self-consistently.

The propagation of the ionization wave beyond the laser spot area in the solid medium has been experimentally observed as reported in Ref[52]. It was regarded that the ionization wave is originated from the electron transport to the laser transverse direction in the interaction with the high intensity laser field[65, 66, 67]. It has an important role to consider the initial condition for the energy transport inside the plasma and the acceleration of the multiply charged ions. However, the mechanism of the rapid ionization process has not been clarified in theoretical and simulation research. In this section, we investigated such ionization dynamics for the propagation- and transverse-direction in the laser interaction with the aluminum film.

4. 2 Simulation model for Al film

We carry out the 2-dimensional simulation for evaluating the ionization and ion acceleration by using EPIC3D (Extended Particle-based Integrated Code) which includes atomic processes such as a field ionization and an impact ionization. The field ionization is calculated as tunnel a field ionization process by calculating the electric field per particle based on ADK model[20], and the impact ionization is calculated by the cross-section through a binary collisional process between ion and electron based on BEB model[18]. The field energy loss can be estimated from the energy conservation with the ionization energy so that we introduce the ionization current calculated from the energy as Joule heating.

The simulation capability is set as $L_y = 14.4$ μm (18 λ) in the laser propagation direction (-y) and $L_x = 28.8$ μm (36 λ) in the transverse direction (-x), where λ (=0.8 μ m) is a wavelength of the laser field. In the simulation, the laser peak intensity is assumed to be $I = 1.0 \times 10^{21}$ W/cm^2 ($a_0 = 21$). The laser field is emitted with P-polarization from the left-hand boundary of the simulation domain during the Gaussian pulse duration τ =40 fsec and focused into 3-micron diameter to the solid surface. The solid film is based on an Al (Z=13) atom which is initially located in 3.2 μm $<$ y $<$ 4.0 μm with a thickness $l = 0.8$ μm (= λ) and distributed uniformly on the transverse direction. The mass density of the film is 0.675 g/cm3 which value is 1/4 for the real mass density of Al material, i.e., 2.7 g/cm^3. The initial charge state is set as Al^{1+} assumed the free electrons in the film, so that the initial electron density is $n_e/n_{cr} = 8.6$, where n_{cr} is the cut-off density, i.e., 1.74×10^{21}cm^{-3}. Therefore, the initial penetration length is $\sigma_{q=1} = 4.35 \times 10^{-2}$ μm, and that at the fully ionized plasma reaches to $\sigma_{q=13} = 1.21 \times 10^{-2}$ μm. In the simulation model, we investigate the ionization dynamics and ion acceleration of Al.

4. 3 Simulation results of the ionization of Al

Figure 4.1 represents the time history of field energy E_f, electron kinetic energy E_e, ion kinetic energy E_i summed up each charge state q (1-13), and total energy E_t (=E_f+E_e+E_i) in the simulation domain, respectively. The laser field is irradiated from the antenna, and then it applies the energy into the simulation domain and the plasma. From t=100 fsec, both energies of electron and ion start to increase due to the absorption from the laser field with approaching the time of the peak laser intensity (t=120 fsec). After the laser ceases, the electron energy saturates at t=135 fsec and then decrease gradually. A part of field energy remains in the simulation domain as the sheath field which generated by the charge separation between the high energy electrons and ion surface. Then, the ion energy keeps increasing due to the energy transfer from that of the electrons and the field to that of the ions, i.e., sheath ion acceleration.

In this process, we found the two kind of rapid ionization dynamics as seen in Figure 4.2. Fig. 4.2 shows the ion abundance q^+ for each charge state of Al in logarithmic scale. Here q^+ is determined as N^{q+}/N_{ion}, where N^{q+} is ion number for each charge state, and N_{ion} is total ion number. After the laser field hits the surface of the film, the ionization in M-shell electrons proceeds gradually from the initial charge state Al^{1+} until t=80 fsec. Then, the first rapid ionization starts to proceed for L-shell electrons, and the abundance of Al^{11+} which is the final state of the L-shell reaches to $N^{11+}/N_{ion} = 0.08$. The increase

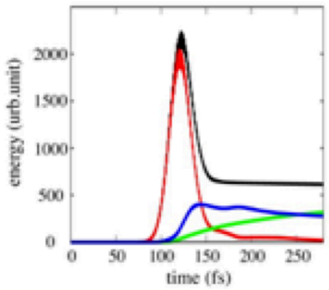

Figure 4.1. Time history of field (red), electron (blue), ion (gren), and total energy (black).

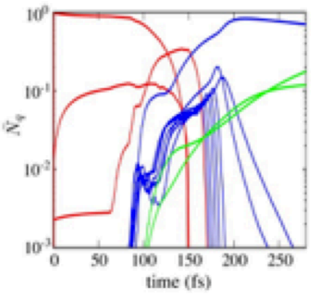

Figure 4.2. Time history of ion abundance of each charge state, where each lines are M-shell(red), L-shell(blue), and K-shell(green).

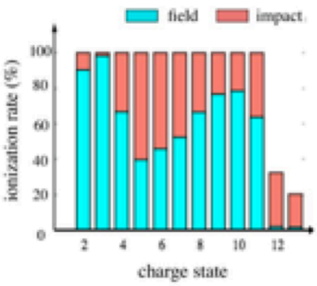

Figure 4.3. Ionization rate of the field(blue) and impact(red) for each charge state.

of the abundance with the L-shell electrons saturates from t=100 fsec, and the inner ionization to Al^{12+} and Al^{13+} starts to increase gradually. At t=115 fsec, the second rapid ionization takes place from the lower charge state, and the population of ions with charge state in M- and L-shell mostly transits to Al^{11+}, i.e., the ionization state is held in the final charge state of L-shell due to the ionization potential gap between L- and K- shell. The abundance of Al^{11+} reaches $N^{11+}/N_{ion} = 0.9$ at t=200 fsec and then decrease gradually while that of inner charge state: Al^{12+} and Al^{13+} keeps increasing with slower time scale than the other ionization process.

We also evaluate the difference between the field and the impact as seen in figure 4.3. Fig. 4.3 shows the ionization rate of the field and the impact component for each charge state until t=250 fsec when the laser has already ceased from the simulation domain. In the outer shell, i.e., M-shell, the field ionization takes place dominantly due to the laser field, and the rate reaches to 94.6 % which value is averaged from q=2 to q=3. The impact ionization proceeds only 5.6 %, i.e., the additional rate is 100. In L-shell, the field ionization rate decreases to averagely 40.4 %. Instead of that, the impact ionization rate increases due to the increase of the collisional frequency depended on the ionization degree, and the rate reaches to 59.6 % with slower time scale than that of the field. Finally, in inner-shell, i.e., K-shell, the impact components become dominant rate while that of the field is less than the 1 %, however the total ionization proceeds to only 25 % of the film. In this case, the ionization loss is estimated from the ionization degree, and the rate is only 0.1 % compared with the laser energy. Thus, the ionization loss is negligible for the investigating the dynamics.

Figure 4.4 represents (a) the normalized ion density ni/na in the region of $-3.2\ \mu$m $<$ y $<$ 3.2 μm and 2.8 μm $<$ y $<$ 4.4 μm at representative times, where ni is the ion charge

density, and na is the initial atom density, i.e., that shows the charge state as far as ions remain, and (b) the profile of ni/na and the electric field Ey at same times to (a). The ionization proceeds only around the front surface due to the cut-off of the laser until t=70 fsec. Then, the ionization front starts to propagate to the inside of the film with the electric field Ey as seen in Fig. 4.4 (a) and (b). This transition is driven by the propagation of the fast electron bunches generated by the $\boldsymbol{J} \times \boldsymbol{B}$ heating. The electron bunch is accelerated to the relativistic region at the front surface and injected to the inside of the film every twice of the laser frequency. The return current is also excited for the current neutralization with the bunch, and the solitary electric field at the front of the bunch and the plasma wave behind that are generated for propagation direction by the charge separation inside the film. Therefore, the field ionization to Al^{11+} takes places with the propagation of the electric fields Ey with the bunch as the first ionization dynamics. The ionization velocity is vf=0.8c which is almost same as the averagely bunch velocity. After the electrons reach to the rear surface, the sheath field is generated by the charge separation between the ion surface and the electron bunches. The electrons behind of that are reflected by the sheath field to the inside of the film and recirculate between the front and the rear surface with the initial scattering angle. So that, the electrons spread to the transverse direction over the laser spot area with the ionization to Al^{11+} as seen in Figure 4.5, which is the same as Fig. 4.4 (a) in the whole region. Around the laser spot area, the field ionization proceeds due to the electron bunches with the electric field as discussed in the above. However, the amplitude of the electric field gradual decreases due to the electron diffusion with the spread to the transverse direction, and the impact ionization rate changes larger than that of the field as second rapid ionization dynamics. Therefore, the velocity of the ionization to Al^{11+} for transverse direction is decelerated to averagely vf=0.6c compared with the first one. Additional to these rapid ionization processes, the ionization of Al^{12+} and Al^{13+} takes place due to the sheath field on the each surface and the collision around the laser spot area. Thus, the charge states of accelerated ion are decided more than Al^{11+} through these ionization processes and extracted from the film.

The highly charged ions are accelerated by the sheath field generated on both surfaces. The peak amplitude of the sheath field reaches to 35 TV/m which is same order to the laser peak amplitude so that the ionizations to Al^{12+} and Al^{13+} proceed due to the field ionization from the charge state of the bulk Al^{11+}. Then, the ions are accelerated and extracted to the vacuum region with the dependence of its charge to mass ratio as seen in Figure 4.6 which represents the ion energy distribution for each charge state. The ions of fully ionized state (Al^{13+}) with the largest charge to mass ratio is accelerated most effi-

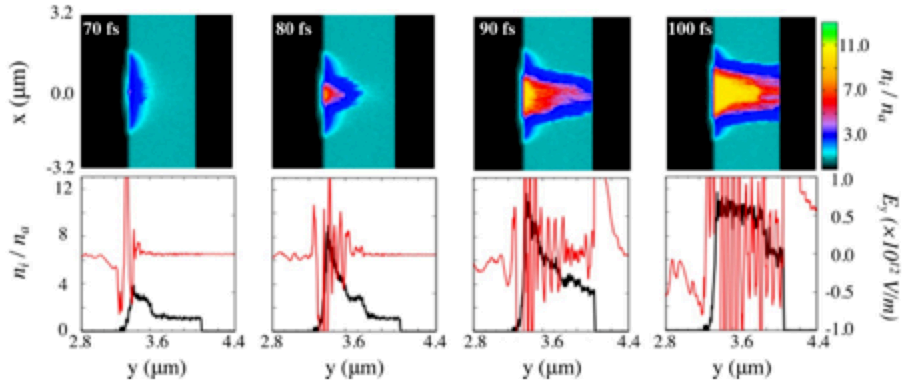

Figure 4.4. (a) Normalized ion density n_i/n_{a0}in 2-dimentional domain at representative times, where n_i is the ion charge density, and n_a is the initial atom density, and (b) the profile of n_i/n_a and the electric field Ey on x=0 at same times to (a)

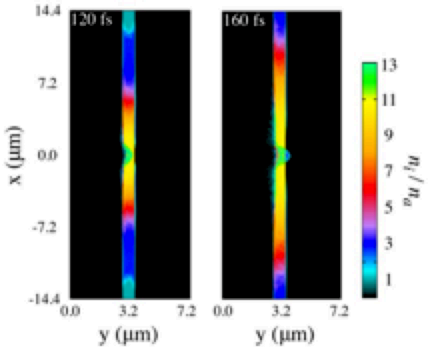

Figure 4.5. Normalized ion density n_i/n_a in 2-dimentional domain at t=120 fs and t=160

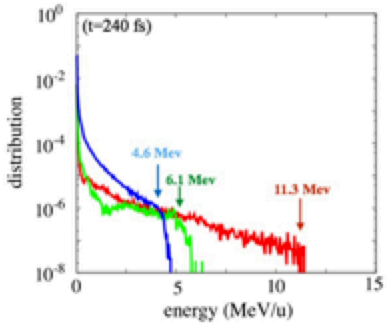

Figure 4.6. Ion energy distributions for the charge state q=11(blue). q=12(green), and q=13(red)

ciently in the Al, and then the maximum ion energy reaches to 11.3 MeV/u. On the other hand, the ion energy of Al^{11+} and Al^{12+} reaches to 4.6 MeV/u and 6.1 MeV/u which is less than the dependence of the charge to mass ratio compared with that of Al^{13+}. Therefore, the sheath amplitude for a lower charge state becomes smaller than that for Al^{13+} in the outside than the laser spot area.

In the interaction between such high intensity laser and the solid film of Al, the ionization dynamics with the field and the impact is mainly driven by the electron transport and decide the charge state of accelerated ions. Therefore, we will perform the simulation for higher-Z elements including the other atomic process such as recombination, radiation, etc.

4. 4 Conclusion

It is found that ionization wave propagates with the electron transport for laser transverse direction. Here, we investigated the ionization dynamics of an aluminum film in 2-dimensional. Around laser spot area, the field ionization to Al^{11+} which is the final state of L-shell proceeds with the electric field as discussed in the above. After the ionization to the propagation direction, the ionization wave of Al^{11+} also propagates to the laser transverse direction beyond the laser spot area. However, the amplitude of the electric field on the ionization front gradual decreases due to the electron diffusion with the spread to the transverse direction, and the impact ionization rate becomes larger than that of the field. Therefore, the velocity of the ionization wave with Al^{11+} is decelerated with the propagation to the transverse direction. Additional to these rapid ionization processes, Al^{12+} and Al^{13+} are ionized by the sheath field excited on both surfaces. They are extracted through the acceleration mechanisms which are discussed in next section.

5 Acceleration and ionization of gold ions

5. 1 Introduction

The study of proton acceleration[68, 69, 70, 71, 72] through a high intensity laser interaction with a solid film has been advanced for promising applications such as a proton cancer therapy[73, 74] and a fast ignition by proton beams[75, 76]. One of the most important features of such acceleration is that the accelerated protons reach to the order of sub ten MeV within a short time ($\simeq$ 1ps) and a small size ($\simeq 10\mu$m). In recent experiments, carbon (C)[77], aluminum (Al)[78], and iron (Fe)[79] with the full stripped state have been observed in the energy range of 10MeV/u. Their results indicate that the laser-driven ion accelerator becomes worthwhile to extend the schemes to heavy ion acceleration in which the highly charged ions are generated and accelerated. There is a possibility that such compact heavy ion accelerator explores a wider class of application primarily related to nuclear physics, e.g., highly charged heavy ion injector for nucleus-nucleus collision[80, 81] and nuclear transmutation[82, 83], extraction and acceleration of short-lived exotic nuclei[84, 85].

For both of the proton and the heavy ion accelerations, the generation of high energy electrons has the most important role to obtain the high energy ions[86, 87]. Especially, when the laser intensity of the wavelength λ is more than $I = 1.36\times10^{18}/\lambda(\mu\text{m})$ W/cm^2, in which the generated electrons are accelerated to relativistic region, the ion energy increase drastically through several acceleration mechanisms[88, 89]. Among their accelerations, the most typical acceleration mechanism to explain the experimental results is target normal sheath acceleration (TNSA)[90, 91, 92, 93]. In this mechanism, the electrons, which are accelerated by the laser field, excite the electric sheath field due to the charge separation with ion surface of the target. Then, it accelerates the ion to high energy regime. The theoretical models to solve the quasi-static electric potential of the sheath field have been proposed by assuming non-relativistic or relativistic Maxwellian distribution of the electrons. The proton acceleration energy in TNSA has been correctly described by the analytical solutions of such models.

On the other hand, the acceleration from the front surface interacted with the laser field directly is regarded to be a significant process for evaluating the ion energies, which is named as radiation pressure acceleration (RPA)[94, 95, 96]. In this mechanism, the laser

ponderomotive force pushes the electrons to the inside of the film. Then, the electrostatic field to the positive direction is formed as balancing to the ponderomotive force during the irradiation of the laser pulse, and it accelerates the ion. These ions penetrate into the bulk plasma as ballistic propagation, and it can be extracted from the rear surface of the film with a few micron thickness.

Most of them have been mainly studied for the proton acceleration so that they only consider the fully ionized state of the accelerated ions. In heavy ion acceleration, the mechanisms of not only maximum ion energy with the highest charge state but also ion energy distribution with lower charge states have to be investigated for those applications. Furthermore, the charge states of the accelerated ions aren't uniquely determined by the complex ionization dynamics. Thus, the numerical analysis of the heavy ion acceleration requires solving the ionization process coupled with the laser-plasma interaction.

5. 2 Simulation model including ionization process

We have carried out the simulation of the interaction between a gold film and a short pulse laser using the EPIC3D. The simulations were performed using the one-dimensional capability along y-direction with a computational domain of $-3.2\ \mu\text{m} \leq \text{y} \leq 16.8\ \mu\text{m}$, where $y = 0\ \mu$m is chosen to be the left-hand side (LHS) surface of the film as explained in the following. A gold film with a constant density n_1 is set at $y_1 \leq y \leq y_2$, where $y_1 = 0\ \mu$m and $y_2 = 0.8\ \mu$m, such that y_2 corresponds to the thickness of the film. A pedestal (pre-plasma) with a density that gradually increases from n_0 to n_1 as $n(y) = n_1\text{exp}(-(y_1 - y)/L_p)$ in $y_0 \leq y \leq y_1$ is assumed, where $L_p = 0.08$mum. Here, the density at the front, i.e. $n_0 = n(y_0) = pn_1$, is determined by $p = 10^{-3}$. The gold density is typically chosen to be $n_1 = 6.0 \times 10^{22}$ cm^{-3}, which is the real gold density.

A linearly polarized short pulse laser with electric and magnetic fields in the x- and z-directions, respectively, is irradiated along the y-direction from an antenna placed at $y = -3.1\ \mu$m near the LHS boundary. The laser wavelength is $\lambda_\ell = 0.8\ \mu$m and the corresponding cut-off density in the non-relativistic limit is given by $n_c = 1.74 \times 10^{21}$ cm^{-3}. The laser pulse width is chosen to be $\tau_\ell = 40$ fs (FWHM), with a Gaussian form $\text{exp}[-4(t - t_p)^2/\tau_\ell^2]$, where $t_p = 80$ fs which is the time when the laser intensity reaches a peak value. The maximum laser intensity is typically set to $I = 1.0 \times 10^{21}$ W/cm^2, which corresponds to $a_0(\equiv eA_0/mc^2) = 22.1$ in normalized units. The mesh number and width in the y-direction are $N_y = 4000$ and $\Delta y = 5.0 \times 10^{-3}\ \mu$m, respectively. The time step

Δt satisfies the Courant-Friedrichs-Lewy (CFL) condition as $c\Delta t/\Delta y/ = 0.1$.

5. 3 Simulation results of ionization and acceleration

Here, we present the simulation results of the ionization dynamics and the acceleration of the multiply charged ions in the laser interaction with the gold film.

Figure 5.1 (a) represents the temporal evolution of the field energy including the electrostatic and electro-magnetic components E_f, the electron kinetic energy E_e, and the ion kinetic energy E_i. And also, the energy losses of the field ionization U_f and the electron impact ionization U_{im} are represented in this figure, and the total energy is summed up with $E_t = (E_f + E_e + E_i) - (U_f + U_{im})$. The energies E_t and E_f increase along with the irradiation of the laser field. When the laser field reaches the surface of the film, the electron energy E_e starts to increase with the increase of the laser amplitude. The electron energy saturates at $t = 100$ fsec which corresponds to the laser peak time, and it starts to decrease gradually. After the irradiation of the laser field, the field energy remains with the certain level corresponding to the electric sheath field. Then, the ion energy keeps increasing due to the energy transfer from the electron energy through the field energy. At $t = 500$ fs, each energy saturates to the constant value, so that the generated plasma reaches to a steady state. From this result, the total absorption ratio can be estimated from the irradiated laser energy W_L as $R_t(t = 500) = E_t(t = 500)/W_L = 0.21$. Whereas the absorption of the plasma is over 20%, the energy losses of both ionization, i.e., U_f and U_{im} account for only 0.01% and 0.02% which is negligible for the main plasma dynamics. From these temporal evolutions, it also shows that the field ionization also saturates at $t = 90$fs which corresponds to the time that the laser reaches to the peak amplitude. The electron impact ionization keeps proceeding with the collisional relaxation process in longer time scale. The detail of the time transition of the ion population $\bar{N_{n,l}}$ which is categorized by the electron shell n and the orbit l is also shown in Fig.5.1 (b) in the same time scale of (a). Until the laser interaction starts, the charge state mostly remains as the initial condition $q = 1$ (6s). When the laser field hits the surface of the film, the ion also stated to be ionized to higher charge state suddenly, and then the charge state of all ions including the inside of the film reaches over the $q = 18$ (5s). During the laser interaction, a few ions are ionized to the charge state in $n = 3$, and it saturates to only $\bar{N_{3p}} = 6.0 \times 10^{-2}$ and $\bar{N_{3s}} = 1.2 \times 10^{-2}$ at $t = 100$ fs. After the irradiation of the laser field, the charge state dominantly transits more than that in 4f, and the ionization speed changes to slow down.

The ionization continues to proceed to the higher charge state intermixed with multiple states during the increasing of the ion energy in Fig.2 (b). The ion charge state mainly saturate to the state in 3d at $t = 500$ fs, while the abundance of the lower charge states in 4d, 4p, and 4s saturate to $\bar{N_{4d}} = 7.2 \times 10^{-2}$, $\bar{N_{4p}} = 3.3 \times 10^{-1}$, and $\bar{N_{4s}} = 3.8 \times 10^{-1}$, respectively. These distributions of the partially ionized state indicate the quality of the heavy ion acceleration, and each charge to mass corresponding the time transition of the ionization degree also contributes to the ion acceleration energy.

Figure 5.2 represents the ratio of the both components of the field tunnel ionization $\bar{N}_f^q = N_f^q/N_{ion}$ (a) and the electron impact ionization $\bar{N}_{im}^q = N_{im}^q/N_{ion}$ (b) at $t = 500$fs when the ionization saturates as seen in Fig.5.1 (b), where the $N_{f,im}^q$ are the ion abundance ionized by the field (f) and impact (im) for each charge state q. Here, the the ionization ratio is divided into four groups from the initial location of the film, i.e., (i) $0.0\mu\text{m} \leq \text{y} < 0.2\ \mu\text{m}$, (ii) $0.2\mu\text{m} \leq \text{y} < 0.4\ \mu\text{m}$, (iii) $0.4\mu\text{m} \leq \text{y} < 0.6\ \mu\text{m}$, (iv) $0.6\mu\text{m} \leq \text{y} < 0.8\ \mu\text{m}$. The ionizations of all ions to $q = 18$ (5s) are dominantly determined by the field component even in the inside of the film as seen in Fig.5.2 (a). It is due to the ionization wave co-propagating with the electrostatic field excited by the high energy electron bunches[97]. However, the field components are damped by the increasing of the electron density, and then the field ionization of the inside part (ii) and (iii) saturate to the $q = 30$ and $q = 29$ in 4f, respectively. The field ionization on the front surface (i) accounts for the higher charge state than the level of the inside since the laser field interacts directly. Its amount decreases as a staircase form along with the energy gaps of each ionization threshold and the ion with $q = 69$, which is the final state of $n = 3$, reach to $\bar{N}^{69+} = 3.0 \times 10^{-3}$. The field ionization on the rear surface (iv) also proceeds to the higher charge state $q = 67$ in $n = 3$. It is the result of the excitation of the sheath field on the rear surface. On the other hand, the impact ionization in each region shows the similar ratio in the range of $q = 18 - 54$ as seen in Fig.5.2 (b). The time scale of the electron impact is determined by the electron mean free path which corresponds to the bounded energy of each charge state. Thus, the electron impact ionization slowly proceeds to the charge state $q = 54$ in 3d after the field ionization takes place.

Figure 5.3 represents the ion phase space $y - P_y/mc$ and the spatial distributions of the ion charge density $y - qn_i$ which is also categorized in the initial location as (i), (ii)+(iii), and (iv) at the representative times. In phase space, the two kind of ion acceleration takes place from the front and the rear surface of the film. Around the front surface, the ions of (i) starts to be accelerated to the propagation direction $+y$ from $t = 106.7$ fs. This

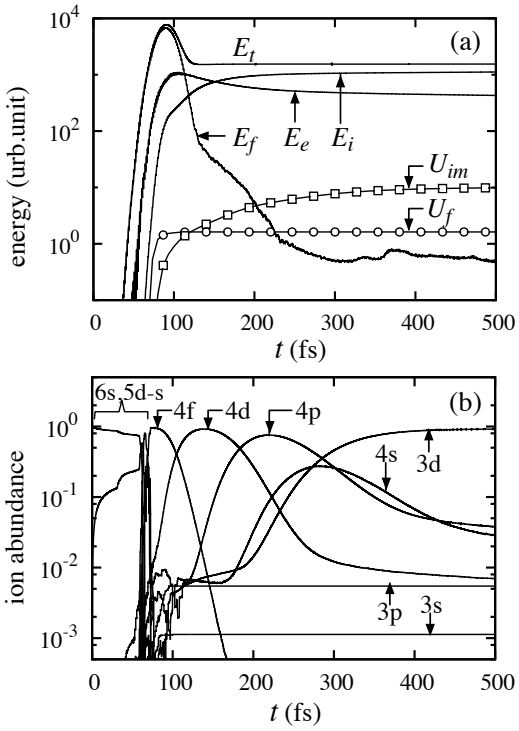

Fig5.1: (a) Solid lines show the temporal evolution of field E_f, electron energy E_e, ion energy E_i. Dot lines show that of field ionization loss U_f, electron impact ionization loss U_{im}. E_t represents total energy $E_t = (E_f + E_e + E_i) - (U_f + U_{im})$. (b) Time history of ion abundance for each electron orbit.

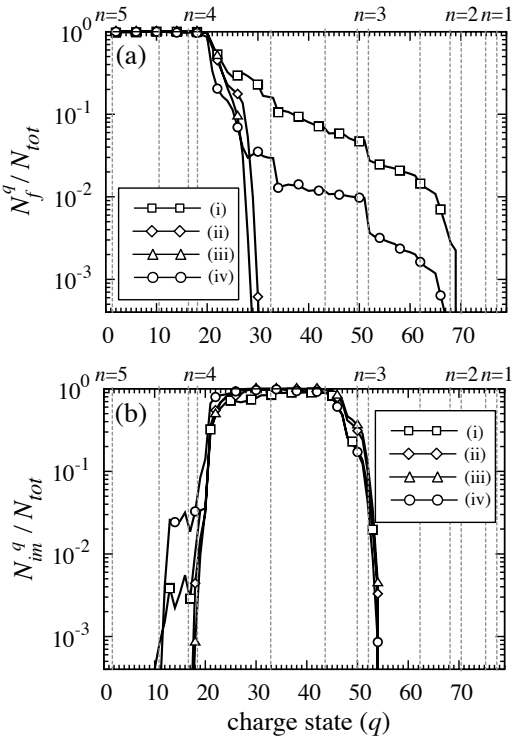

Fig5.2: Ionization ratio generated by (a) field and (b) electron impact at $t = 500$fs. Here, the ratios are divided into four groups from the initial location of the film, i.e., (i) $0.0\mu\text{m} \simeq \text{y} \simeq 0.2\mu\text{m}$, (ii) $0.2\mu\text{m} \simeq \text{y} \simeq 0.4\mu\text{m}$, (iii) $0.4\mu\text{m} \simeq \text{y} \simeq 0.6\mu\text{m}$, (iv) $0.6\mu\text{m} \simeq \text{y} \simeq 0.8\mu\text{m}$.

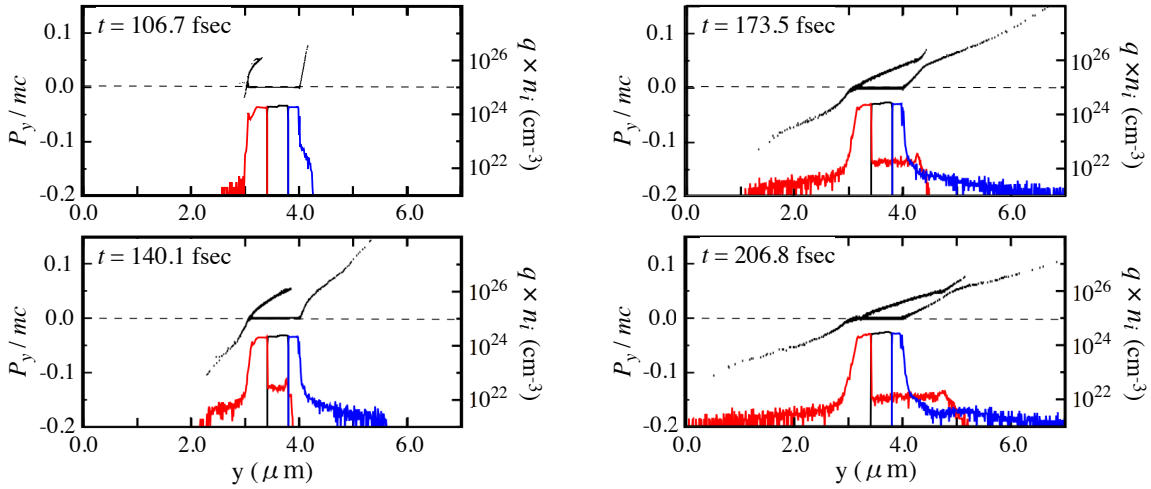

Fig5.3: Spatial distributions of ion phase space and ion charge density. The ion density is categorized by the initial location on (i), (ii)+(iii), and (iv) as illusrated to red line, black line, and blue line, respectively.

acceleration takes place in the front area, and then it reaches to $P_y/mc = 0.05$. Note that the ions are not only accelerated to $+y$ direction on the front surface but also it is expanded to $-y$ direction due to the sheath acceleration. These ions with the momentum $P_y \leq 0$ ballistically propagate to the inside of the film keeping the energy in the film region. When the ions are emitted from the film, the local density of the accelerated ions is larger than that of (iv). Thus, the secondary charge separation takes place on the ion front of (i) behind the expanded ion of (iv). This field re-accelerates the ion front of (i) with the changing the density form to exponentially decreasing. On the other hand, the ions around the rear surface are also accelerated to the vacuum area $+y$ through TNSA. The ions continue to be accelerated as long as the sheath field survives as seen in the Fig.5.1 (a). At $t = 206.8$ fsec, the peak momentum of (iv) increases to $P_y/mc = 0.15$ which is roughly 2 times the energy of that from (v).

In this interaction, such two kinds of acceleration mechanisms, i.e., (A) RPA as Hole boring regime and (B) TNSA, take place. In both mechanisms, it is founded that the field component accounts for the ionization to high charge state as discussed above, so that the detail of the ionization process and its distribution are shown for each region as follows.

5. 3. 1 RPA with ionization process

To discuss the only acceleration from the front surface, we show the ion distribution $n_i^{(n,l)}$ of (i)+(ii)+(iii) for each electron shell n and electron orbit l in logarithmic scale and the electric field for laser propagation direction E_y in linear scale as seen in Fig.5.4. The ions near the front surface are ionized along the field profile of E_x which forms the standing wave consisting of the incident and the reflected laser components. Thus, the highest charge state $q = 69$ in 3s is generated in the under-dense region of the pre-plasma. Then, the laser ponderomotive force pushes the generated electrons into the inside of the film with increasing of laser amplitude and excites the electrostatic field E_y as balancing to that. Although the charge to mass ratio of 3s is the highest value in the ion distribution, the peak amplitude of E_y locates around the distribution of 3d, which corresponds to the field ionization level on the reflecting surface of the laser field. It preferentially accelerates the ion with 3d into the inside of the film, and the ions with other charge stats also propagate following the ion front of 3d. When the ponderomotive force starts to decrease with the laser amplitude, the direction of E_y changes to $-y$ with losing the force balance as seen in Fig.5.4 (b). Therefore, the accelerated ions are separated from the ion distribution near the surface and propagate to the inside as the ion bunch in which the multiple charge states of $q = 32 - 69$ are intermixed. When the ions reach to the rear surface, only the front part of the ions with 3d and 3s is re-accelerated into the vacuum area co-propagating with the sheath field as seen in Fig.5.4 (c).

Figure 5.4 shows the ion energy distribution for each (n, l) at 240 fsec when the acceleration saturates. Note that the energy distribution is observed in the region of $y > 0$ for evaluating only the ion acceleration to $+y$ direction. The ion distribution is clearly separated to the low energy part of the bulk ions ($E_i \geq 2.0 \times 10^{-3}$ Mev/u) and the high energy part of the accelerated ions ($E_i \leq 1.0 \times 10^{-2}$ Mev/u). In the high energy part, the charged ions from $q = 32$ (4d) to $q = 69$ (3s) overlap in the region of $10^{-2} \leq E_i \leq 10^{0}$ MeV/u. The ion energy of $q = 67$ in 3d orbit reaches to the maximum value, i.e., 10.2 MeV/u which is slightly larger than that of $q = 69$ in 3s orbit.

5. 3. 2 TNSA with ionization processs

Figure 5.5 illustrates the spatial ion density for each (n, l) of (iv) and longitudinal electric field E_y in both logarithmic scale. When the laser amplitude reaches the peak value, the amplitude of the electric sheath field also reaches to $E_y = 1.0$ TV/m near the rear surface

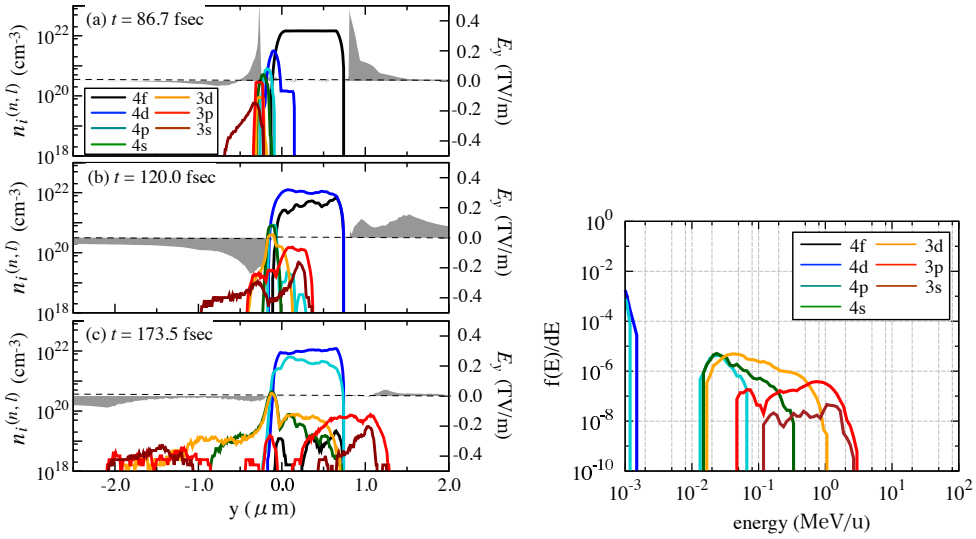

Fig5.4: Spatial ion distributions of (i)+(ii)+(iii) for each electron shell n in logaristic scale and the electric field for laser propagation direction E_y described as grey fill in linear scale, and the ion energy distribution of (i)+(ii)+(iii) for each electron orbit at 240fsec

of the film. It ionizes a part of the film to $q = 67$ in 3s and accelerates that to the vacuum area as the expansion front of the ion distribution. The location of the peak amplitude of E_y also propagate with the ion front so that it continues to be accelerated as long as the E_y becomes negligibly small. The ions with lower charge states are also generated behind the ion front, which follows to the Debye screening of E_y in the inside of the film. The spatial intervals between each ion distributions gradually extend with the ion propagation of the front, and the lower charge distributions are left behind of the sheath field. Thus, the acceleration time of the ion with the lower charge state becomes shorter than that of the expansion front with $q = 67$. On the other hand, the certain level of the electric field E_y, which is excited by the bulk electrons with cold temperature, i.e., $T_e \simeq$ keV, remains near the rear surface of the film. It continues to accelerate the ion keeping the charge states in $n = 4$. When the ion accelerated from the front surface of the film passes through the rear that, the sheath field also starts to propagate with it. Thus, the ions behind of the expanded front also re-accelerated along with the propagation of the ballistic ions of RPA. Figure 5.5 also shows the ion energy distribution for each state (n, l) of (iv) in logarithmic scale. The energy distribution of more than 4p orbit separated in each energy regions around $0.1 - 10$ Mev/u, while the total distribution continues to decrease exponentially from the low energy region as TNSA mechanism. In such distribution, the

energy of $q = 67$ which is the highest state in L-shell reaches to the peak ion energy, i.e., 22.2Mev/u which is roughly 2 times higher than that from the front surface. The distribution of 3d including the charge states $q = 63 - 67$ is ranged around $1 - 10$Mev/u which is much smaller than that of $q = 67$ even without the dependence of the charge to mass ratio.

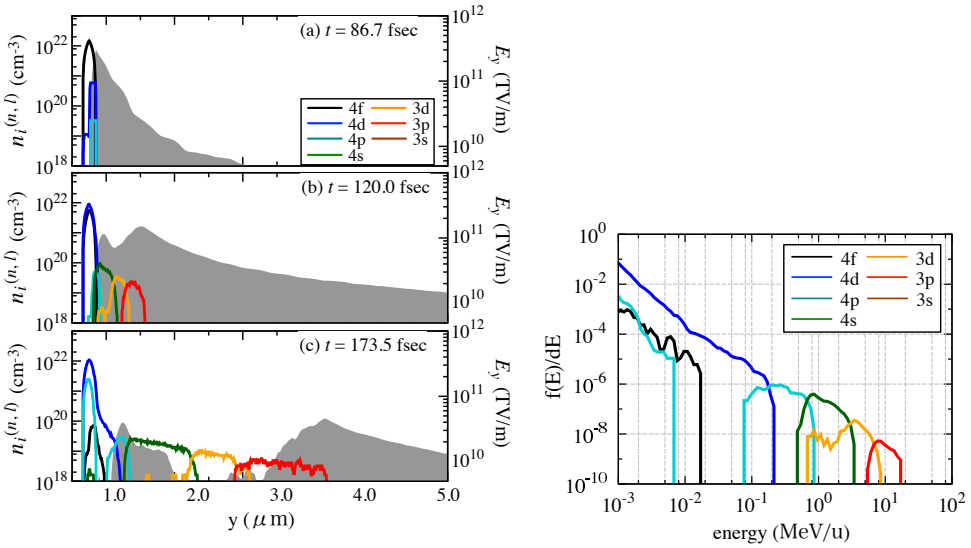

Fig5.5: Spatial ion distributions of (iv) for each electron orbit and longitudinal electric field E_y in both logarithmic scale, and the ion energy distribution of (iv) for each electron orbit at 240fsec

5. 4 Dependece of laser intensity for each ionization and acceleration

Even in the different laser intensity, the maximum ion energy from the rear surface $\epsilon_{i,\mathrm{rear}}$ of TNSA is larger than that from the front $\epsilon_{i,\mathrm{front}}$ of RPA. Figure 5.6 shows the dependence of the laser intensity for the maximum ion energies of TNSA and RPA, respectively, and the highest charge state in each acceleration. Here, the theoretical models, which have been respectively presented by Passoni[92] and Sentoku[94], are compared to the simulation result by assuming the highest charge state simulated in each mechanism. The front

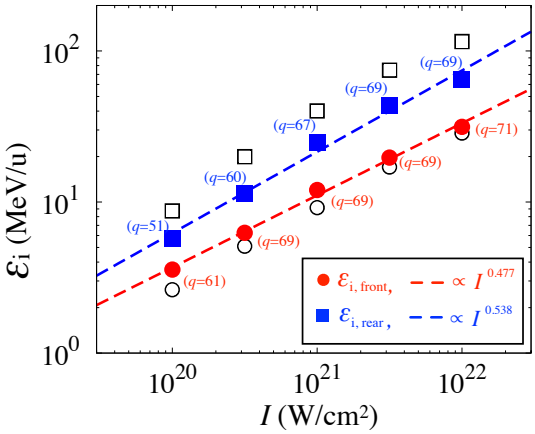

Fig 5.6: Dependence of the laser intensity for the maximum ion energies of TNSA (solid square) and RPA (solid circle), respectively, where the theoretical models which have been respectively presented by Passoni (holed square) and Sentoku (holed circle)

acceleration takes place after the laser field has ionized the ions to the highest charge state. Thus, if the parameter of the ion charge state is substituted for the theoretical scaling, it shows the mostly same dependence of the simulation results. However, the ion energy $\epsilon_{i,\mathrm{front}}$ of the simulation result is slightly larger than the energy scaling due to the re-acceleration coupled with the electric sheath field near the rear surface. On the other hand, the acceleration length in the acceleration from the rear surface is longer than that from the front surface, while the charge state is smaller than that. Therefore, the energy scaling of the maximum ion energy $\epsilon_{i,\mathrm{rear}}$, i.e., $I^{0.533}$ exceeds the scalingof $\epsilon_{i,\mathrm{front}}$, i.e., $I^{0.473}$. In comparing with the theoretical model assumed each highest charge state, the simulation result decreases to $60-80\%$ of this model due to the time transition of the charge state when the acceleration takes place.

5. 5 Effect of contamination layer for accelerated Au energy

The contamination layer of the water vapor (H^2O) is expected to be attached to the film surface, which has been investigated for the proton acceleration. On the front surface of the film, the contamination is peeled to outside region by the direct laser interaction so that it could be negligible for the ion acceleration from the front surface. However, the sheath field generated on the rear surface wastes to accelerate the contaminated ions, i.e., the proton (p) and oxygen (O), and the acceleration energy of Au decreases. In this case, the proton has the highest charge to mass ratio $Z/M)_{\mathrm{p}}$ even in the fully ionized state, i.e., $(Z/M)_{\mathrm{p}} \simeq 2.0(Z/M)_{\mathrm{O}} \simeq 2.5(Z/M)_{\mathrm{Au}}$. The contaminated ions also tend to be fully ionized state compared with Au due to the difference of the ionization potential, i.e.,

$U_{H^+}(= 13.6\ \text{eV}) \leq \text{U}_{\text{O}^{8+}}(= 87.4 \times 10^1\ \text{eV}) \leq \text{U}_{\text{Au}^{79+}}(= 93.2 \times 10^3\ \text{eV})$. Thus, both of the field ionization degree and the acceleration energy become smaller value through the energy transfer to p and O which are readily accelerated from the rear surface. Figure 5.7 shows the ion energy distribution from the front surface $\text{Au}_{(\text{front})}$ and the rear surface $\text{Au}_{(\text{rear})}$, and the distributions of p, and O which initially locate on the rear surface with the thickness of 10.0 nm (a) and 20.0 nm (b). IIn the case of (a) the contamination thickness 10.0 nm, the proton energy reaches to 31.0 MeV/u which is the highest value in the whole ions including O and Au. The most protons are also accelerated to over 20.0 MeV/u as the bunch, which keeps in front of the ion distribution included O and Au. On the other hand, the ion energy of O is less than that of p due to the difference of the charge to mass ratio discussed in above and reaches to 22.8 MeV/u with the fully ionized state. The maximum energy of $\text{Au}_{(\text{rear})}$ decreases to 5.6 MeV/u which roughly correspond to 1/4 for that in case of the pure gold film. Furthermore, the highest charge state of $\text{Au}_{(\text{rear})}$ also decreases to $q = 58$ from $q = 67$, which corresponds to the Debye screening of the electric sheath field behind of the contamination layer. The maximum energy from the front surface $\text{Au}_{(\text{front})}$ reaches to 10.6 MeV/u as same to the energy without the contamination. Even if the contamination thickness becomes larger to 20.0 nm, this energy distribution of $\text{Au}_{(\text{front})}$ is also same as seen in Fig.5.7 (b). However, $\text{Au}_{(\text{rear})}$ decrease to the half value of that in case (a), i.e., 2.7 MeV/u, which is in inverse proportion to the contamination thickness, and the maximum charge state of $\text{Au}_{(\text{rear})}$ decreases to $q = 51$. Thus, the ionization level and the acceleration energy of $\text{Au}_{(\text{rear})}$ also become less than that of $\text{Au}_{(\text{front})}$ in the case with the contamination.

5. 6 Scaling model of ion energy with each charge state in TNSA

While the ion front with the high charge state keeps being accelerated to the maximum energy in TNSA, the ions with lower charge state are generated and accelerated. To describe the peak ion energy for each charge state, we consider the simplified scaling based on the classical tunnel ionization formula;

$$I_{thr} = 1.0 \times 10^9 U_q^4 q^{-2}. \tag{5.6-1}$$

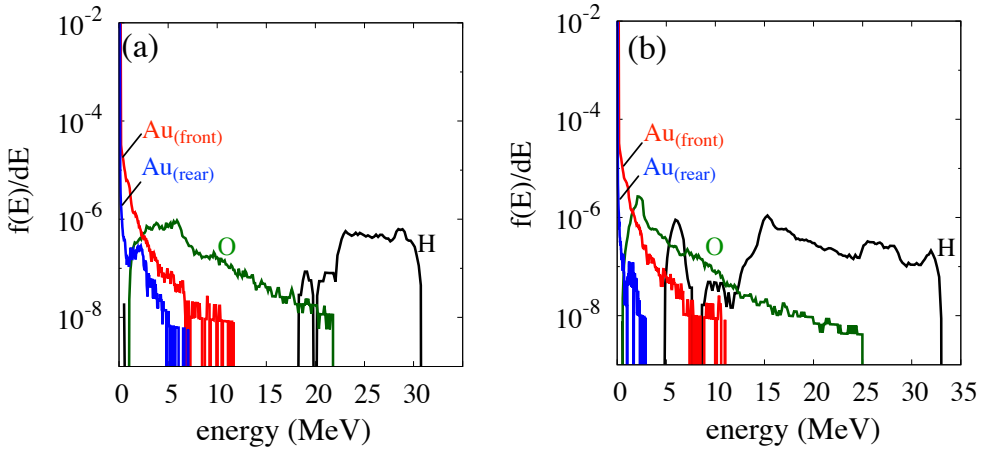

Fig5.7: Ion energy distribution of Au from the front surface $Au_{(front)}$ and the rear surface $Au_{(rear)}$, and the distributions of p, and O which initially locate on the rear surface with the thickness of (a) 10.0 nm and (b) 20.0nm

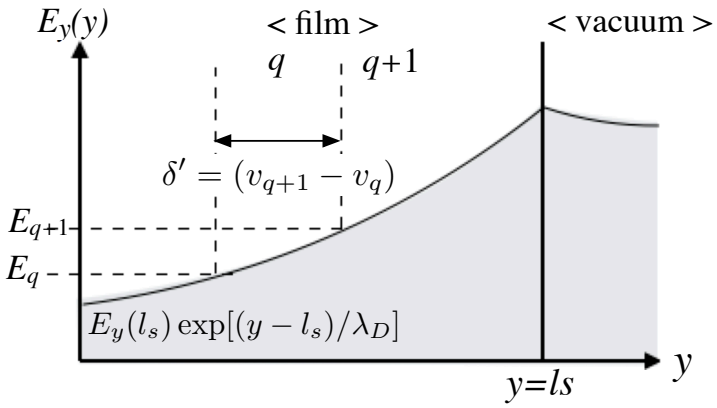

Fig5.8: Schematic representation of Debye screening of sheath field and charge distributions around rear surface of the film.

This formula also indicate the upper limit of the accelerating electric field for the ion with q, i.e., $E_{\mathrm{lim,q}} < E_{q+1}$. Around the rear surface, the spatial charge distribution inside of the film is followed by the Debye screening of the sheath field as $E_y = E_p \mathrm{e}^{-(\mathrm{y}-\mathrm{l_s})/\lambda_\mathrm{D}}$ as seen in Fig.5.8, where the E_p is the peak amplitude of the sheath electric field on the rear surface, and $\lambda_D (= \sqrt{T_e/(e^2 n_e)})$ is Debye length inside of the film. Here, the cross-section of the multi-filed ionization to the maximum charge state generated by the sheath field is less than the total ion amount localized at the rear surface. Thus, the Debye length λ_D for each charged ion acceleration is approximated to a constant value determined by the averaged electron temperature and the averaged charge density. In this field profile, the ion velocity $v_q(t)$ is calculated from the equation of motion described by

$$v_q(t) = \frac{q}{M_i} \int_0^{\tau_q} \mathrm{dtE_y(y)}. \tag{5.6-2}$$

The ions are accelerated from the rear surface in order of the higher charge state, and then the acceleration time τ_q for each charge state is given by the relative velocity difference between the q and $q+1$, i.e.,

$$(v_{q+1}(t) - v_q(t))\tau_q = \lambda_D. \tag{5.6-3}$$

To estimate the peak ion energy, the spatial location of q is assumed to be near that of $q+1$, so that the electric field for q and $q+1$ is assumed to be smae value. Thus, the acceleration length for the peak ion energy of q is approximated to

$$v_q(t)\tau_q = \frac{v_q(t)}{v_{q+1}(t) - v_q(t)} \lambda_D \simeq q\lambda_D. \tag{5.6-4}$$

Here, the acceleration length is much smaller than the scale length of the expnaded ions so that the electric field which acclerates the ion with q is approximated to be a constant value as $E_{q,max} = E_{q+1}/2$ during the time of τ_q Then, the peak ion energy of q is given by

$$E^q_{i,max} = \frac{q}{M_i} \int_0^{v_q \tau_q} E_y(y) \simeq \frac{1}{2} q^2 \lambda_D E_{q+1}. \tag{5.6-5}$$

It shows that the peak ion energy with each charge state assuming the field ionization is dominant.

This scaling correctly describes the simulation result of the peak ion energies for each charge state. Figure. 5.9 shows the simulation result of the ion peak energies in the laser intensity $I = 10^{20}, 10^{21}, 10^{22}$ W/cm^2 and the scaling fomula (5). Here, the charge

dependence of the ion energy is compared in the case w/o the contamination (a) and with 10nm contamination thickness (b). Note that the Debye length of this model is calculated from the simulation result of the averaged temperature and the averaged charge density in the case of $I = 10^{21}$ W/cm^2. In the case (a), the maximum ion energy and the charge state increase with increasing of the laser intensity, which detail is more discussed in Sec. V. The ion front is predominately accelerated to the higher energy above the scaling formula of (5). It is due to that the front keeps being accelerated with the propagation of the sheath field beyond the acceleration length assumed in formula (3). Behind of the ion front, the ions with the lower charge state are also accelerated according to the upper limit of each ionization potential as the relation of (5). Even in the different laser intensity, the peak ion energy for lower charge state can be explained by this formula as seen in Fig.5.9 (a). It also indicates that the increase of the laser intensity is less important of the acceleration length $q\lambda_D$ since both of the electron temperature and the averaged charge state increase. In the case (b), this scaling explains the charge dependence of the peak ion energy including the ion front of Au as seen in Fig.5.9 (b). It results from that the proton and oxygen are accelerated ahead of Au by the sheath field. Especially, in the laser intensity $I = 10^{20}$ W/cm^2, the ion energy becomes to be less than the scaling model of (5) in the consequence that the ionization type of the accelerated ions charges to the electron impact. Therefore, the peak ion energies in the lower laser intensity deviate the scaling which assumes that the field ionization dominantly takes place.

5. 7 Collisional effect and three body recombination

To investigate the collisional effect for the ion acceleration, the spatial distributions of the ion density ionized by the field and the electron impact, and the averaged ion energy $< E_i(y) >$ are shown in Fig. 5.10. The time of their results are chosen at $t = 500$ fsec when the ion acceleration and the ionization process mostly saturate in the both cases of $I_l = 1.0 \times 10^{20}$ W/cm^2 (a) and $I_l = 1.0 \times 10^{21}$ W/cm^2 (b). Note that each density is separated by the ionization components for only the outer state, which is unrelated to the previous ionization process of the ion. In the case (a), the ions ionized by the electron impact ranges to $y = 2.0$ μm which is behind of that ionized by the field. The averaged ion energy of the electron impact component reaches to only $< E_i > \simeq 5.8 \times 10^{-2}$ MeV/u, while the maximum ion energy reaches to $E_i \simeq 4.0$ MeV/u. On the other hand, in the case (b), the region of the electron impact component extends to $y = 3.5$ μm and the

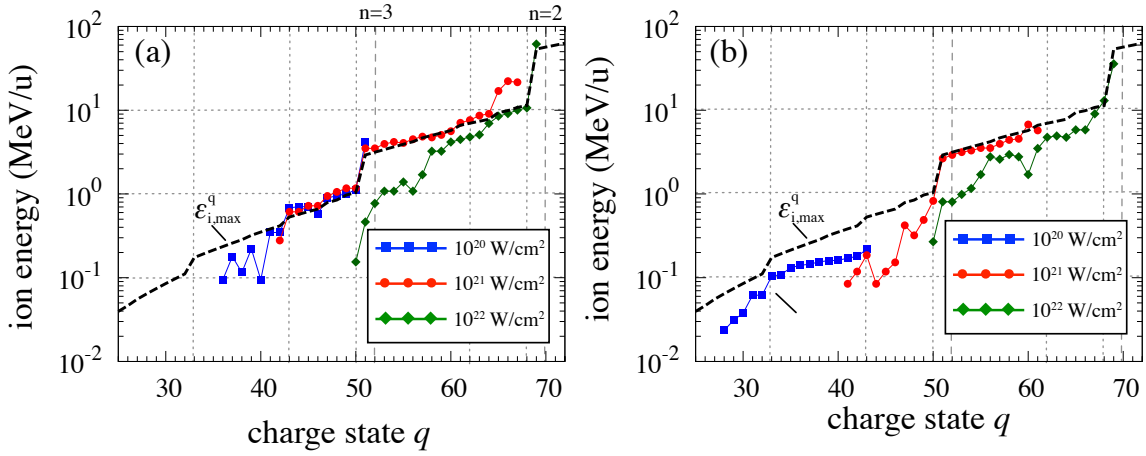

Fig5.9: Ion peak energies in the laser intensity $I = 10^{20}, 10^{21}, 10^{22}\mathrm{W/cm^2}$ and the scaling formula (5) for each charge state. Here, the charge dependence of the ion energy is compared in the case (a) w/o the contamination and (b) with 10nm contamination thickness

averaged energy increases to $< E_i > \simeq 7.2 \times 10^{-1}$ MeV/u. These energies are smaller than the maximum ion energy by roughly two orders. In the time scale that the ions are hardly expanded from the rear surface, the electric sheath field E_y ionizes the higher charge state before the electron impact ionization takes place. When the electron impact ionizes to the higher charge state, which is roughly estimated to $1.0/n_e\sigma_{im,(n=3)}v_e \simeq 800$ps, the accelerated ions are already expanded.

At the latter time, the three-body recombination process might take place in the high-

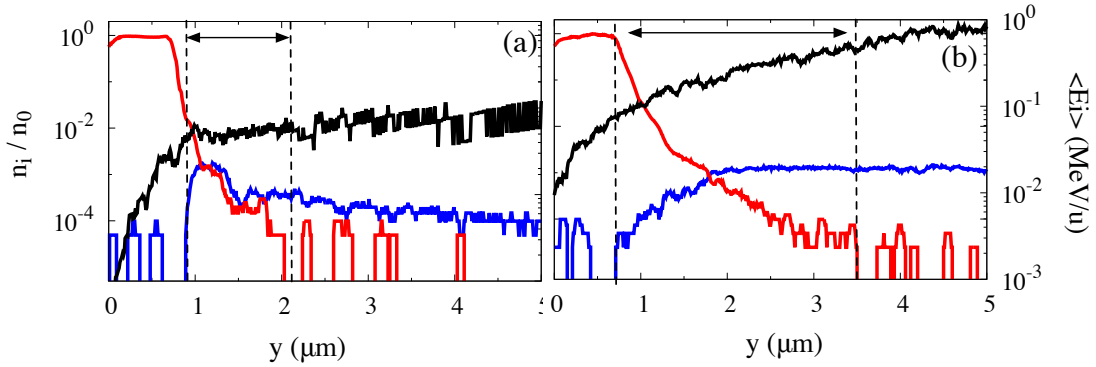

Fig5.10: Spatial distributions of the ion density ionized by the field (blue line) and that by the electron impact (red line), and the averaged ion energy (black line).

density plasma. For estimating the recombination effect for the ion acceleration, the ratio between the three body recombination and the electron impact ionization is calculated from the detailed balance equation, i.e.,

$$\frac{\sigma_R}{\sigma_I} = n_e \frac{g_i}{g_j} \frac{h^3}{(2\pi m_e T_e)^{3/2}} \exp[\frac{I_k}{T_e}] \tag{5.7-6}$$

Where, the σ_R and σ_I are the three-body recombination rate and the ionization rate for the charge state q, respectively, and h and m_e are the plank constant and the electron mass. It is calculated in each spatial mesh from the simulation result of the electron density $n_e(y)$ and the averaged electron temperature $< T_e(y) >$. Figure. 14 shows the spatial distributions of the average ratio of each electron shell as $\sigma_R/\sigma_I^n(y)$ and the averaged electron temperature $< T_e(y) >$ at $t = 500$ fsec in the cases of $I_l = 1.0 \times 10^{20}$ W/cm^2 (a) and $I_l = 1.0 \times 10^{21}$ W/cm^2 (b). In this time, the all ions already transit more than $n = 4$ in both cases, so that such estimation is only applied for $n = 3$ and $n = 4$. In the case (a), the averaged electron energy is around $< T_e >= 4.0$ keV, and the recombinations of both electron shells affect to only $\sigma_R/\sigma_I^{3,4}(y) \simeq 0.1$ even in the film region (0 μm $\leq$ y $<$ 0.8 μm). It drastically decrease with the ion expansion (0.8 μm $\leq$ y) to $\sigma_R/\sigma_I^{3,4} \simeq 10^{-9}$. In the case of (b), the electron averaged energy in the film region increases to $< T_e >= 30.0$ keV. Thus, both ratios of $n = 3, 4$ decrease to $\sigma_R/\sigma_I^{3,4} \simeq 4.0 \times 10^{-3}$ which shows the electron impact ionization becomes dominant with increasing of the irradiated laser intensity. In the outside region ($y \geq 0.8$), the averaged electron temperature exponentially increase to $< T_e >= 400.0$ keV which is mostly same to that in the case of (a). The both ratios is only $\sigma_R/\sigma_I^{3,4} \simeq 10^{-8}$. In considering that each ions ionized by the electron impact propagate to $y = 2.0$ μm and $y = 3.5$ μm as shown in Fig. 13, the recombination effect is small enough to be negligible for the accelerated mechanism.

5. 8 Conclusion

Heavy ion ionization and acceleration through the interaction between a gold thin film and a high-intensity short pulse laser were investigated by using a particle-in-cell code including atomic and collisional processes. We found that both mechanisms of radiation pressure acceleration (RPA) and target normal sheath acceleration (TNSA) shows different field ionization nature from the front and rear surface of the film. The ion energy accelerated through each mechanism are characterized by not only charge-to-mass ratio but also the

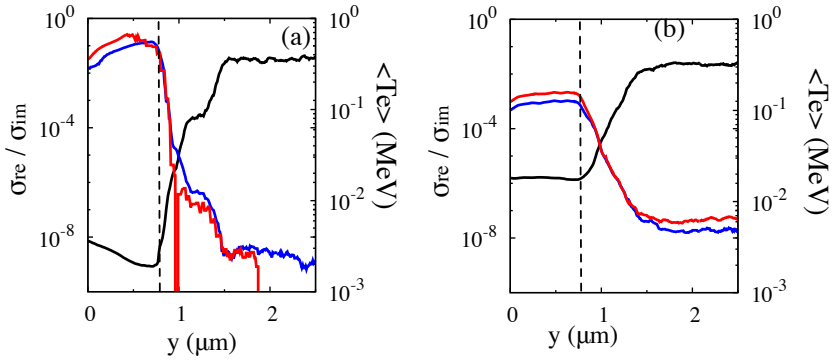

Fig5.11: Spatial distributions of $\sigma_R/\sigma_I^n(y)$ which is averaged every the electron shell as red line (n=3) and blue line (n=4) and the averaged electron temperature $< T_e(y) >$ as black line around the rear surface in each cases of (a) $I_l = 1.0 \times 10^{20}$ W/cm^2 and (b) $I_l = 1.0 \times 10^{21}$W/cm^2.

spatial distributions of the multiple charge states. Each mechanism was discussed for both the ion charge distribution and the ion energy in Sec. II and III and summarized as follows.

In the radiation pressure acceleration for the laser intensity $I = 10^{21}$ W/cm^2, the laser field directly ionizes the accelerated ions to the charge state $q = 69$, and then the electrostatic field balancing the laser ponderomotive force accelerates the charged ions to the inside of the film. The accelerated ions ballistically propagate keeping its charge state to the rear surface of the film. Then, the charged ions bunching from $q = 32$ (4d) to $q = 69$ (3s) are emitted with the energy range of 0.01 MeV/u $-$ 1.0MeV/u. The front of the ion bunch is re-accelerated by the sheath field on the rear surface, and its maximum energy reaches 10.8 MeV/u.

In the target normal sheath acceleration for the laser intensity $I = 10^{21}$ W/cm^2, the sheath field generated on the rear surface ionizes and then accelerates them. The front of the expanded ions with a maximum charge state $q = 67$ is predominantly accelerated to 22.2 MeV/u which is much larger than the energy of the lower charge state even without the dependence of the charge to mass ratio. For the lower charge state, the ions with the charge state q are also accelerated during the acceleration length $q\lambda_D$ which is approximated from the condition that the acceleration time is less than the laser pulse duration. The original scaling model formed by ionization potential value correctly describes the peak ion energy for each charge state in the range that the field ionization dominantly takes place.

The simulation result of the accelerated ion energy in RPA is slightly larger than the theoretical energy scaling, which has verified in the proton acceleration, due to the re-

acceleration of the electric sheath field near the rear surface, However, the simulation result of that in TNSA becomes less than the theoretical value due to the time transition of the charge to mass ratio after the acceleration starts. From the dependence of the irradiated laser intensity on the maximum ion energy, it is found that the energy scaling of TNSA, i.e., $I^{0.533}$ is larger than that of RPA, i.e., $I^{0.473}$ in considering the pure gold film. This relation is reversed by contamination thickness on the rear surface since the contaminated proton and oxygen attached on the rear surface are readily accelerated in front of the ion distribution of Au.

Here, we have only investigated the ion acceleration of Au in the region of the laser intensity $I = 10^{20-22}$ W/cm^2. In this region, it was founded that the electron impact ionization affects only the bulk ions since the high energy ions are ionized by the field ionization which corresponds to the accelerating electric field in each mechanism. Thus, the recombination process could be negligible for the accelerated ions. However, in lower laser intensity such as $I = 10^{18-19}$ W/cm^2 and also case with a thick layer of contaminated ions, the collisional relaxation process might have an important role for such acceleration mechanisms.

6 Conclusions and future work

In the previous fifth sections, we have presented the research work on the laser plasma interactions coupled with the ionization process. The various properties such as ion acceleration and the radiation is also investigated from the analysis of the ionization dynamics. In this section, we point out the meaning of our research and give a conclusion about the results.

- We developed an extended particle in cell code (EPIC3D) which includes both calculation schemes of the field tunnel ionization and the electron impact ionization and also the calculation schemes radiation processes. The tunnel field ionization process is calculated by electric field intensity applying to each ion particle based on the cross-section of ADK model[20]. The electron impact ionization is calculated by electron energy collided with an ion based on the cross-section of BEB model[18]. In addition to such ion-electron collision, the collisional processes between all species as electron-electron and ion-ion are also included for describing the collisional relaxation process. The Montecarlo calculation from each scheme judge whether an ionization happens or not at every time step so that the ionization corresponding the laser interaction can be described.

- Ionization dynamics resulting from the interaction between a high power femtosecond short pulse laser in the range of 10^{19-20} W/cm^2 and a carbon thin film in one-dimensional configuration was investigated using the particle-in cell code including atomic process and collisional relaxation process (EPIC). In this work, we found that the ionization of the film exhibits a multi-phase nature with different spatio-temporal structures due to the different ionization mechanism as summarized in the following. Specifically, the different charge state with different principal quantum number n, e.g. those for lower than or equal to C^{4+} and for higher than it, i.e. C^{5+} and C^{6+}, in the case of carbon film, shows different ionization dynamics qualitatively.

- The ionization front for C^{4+} exhibits a convective propagation keeping sharp ionization front. The localized longitudinal electrostatic field is found to be produced near the front and propagate with it, suggesting that the ionization is ascribed to the field. The velocity of the front is approximately $0.5 - 0.7c$ in the case with- and without the field ionization loss, respectively. It is noted that that the front velocity

is accelerated about 20% in later time that the laser field becomes larger. Then, the ionization front for C^{4+} reaches to the rear side, so that the whole film becomes a plasma with C^{4+}. This process is repeated by the electron bunches which are produced subsequently produced, so that the localized longitudinal electrostatic field and then the resultant ionization are sustained keeping the nearly constant propagation of the ionization front. The velocity of fast propagation of the ionization front for C^{4+} is insensitive to the density of the film though it weakly depends on the model for the field ionization loss.

- Heavy ion ionization and acceleration through the interaction between a gold thin film and a high-intensity short pulse laser were investigated by using a particle-in-cell code including atomic and collisional processes. We found that both mechanisms of radiation pressure acceleration (RPA) and target normal sheath acceleration (TNSA) shows different field ionization nature from the front and rear surface of the film. The ion energy accelerated through each mechanism are characterized by not only charge-to-mass ratio but also the spatial distributions of the higher charge states. Each mechanism was discussed for both the ion charge distribution and the ion energy.

- The simulation result of the accelerated ion energy in RPA is slightly larger than the theoretical energy scaling, which has verified in the proton acceleration, due to the re-acceleration of the electric sheath field near the rear surface, However, the simulation result of that in TNSA becomes less than the theoretical value due to the time transition of the charge to mass ratio after the acceleration starts. From the dependence of the irradiated laser intensity on the maximum ion energy, it is found that the energy scaling of TNSA, i.e., $I^{0.533}$ is larger than that of RPA, i.e., $I^{0.473}$ in considering the pure gold film. This relation is reversed by contamination thickness on the rear surface since the contaminated proton and oxygen attached on the rear surface are readily accelerated in front of the ion distribution of Au.

Scientific contributions

Published peer-revied papers

1. ○ D. Kawahito,Y. Kishimoto “Multi-phase ionization dynamics of carbon thin lm irradiated by high power short pulse laser”, Phys. Plasmas 108, 195001 (2017)

2. ○ D. Kawahito,Y. Kishimoto “Ionization and Acceleration of Heavy Ions in High-Z Solid Target Irradiated by High Intensity Laser”, has been accepted to Proc. Inertial Fusion Science Applications 2015

3. ○ D. Kawahito and Y. Kishimoto, “Acceleration of multiply ionized ions in high-Z solid film irradiated by high intensity laser” in preparation for submission

Presentations at academic conference and symposiums

1. (oral) D. Kawahito ,Y. Kishimoto “Magnetic dynamics and confinement of high energy density plasma produced by laser interaction with rod array target”, The technical meeting on High Energy Density Science with High Power Laser, Livermore, USA, Sep, 2017

2. (oral) ○ D. Kawahito ,Y. Kishimoto “Characteristics of radiation in non-equilibrium plasma produced by high intensity laser”, 6th East-Asia School and Workshop on Laboratory, Space, and Astrophysical plasmas (EASW 2016), Tukuba, Japan, July, 2016

3. (oral) ○ D. Kawahito ,Y. Kishimoto, and Yuji Fukuda “Generation and acceleration of high charge state ions through the interaction between high-intense laser and high-Z matter”, Plasma conference 2014, Toki Messe, Niigata, Japan, November, 2014

4. (poster) ○ D. Kawahito and Y. Kishimoto, “Magnetic dynamics and confinement properties in non-equilibrium extreme radiation plasma”, 10th International Conference on Inertial Fusion Sciences and Applications (IFSA 2015) , September, 2017

5. (poster) ○ D. Kawahito and Y. Kishimoto, “Ionization and Acceleration of Heavy Ions in High-Z Solid Target Irradiated by High Intensity Laser”, 9th International

Conference on Inertial Fusion Sciences and Applications (IFSA 2015) , September, 2015

6. （poster）○D. Kawahito and Y. Kishimoto,“Characteristics of radiation from the interaction between haevy element plasma and high intensity laser”Specialized International Conference in OPTICS PHOTONICS International Congress (OPIC2016), Yokohama, Japan, July, 2016

7. （poster）○D. Kawahito and Y. Kishimoto,“Characteristics of magnetic structure formation in high power laser driven high-Z plasma”21st NEXT Workshop, March, 2016

8. （poster）○D. Kawahito and Y. Kishimoto,“Generating and acceleration of multiply-charged ions in double layered thin film irradiated by high intensity lasers”,International workshop on Matter in Extreme Conditions Montgenèvre French, February 2015

9. （oral）○川人大希、岸本泰明,“高強度レーザーと構造性媒質の相互作用における磁場のダイナミックスと自己組織化”, 日本物理学会 第 72 回年次大会,22pAP-6, 大阪大学, 2017 年 3 月

10. （oral）○川人大希、岸本泰明,“高強度レーザーと構造性媒質の相互作用における磁場の生成過程と自己組織化”, 強磁場下の超高強度レーザー駆動無衝突撃破とイオン加速に関する研究会, 2017 年 3 月

11. （oral）○川人大希、岸本泰明、福田祐仁,“高強度レーザーと重元素物質との相互作用による高価数イオンの生成・抽出”, 日本物理学会 2016 年秋季大会,16aKC-6, 金沢大学, 2016 年 9 月

12. （oral）○川人大希、岸本泰明,“X 線輻射を考慮した PIC コードの開発とシミュレーション”, 大阪大学レーザーエネルギー学研究センター共同利用・共同研究 A2　第三回課題研究会, 京都大学, 2016 年 3 月

13. （oral）○川人大希、岸本泰明、森林健吾、福田祐仁,“電離過程に支配される超高強度レーザー生成重元素プラズマの特性”, 日本物理学会 2016 年秋季大会,22pAP-6, 関西大学, 2015 年 9 月

14. （oral）○川人大希、岸本泰明、森林健吾、福田祐仁,“高強度レーザーと高 Z 物質の相互作用による高価数イオンの生成と加速 ()”, 日本物理学会 第 70 回年次大会,22pAP-6, 早稲田大学, 2015 年 3 月

15. （oral）○川人大希、岸本泰明、森林健吾、福田祐仁,“高強度レーザーと高価数固体薄膜との相互作用による多価イオン生成過程と粒子加速”, レーザープラズマ科学のため最先端シミュレーションコード共同開発・利用に関する研究会, 2015 年 1 月

16. （oral）○川人大希、Feng Wu、岸本泰明,“高強度レーザーによる固体媒質の多段階電離ダイナミクスとトリガーの物理機構”, 日本物理学会 第 69 回年次大会, 30aAX-5, 東海大学,2014 年 3 月

17. （oral）○川人大希、Feng Wu、岸本泰明,“レーザー照射媒質で電離波伝播のダイナミックスと構造”, レーザープラズマ科学のための最先端シミュレーションコードの共同開発・共用に関する研究会, 2014 年 1 月

18. （oral）○川人大希、山本寛子, 鷲田浩人, 李暁龍, 和田弓規, 小川琢己,　山口聡一郎, 浅川誠,“フェムト秒電子バンチのパルス幅伸長”, 電気学会光応用・視覚研究会, LAV-12, 大阪産業大学, 2012 年 12 月

19. （poster）○川人大希、岸本泰明,“高強度レーザー生成プラズマ中の X 線・γ 線放射に関する数値シミュレーション研究”, 第 332 回生存圏シンポジウム「宇宙プラズマ波動研究会」, 2016 年 12 月

20. （poster）○川人大希、岸本泰明,“Emission of bremsstrahlung from heavy element plasma produced by high intensity laser”, 第 16 回光量子科学研究シンポジウム, 2015 年 10 月

21. （poster）○川人大希、岸本泰明,“Generation and acceleration of high charge state ions through the interaction between high-intense laser and high-Z matter”, 第 15 回光量子科学研究シンポジウム, 2014 年 10 月

22. （poster）○川人大希, 鷲田浩人, 山本寛子,　山口聡一郎, 浅川誠,“フェムト秒フォトインジェクターでの電子バンチ放射光測定系の開発”, 第 22 回日本赤外線学会研究発表会, p-17, 関西大学 2012 年 12 月

References

[1] A. L. Schawlow and C.H. Towns, Phys.Rev. **112** 1940 (1958)

[2] T. H. Maiman, Nature 187, 493(1960)

[3] G. Mourou and D. Unstadter, Phys. Fluids B **4**, 2315(1992)

[4] L. M. Gorbunov., Usp. Fiz. Nauk **109**, 631-665(1973)

[5] G. Mourou, et al., Rev. Mod. Phys.Rev.Lett. **43**, 267(1979)

[6] S.P. Hatchett et al., Phys. Plasmas **7**, 2076 (2000)

[7] C. Yamanaka, S. Nakai, T. Yamanaka, Y. Izawa, Y. Kato, K. Mima, K. Nishihara, T. Mochizuki, M. Yamanaka, M. Nakatsuka, et al. High thermonuclear neutron yield by shock multiplexing implosion with gekko xii green laser. Nuclear fusion, 27(1):19–30, (1987)

[8] G. Thiell, A. Adolf, M. Andre, N. Fleurot, D.D. Juraszek, and D. Schirman. The phebus experimental facility operating at 250 ps and 0.53 m. Laser and Particle Beams, 6:93–103, (1988)

[9] E.M. Campbell. The national-ignition-facility project. Fusion Technol, 26:755– 766, 1994.

[10] E.I. Moses and C.R. Wuest. The national ignition facility: laser performance and first experiments. Fusion Science and Technology, 47(3), 2005.

[11] F. Brunel., Phys. Rev. Lett. 59(1987)

[12] W. L. Kruer and Kent Estabrook., Phys. Fluid **28**, 430(1985)

[13] S. Kato, B. Bhattacharyya, A. Nishiguchi, and K. Mima, Phys. Fluids B, vol. **5**, p. 564, 1993.

[14] G. Malka and J. L. Miquel, Phys. Rev. Lett, **77**, p. 704, 1977.

[15] 正木知宏:学位論文「高強度レーザーと物質との相互作用に関するシミュレーション研究」2008 年 (京都大学大学院エネルギー科学研究科)

[16] T. Tajima, Computaional Plasma Physics: With Application to Fusion and Astrophysics, Addison Wesley

[17] T. Takizuka and H. Abe., J. Comp. Phys. **25**, 205

[18] Y. K. Kim and M. E. Rudd, Phys. Rev. A **50**, 3954 (1994)

[19] L. Keldysh, Sov. Phys. JETP **20**,1307(1964)

[20] M. V. Ammosov, et al, Sov. Phys. JETP **64**, 1191 (1986)

[21] G Mur., IEEE10.1109/TEMC.(1981)

[22] Jean-Pierre Berenger., Journal of Computational Physics **114** 2 (1994)

[23] J. D. Kmetec, C. L. Gordon, III, J. J. Mackin, B. E. Lemoff, G. S. Brown,and S. E. Harris, Phys. Rev. Lett. **68**, 1527 (1992).

[24] M. Schnurer, M. P. Kalashnikov, P. V. Nickles, Th. Schlegel, and W. Sandner, Phys. Plasmas **2**, 3106 1995.

[25] Y. Sentoku, K. Mima, T. Taguchi, S. Miyamoto, and Y. Kishimoto, Physics of Plasmas **5**, 4366 (1998)

[26] T. Ditmire, J. Zweibeck, V.D. Yanovsky, T. E. Cowan, G. Hays, and K. B. Wharton, Nature (London) **398**, 489 (1999).

[27] Y. Kishimoto, T.Masaki, and T. Tajima, Phys. Plasmas **9**, 589 (2002).

[28] S. V. Bulanov, T. Zh. Esirkepov, M. Kando, J. K. Koga, S. S. Bulanov, Phys. Rev. E **84**, 056605 (2011)

[29] J. Koga, Phys. Rev. E **70**, 046502 (2004).

[30] L. D. Landau and E. M. Lifshits, The Classical Theory of Fields (Pergamon, New York, 1994).

[31] I. V. Sokolov et al., Phys. Plasmas **18**, 093109 (2011)

[32] T.Tajima and J. M. Dawson. Phys. Fluids B **4**, 2315 (1992)

[33] G. Mourou, et al., Rev, Mod. Phys. **78**, 309 (2006)

[34] Daido, H., M. Nishiuchi, and A. S. Pirozhkov, Rep. Prog. Phys. **75**, 056401 (2012).

[35] Zheng-Ming Sheng, Kunioki Mima, Jie Zhang, and Heiji Sanuki, Phys. Rev. Lett. **94**, 095003 (2005).

[36] Sentoku Y, Mima, T. Taguchi, S.MIyamoto and K, Kishimoto Phys. Plasmas textbf5, 4366 (1998)

[37] T Nakamura, and JK Koga, et al, Phys. Plasmas **108**, 195001 (2012)

[38] S Fujioka, et al, Plasma Physics and Controlled Fusion, **54**, 12 (2012)

[39] K. Nakashima and H Takabe, Phys. Plasmas **9**, 1505 (2002)

[40] T. E. Cowan, and A. W. Hunt, et al, Phys. Rev. Lett **84**, 903 (2000).

[41] T. Ditmire, et al, Nature (London) **398**, 489 (1999).

[42] M. Tabak, et al, Phys. Plasmas **1**, 1626 (1994).

[43] E.I. Moses and C.R. Wuest. The national ignition facility: laser performance and first experiments. Fusion Science and Technology, 47(3), 2005.

[44] T. Ditmire, et al, Phys. Rev. A **53**, 3379 (1996).

[45] T.Tajima, Computational Plasma Physics: With Application to Fusion and Astrophysics, Addison Wesley

[46] F. Brunel, Phys. Rev. Lett. **59** (1987).

[47] W. L. Kruer and Kent Estabrook, Phys. Fluid **28**,430 (1985).

[48] B.-T. V. Vu, A. Szoke, and O. L. Landen, Phys. Rev. Lett. **72**, 3823 (1994).

[49] Y.Kishimoto, K.Mima and M. G.Haines, J. Phys. Soc. Jpn. **57** 1972 (1988).

[50] T. Tajima, J. M. Dawson, Phys. Rev. Lett., **43** 267 (1979).

[51] E. Felmi, Phys. Rev. **75** 1169 (1945).

[52] Bowers et al, Optics Letter **31**, No1(2006).

[53] S. Kato, Y. Kishimoto, et al, Phys. plasmas **5**, 292 (1998).

[54] V. T. Tickhonchuk, Phys. plasmas **9**, 4 (2002).

[55] A. Debyle and V. T. Tickhonchuk, Phys. plasmas **14**, 073104 (2007).

[56] S. Kato, Y. Kishimoto, et al, Plasma Fusion Res **7** 267 (2012).

[57] T. Masaki T. Kishimoto, Plasma Fusion Res **81** 643 (2005).

[58] S. C. Rae and K. Burnett, Phys. Rev. A **46**, 1084 (1992).

[59] T. Takizuka and H. Abe., J. Comp. Phys. **25**, 205 (1977).

[60] Y. Sentoku and A.J. Kemp, J. Comput. Phys. **227**, 6846 (2008).

[61] S. Nakazaki et al., J. Phys. Soc. Jpn. 60, 1565 (1991).

[62] J. Robertson, J. Pure and Applied Chemistry. **66**, 9 (1994).

[63] H. C. Ong and R. P. H. Chang, Phys. Rev. B. **55**, 13213 (1997). (2006).

[64] D. Kawahito and Y. Kishimoto, Physics of Plasmas **24**, 103105

[65] V. T. Tickhonchuk, Phys. plasmas **9**, 4 (2002).

[66] A. Debyle and V. T. Tickhonchuk, Phys. plasmas **14**, 073104 (2007).

[67] S. Kato, Y. Kishimoto, et al, Plasma Fusion Res **7** 267 (2012).

[68] S. C. Wilks, A. B. Langdon, T. E. Cowan, M. Roth, M. Singh, S. Hatchett, M. H. Key, D. Pennington, A. MacKinnon, and R. A. Snavely, Physics of Plasmas **8**, 542–549 (2001),

[69] H. Schwoerer, S. Pfotenhauer, O. J ackel, K.-U. Amthor, B. Lies- feld, W. Ziegler, R. Sauerbrey, K. W. D. Ledingham, and T. Esirkepov, Nature **439**, 445–448 (2006).

[70] M. Nishiuchi, A. Fukumi, H. Daido, Z. Li, A. Sagisaka, K. Ogura, S. Orimo, M. Kado, Y. Hayashi, M. Mori, S. Bulanov, T. Esirke- pov, K. Nemoto, Y. Oishi, T. Nayuki, T. Fujii, A. Noda, Y. Iwashita, T. Shirai, and S. Nakamura, Physics Letters A **357**, 339–344 (2006).

[71] L. Robson, P. T. Simpson, R. J. Clarke, K. W. D. Ledingham, F. Lindau, O. Lundh, T. McCanny, P. Mora, D. Neely, C.G. Wahlstr om, M. Zepf, and P. McKenna, Nature Physics **3**, 58–62 (2007).

[72] H. Daido, M. Nishiuchi, and A. S. Pirozhkov, Reports on Progress in Physics **75**, 056401 (2012).

[73] S. V. Bulanov and V. S. Khoroshkov, Plasma Physics Reports **28**, 453–456 (2002).

[74] S. Fritzler, V. Malka, G. Grillon, J. P. Rousseau, F. Burgy, E.Lefebvre,E.D ' Humi'eres,P.McKenna,andK.W.D.Led- ingham, Applied Physics Letters **83**, 3039–3041 (2003).

[75] M. Roth, T. E. Cowan, M. H. Key, S. P. Hatchett, C. Brown, W. Fountain, J. Johnson, D. M. Pennington, R. A. Snavely, S. C. Wilks, K. Yasuike, H. Ruhl, F. Pegoraro, S. V. Bulanov, E. M. Campbell, M. D. Perry, and H. Powell, Physical Review Letters **86**, 436–439 (2001).

[76] M. T. S. Atzeni and J. Honrubia, Nucl. Fusion **42** (2002).

[77] E. L. Clark, K. Krushelnick, M. Zepf, F. N. Beg, M. Tatarakis, A. Machacek, M. I. K. Santala, I. Watts, P. A. Norreys, and A. E. Dangor, Physical Review Letters **85**, 1654–1657 (2000).

[78] M. Nishiuchi, H. Sakaki, et al., Review of Scientific Instruments **85**, 02B904 (2014).

[79] M. Nishiuchi, H. Sakaki, et al., Physics of Plasmas **22**, 033107 (2015).

[80] W. Scheid, H. Mu ller, and W. Greiner, Physical Review Letters **32**, 741–745 (1974).

[81] K. W. D. Ledingham, J. Magill, et al., Journal of Physics D: Applied Physics **36**, L79–L82 (2003).

[82] V. Malka, S. Fritzler, et al., " Electron acceler- ation by a wake field forced by an intense ultrashort laser pulse. " Science (New York, N.Y.) **298**, 1596–600 (2002).

[83] F. Ewald, H. Schwoerer, S. Du sterer, R. Sauerbrey, J. Magill, J. Galy, R. Schenkel, S. Karsch, D. Habs, and K. Witte, " Application of relativistic laser plasmas for the study of nuclear reactions, " Plasma Physics and Controlled Fusion **45**, A83–A91 (2003).

[84] K. Nemoto, A. Maksimchuk, S. Banerjee, K. Flippo, G. Mourou, D. Umstadter, and V. Y. Bychenkov, Applied Physics Letters **78**, 595–597 (2001).

[85] K. W. D. Ledingham, P. McKenna, et al., Journal of Physics D: Applied Physics **37**, 2341– 2345 (2004).

[86] A. J. Mackinnon, Y. Sentoku, P. K. Patel, D. W. Price, S. Hatchett, M. H. Key, C. Andersen, R. Snavely, and R. R. Freeman, Physical Review Letters **88**, 215006 (2002).

[87] M. Kaluza, J. Schreiber, M. I. K. Santala, G. D. Tsakiris, K. Ei- dmann, J. Meyer-ter Vehn, and K. J. Witte, Physical Review Letters **93**, 045003 (2004).

[88] E. D ' Humi‘eres, E. Lefebvre, L. Gremillet, and V. Malka, Physics of Plasmas **12**, 062704 (2005).

[89] L. O. Silva, M. Marti, J. R. Davies, R. A. Fonseca, C. Ren, F. S. Tsung, and W. B. Mori, "Proton Shock Acceleration in Laser-Plasma Interactions," Physical Review Letters **92**, 015002 (2004).

[90] P. Mora, Physical Review Letters **90**, 185002 (2003).

[91] P. Mora, Physical Review E **72**, 056401 (2005).

[92] M. Passoni, V. T. Tikhonchuk, M. Lontano, and V. Y. Bychenkov, Physical Review E **69**, 026411 (2004).

[93] M. Passoni and M. Lontano, Physical Review Letters **101**, 115001(2008).

[94] Y. Sentoku, T. E. Cowan, A. Kemp, and H. Ruhl, Physics of Plasmas **10**, 2009–2015 (2003).

[95] A. Henig, S. Steinke, M. Schnu rer, T. Sokollik, R. H orlein, D. Kiefer, D. Jung, J. Schreiber, B. M. Hegelich, X. Q. Yan, J. Meyer-ter Vehn, T. Tajima, P. V. Nickles, W. Sandner, and D. Habs, Physical Review Letters **103**, 245003 (2009).

[96] T. Esirkepov, M. Borghesi, S. V. Bulanov, G. Mourou, and T. Tajima, Physical Review Letters **92**, 175003 (2004).

[97] D. Kawahito and Y. Kishimoto, Physics of Plasmas **24**, 103105 (2017).